Probing the multiphase interstellar medium in an extreme starburst at high redshift

Author:
Matthew DOHERTY

Supervised by:
Prof. J.E GEACH
Prof. K.E.K. COPPIN
Dr. J. STEVENS

Centre for Astrophysics Research
School of Physics, Astronomy and Mathematics
University of Hertfordshire

Submitted to the University of Hertfordshire in partial fulfilment of the requirements of the degree of Doctor of Philosophy.

July 2023

Abstract

In this thesis we present a range of observations and results relating to the lensed hyperluminous sub-mm galaxy '9io9' at $z = 2.6$, where we have used sub-mm/mm spectroscopy targeting the dense and cold interstellar medium to better undertstand the conditions underlying extreme star formation (1000$\times$ that of the Milky Way) in galaxies the early Universe.

In Chapter 2 we present new observations with the Atacama Large Millimeter/sub-millimeter Array (ALMA) of the 122- and 205-μm fine-structure line emission of singly-ionised nitrogen in 9io9. The 122-/205-μm [N II] line ratio is sensitive to electron density, $n_{\rm e}$, in the ionised interstellar medium, and we use this to measure $n_{\rm e} \approx 300\,{\rm cm}^{-3}$ averaged across the galaxy. This is over an order of magnitude higher than the Milky Way average, but comparable to localised Galactic star-forming regions. Combined with observations of the atomic carbon (C I(1–0)) and carbon monoxide (CO $J = 4$–3) in the same system, we reveal the conditions in this intensely star-forming system. The majority of the molecular interstellar medium has been driven to high density, and the resultant conflagration of star formation produces a correspondingly dense ionised phase, presumably co-located with myriad H II regions that litter the gas-rich disk.

In Chapter 3 we present the detection of the ground state rotational emission of ammonia, ortho-NH_3 ($J_K = 1_0 \rightarrow 0_0$) in 9io9. The integrated line profile is consistent with other molecular and atomic emission lines which have resolved kinematics well-modelled by a 5 kpc-diameter rotating disc. This implies that the gas responsible for NH_3 emission is broadly tracing the global molecular reservoir, but likely distributed in pockets of high density ($n \gtrsim 5 \times 10^4\,{\rm cm}^{-3}$). With a luminosity of $2.8 \times 10^6\,L_\odot$, the NH_3 emission represents 2.5×10^{-7} of the total infrared luminosity of the galaxy, comparable to the ratio observed in the Kleinmann-Low nebula in Orion and consistent with sites of massive star formation in the Milky Way. If $L_{\rm NH_3}/L_{\rm IR}$ serves as a proxy for the 'mode' of star formation, this hints that the nature of star formation in extreme starbursts in the early Universe is similar to that of Galactic star-forming regions, with a large fraction of the cold interstellar medium in this state, plausibly driven by a storm of violent disc instabilities in the gas-dominated disc. This supports the 'full of Orions' picture of star formation in the most extreme galaxies seen close to the peak epoch of stellar mass assembly.

In Chapter 4 we present new ALMA observations of 9io9 detecting CO J=5$\rightarrow$4 and its isotopologues ^{13}CO J=5$\rightarrow$4 and C^{18}O J=5$\rightarrow$4. Since ^{13}C is mainly produced by intermediate-mass stars and ^{18}O is produced by massive stars, ^{13}CO/C^{18}O is sensitive to the shape of the stellar initial mass function (IMF), where the IMF of the Milky Way has a power law slope $\alpha_2 \approx 2.3$–2.6 for stars of masses above $0.5\,{\rm M}_\odot$. We measure a galaxy-integrated luminosity ratio ^{13}CO/C^{18}O $= 1.6 \pm 0.1$, consistent with the ratio observed in local ultraluminous infrared galaxies and submillimetre-selected galaxies at high redshift, and significantly lower than the ^{13}CO/C^{18}O of the Milky Way. It has been argued that the low ^{13}CO/C^{18}O observed in extreme star-forming galaxies in the early Universe is evidence for a top-heavy IMF in these systems. In this work we use state-of-the-art chemical evolution models to conclude that irrespective of

stellar rotation, the observed ^{13}CO/C^{18}O is consistent with a Kroupa IMF with high-mass slope of $\alpha_2 = 2.3$ (as in our Milky Way models) and also the steeper 'top-heavy' $\alpha_2 = 2.1$ slope.

In Chapter 5 we present a discussion of ongoing work on an ALMA spectral scan of 9io9, alongside some potential future avenues of research, in particular pushing to higher resolution with ALMA, and MIRI observations with JWST probing the mid infrared PAH emission as a AGN diagnostic.

Declaration

I declare that no part of this work is being submitted concurrently for another award of the University or any other awarding body or institution. This thesis contains a substantial body of work that has not previously been submitted successfully for an award of the University or any other awarding body or institution.

The following parts of this submission have been published previously and/or undertaken as part of a previous degree or research programme:

1. Chapter 2: this has been published as Doherty et al., 2020, *The Astrophysical Journal*, **905**, 2.
2. Chapter 3: this has been published as Doherty et al., 2022, *Monthly Notices of the Royal Astronomical Society: Letters*, **517**, 1.

The following parts of this submission have not been undertaken as part of a previous degree or research programme and have not yet been published.

1. Chapter 4: To be submitted to MNRAS.

Except where indicated otherwise in the submission, the submission is my own work and has not previously been submitted successfully for any award.

Acknowledgements

Over the past four and a half years I have been lucky to be surrounded by a great group of people at and away from Hertfordshire and it's only fitting that I thank them here.

Firstly, I am grateful to my supervisor Jim Geach, for offering me the position in the first place. After not receiving any offers in my first round of applications, you can't imagine how great it felt to receive the offer to work with you these past few years. I appreciate the help and guidance you've given me and your patience with my often slow and likely painful to read writing. Whilst COVID scuppered some of the plans, I also appreciate the opportunity you gave me to be able to travel to various places and conferences to present my work.

I also want to thank all of my collaborators for their helpful feedback on all of my paper drafts, whilst sometimes there was slow progress, your inputs vastly improved the quality of the work and for that I am grateful. I would in particular like to thank Rob Ivison and Chiaki Kobayashi, who agreed to write me references as I look towards the next stage of my career.

I have been fortunate to meet and make good friends in the department and met a lot of great PhD students too numerous to mention, with who discussing all the interesting things they were working on have been a great and needed distraction from my own projects. Sharing the past few years with everyone has been one of the highlights of my life thus far and I will miss everyone.

I would like to thank my Sub-mm brethren Tracy, who started her PhD journey alongside me and was a great help to me in understanding the subject of which I was unfamiliar with before I came, and helped keep things running when the rest of our year were too lazy to help.

I cannot leave out Kasia who after I had moved away in the last few months of writing this thesis allowed me to stay on her sofa when I've returned to hatfield, it has really been appreciated by me and my bank balance!

I would like to in particular thank the 2E50 peeps, sharing an office is only as good as the people within and I have been lucky to share with a great group of people. To Alex, Max, and Tom (Spriggs): Thank you for making me feel so welcome when I arrived and for helping me with all my naïve linux and python questions, without which I would probably still be staring at the terminal blankly.

To Marina and Niall: You came into the office two years after me, but fit straight in our random meandering discussions on lots of topics (including the ones Calum banned) as well as all the science discussions (as everyone elses research was always more interesting than what I need to do!) you both always made me enjoy coming in to the office. To Calum, the most consistent member of the 2E50 peeps, we started on the same day and are finishing together as well. Whilst we did our masters together (sorry for not remembering you), you have been a great friend and

office mate over the years. I will always remember you storming in the office whilst I was giving an online talk during covid, and I'm sure that made an impression on everyone listening online too!

To the 13 Horsa Gardens (astro house) crew, I lived there throughout my PhD and lived with many different people from the department. To Athulya, Ben, Brian, Jaime, Maddie B, Maddie S, Mike, Mubela, and Ryan. Whilst I wasn't always the best housemate, I've had great times in that house with you all over the years, thanks for all the help and support you have given me I really appreciate it and I will miss living there as you have all made it feel like home.

I would also like to thank all of my friends from undergraduate and otherwise, who have put up with me the last few years. Whilst we don't see each other as much as I would like, your friendship has helped me through hard times and I don't think I would be writing this right now without all of your support.

Finally I would like to thank my family. My mum Jewlee and step-dad Martyn, for nagging me to keep working, being there for me, and helping me out whenever I needed it (including letting me move back towards the end of writing my thesis. My dad, Micheal, who sadly isn't here to see me finish. You always took pride in what I was doing and I would enjoy our conversations on it, even though you would try your best constantly embarrass me. To my brothers Chris, Gareth, Jack, and Liam, for all the laughs we have when we all get together (and your taxes which funded much of my education), the support (and free takeaways won't be forgotten).

Contents

List of Figures

List of Tables

List of Abbreviations

Acronym	**W**hat (it) **S**tands **F**or
AGB	**A**symptotic **G**iant **B**ranch
ALMA	**A**tacama **L**arge **M**illimetre/sub-millimetre **A**rray
BBN	**B**ig **B**ang **N**ucleosynthesis
CDM	**C**old **D**ark **M**atter
CMB	**C**osmic **M**icrowave **B**ackground
DSFG	**D**usty **S**tar **F**orming **G**alaxy
FLRW	**F**riedmann **L**emaître **R**obertson **W**alker
FWHM	**F**ull **W**idth **H**alf **M**aximum
GCE	**G**alactic **C**hemical **E**volution
GMC	**G**iant **M**olecular **C**loud
HIFI	**H**eterodyne **I**nstrument (for the) **F**ar-**I**nfrared
HyLIRG	**Hy**per **L**uminous **I**nfra**R**ed **G**alaxy
IMF	**I**nitial **M**ass **F**unction
ISM	**I**nter**S**tellar **M**edium
JCMT	**J**ames **C**lerk **M**axwell **T**elescope
JWST	**J**ames **W**ebb **S**pace **T**elescope
LAS	**L**argest **A**ngular **S**cale
LIRG	**L**uminous **I**nfra**R**ed **G**alaxy
LRG	**L**uminous **R**ed **G**alaxy
LTE	**L**ocal **T**hermal **E**quilibrium
NIR	**N**ear **I**nfra**R**ed
NFW	**N**avarro–**F**renk–**W**hite **PAH**
Polycyclic **A**romatic **H**ydrocarbon	
RRR	**R**ed **R**adio **R**ing

SED	**S**pectral **E**nergy **D**istribution
SFH	**S**tar **F**ormation **H**istory
SFR	**S**tar **F**ormation **R**ate
SMG	**S**ub-**M**illimetre **G**alaxy
SNR	**S**ignal (to) **N**oise **R**atio
ULIRG	**U**ltra **L**uminous **I**nfra**R**ed **G**alaxy
UV	**U**ltra**V**iolet
VDI	**V**iolent **D**isk **I**nstability
WIM	**W**arm **I**onised **M**edium
YSO	**Y**oung **S**tellar **O**bject

Chapter 1

Introduction

1.1 Introduction to the standard model of cosmology

The study of the Universe is one of our species' oldest, with many cultures having their own creation stories and myths. With the advent of the General theory of Relativity (Einstein, 1916) and a host of observations in the 1920s (Slipher, 1917; Hubble, 1929) vastly increasing the scale of our Universe, beyond just the Milky Way and revealing the expanding nature of our Universe, cosmology started to become a scientific discipline in of itself.

The initial discovery of galaxies external to our own (or the island universe hypothesis at the time), was made possible by the discovery of a so called 'standard candle'. Henrietta Swan Leavitt, in 1908 published results on a class of stars known as cepheid variables in the Magellanic clouds (Leavitt, 1908). What was found was a strong period-luminosity relation for this class of stars, as such if you can measure the period, you can determine the luminosity and from this a distance can be inferred. This seminal result made possible accurate distance determinations to what we now know to be different galaxies, so long as you can observe cepheids within. The second key piece to our cosmological picture comes from redshift. Starting in the 1910s with pioneering work by Slipher (Slipher, 1917), who by spectrally observing bright spiral 'nebulae' found them to have a far greater redshift than any star observed in the galaxy, implying that these objects are moving away from us at far greater speeds, and unlikely to be part of the Milky Way. Hubble in the 1920s (Hubble, 1929), combined both of these results and by looking at the outer regions of many of these sources to find cepheid variables, determined distances to

many of these sources and found that these 'nebulae' lay well outside that of the known Milky Way and their distance was proportional to their observed redshift.

1.1.1 Friedmann, Robertson, Lemaître, Walker and the standard model of cosmology

In the decade following the publication of GR, the race began and a multitude of solutions to the equations, both exact, such as the Schwarzschild solution (Schwarzschild, 1916) and approximate, with various solutions involving gravitational lensing (Einstein, 1936), another of these solutions is known as the Friedmann, Robertson, Lemaître, Walker (FLRW) metric (Friedmann, 1922). The FLRW metric is a cosmological solution to the Einstein equations, under the assumption of an isotropic and homogeneous Universe, providing a simple model for the history of the Universe with a few free parameters as shown in equation 1.1 in spherical coordinates.

$$(ds)^2 = (c\ dt)^2 - a^2(t)\left[\frac{dr^2}{1-kr^2} + r^2(d\theta^2 + sin^2(\theta)d\phi^2)\right] \tag{1.1}$$

where c is the speed of light in vacuum, a is the scale factor, and k is a term defining spatial curvature.

Over the decades a range of different cosmological models have been proposed to explain cosmological observations such as the redshifting of light from distant sources, the relative abundance of the light elements, etc, but models based on the FLRW metric have become the preferred models. The current 'standard' model of cosmology is known as ΛCDM where Λ refers to the dominant source of energy density, nominally referred to as Dark Energy (which in this form is also known as the cosmological constant), and CDM being cold dark matter, these denoting the dominant sources of the Universe's energy density.

By applying this metric to the Einstein equations, a set of two equations can be obtained describing the past, present, and future expansion and evolution of the Universe, known as the Friedmann equations. For the standard model of cosmology these take the form:

$$\left(\frac{\dot{a}}{a}\right)^2 = \frac{8\pi G\rho}{3} - \frac{kc^2}{a^2} + \frac{\Lambda c^2}{3} \tag{1.2}$$

$$\left(\frac{\ddot{a}}{a}\right) = -\frac{4\pi G\rho}{3}\left(\rho + \frac{p(t)}{c^2}\right) - \frac{kc^2}{a^2} + \frac{\Lambda c^2}{3} \tag{1.3}$$

With ρ being the matter density, p denoting the radiation pressure, Λ being the cosmological constant, and k the spatial curvature taking the values of +1, 0, -1 corresponding to a positively curved, flat, and negatively curved Universe.

A more convenient way of parameterising the equations 1.2 and 1.3 would be with respect to the Hubble constant (H_0) and the present density parameters $\Omega_{0,\mathrm{m}}$, $\Omega_{0,\mathrm{r}}$, $\Omega_{0,\mathrm{k}}$ and Ω_Λ, which correspond to the fraction of the Universe's present energy density 'locked' up in the matter, radiation, curvature, and dark energy.

Written in this form, the Friedmann equations are:

$$\frac{H^2}{H_0^2} = \Omega_{0,\mathrm{R}}a^{-4} + \Omega_{0,\mathrm{m}}a^{-3} + \Omega_{0,k}a^{-2} + \Omega_{0,\Lambda} \tag{1.4}$$

$$\left(\frac{\ddot{a}}{H_0^2 a}\right) = -\Omega_{0,R}a^{-4} - \frac{1}{2}\Omega_{0,m}a^{-3} + \Omega_{0,\Lambda} \tag{1.5}$$

In equation 1.5, it can be seen that $\Omega_{0,k}$ does not appear, this means that $\Omega_{0,k}$ does not affect the acceleration of the Universe (this is true for any source of energy density which falls off by a^{-2}). From these two equations, given the density parameters for the different components, and the current expansion rate of the Universe, the past and future evolution of the Universe can be described. Over the decades a range of predictions associated with the standard model have been verified, most notably that of the discovery of the cosmic microwave background radiation (CMB) in 1965 (Penzias and Wilson, 1965; Dicke et al., 1965). Observations of the CMB have since become the gold standard in terms of constraining the free parameters in the Friedmann equations, with a series of satellites of ever increasing sensitivity and resolution being launched over the past few decades (Mather et al., 1990; Spergel et al., 2003; Planck Collaboration et al., 2016). Observations of the CMB by the Planck satellite find the current contributions to the energy density are: $\Omega_{0,\Lambda} = 0.691$, $\Omega_{0,c} = 0.26$, $\Omega_{0,b} = 0.049$ ($\Omega_{0,b}$ and $\Omega_{0,c}$ denote the baryonic and dark matter contributions often included together in a matter term $\Omega_{0,m} = \Omega_{0,c} + \Omega_{0,b} = 0.31$) Planck Collaboration et al. (2016), and with a small contribution from radiation $\Omega_{0,r} \approx 10^{-5}$. $\Omega_{0,k}$, which is also present in equation 1.4, has been found to be consistent with zero, and as such is usually ignored and omitted from equation 1.4.

During the 1980s as a response to certain fine-tuning problems within the Big Bang a brief period of exponential expansion in the very early Universe known as inflation was proposed (Guth, 1981; Linde, 1983). Inflation precedes the classical picture and provides a natural solution to a variety of problems found within, such as the flatness and horizon problems. The flatness problem arises from the apparent unlikeliness of the Universe having this geometry. Unlike the negatively and positively curved geometries, a flat Universe required a very specific energy density, referred to as the critical density. Whilst the Universe could contain a slight curvature below our current detection limits, the magnitude of curvature increases over time such that with our current constraints, the Universe must have been flat to greater than 1 part in 10^{57}, which is where the picture sat at inflation's inception (Guth, 1981). Inflation explains the flatness of the universe with its exponential expansion, this works as our observable Universe is just a small patch of the totality, and whilst the entirety of it would likely have some curvature, it appears flat on small enough scales. This explanation is analogous to the Earth, in which the whole Earth is curved but on small everyday scales it appears to be flat.

The horizon problem, comes from observations of the CMB and that it is an almost perfect blackbody with only very small perturbations found. This implies that these regions were at some point in the past in thermal contact with each other, such that they could reach thermal equilibrium. The problem with this is that information, such as this cannot be transmitted faster than the speed of light. Given this constraint regions of the CMB at large distances from each other could have never been in contact with each other, leaving the fact of their almost identical temperatures unexplained. Inflation offers a natural explanation of this, before the inflationary epoch our observable Universe was just a small patch, such that it was in thermal equilibrium. Inflation's exponential expansion then causes this patch to rapidly grow in size and in doing so keeps the initial thermal equilibrium state.

Inflation also provides an explanation of the observed fluctuations within the CMB, which in turn are thought to be the seeds in which clusters and galaxies will form. Whilst inflation has become a key part of the standard picture, its experimental basis is still debated and a range of theoretical questions remain, e.g. What causes inflation to begin and ultimately end?, What is the inflationary potential?.

Following the inflationary picture, ΛCDM takes over and the FLRW metric defines the future evolution of the Universe. The very early Universe is the realm of high energy physics, with the Universe as a whole consisting of a plasma of subatomic particles. As the Universe continued to

expand and cool, these particle species began to 'freeze-out' as the energy density drops below that needed to keep the rate of particle pair production, with that of their destruction rate. At approximately 1-3 minutes after the Big Bang, Nucleosynthesis (BBN) takes place, where the densities were such that the primordial plasma began fusing protons and neutrons together to produce heavier elements. BBN produces negligible amounts of elements above Lithium due to the short timescales, and the lack of stable elements with nucleon masses of 5 and 8. As such as a result of BBN, the primordial mass fractions of the elements are dominated by Hydrogen and Helium with $\approx 75\%$ Hydrogen and $\approx 25\%$ Helium abundances with trace amounts of any larger elements with the next three most abundant being Deuterium, Helium-3 and Lithium-7 having abundances of the order of $10^{-5}, 10^{-5}, \text{and} 10^{-10}$ respectively.

1.1.2 The Cosmic Microwave Background Radiation

Between ~ 3 minutes to $\sim 400,000$ years, the Universe existed as a plasma, with the energy density on exceeding that required to ionise hydrogen. In this state, the Universe is opaque as the photons are constantly scattered and absorbed (and then re-emitted) by the plasma. As the Universe cooled, recombination occurred, and the Universe became neutral, with photons then decoupling from the now neutral gas and able travel relatively unimpeded throughout the Universe. This event is known as the last scattering surface. The last scattering surface occurred $\approx 380,000$ years after the Big Bang, when the Universe had a temperature of $T \approx 3000$K and since this epoch has cooled with the Universe's expansion giving us what we see today, with the radiation field peaking in the microwave wavelengths known as the cosmic microwave background.

The CMB is an almost perfect blackbody initially at the temperature at last scattering, but today due to cosmic expansion lies at a value of $T \approx 2.73$K. As can be seen in Figure 1.1, this value is remarkably consistent across the sky with tiny fluctuations in this value of the order of 1 part in 10,000, these small temperature fluctuations are thought to correspond to density fluctuations in the early Universe (higher temperature corresponding to denser regions), and as such are thought to be the seeds of galaxies and clusters of galaxies.

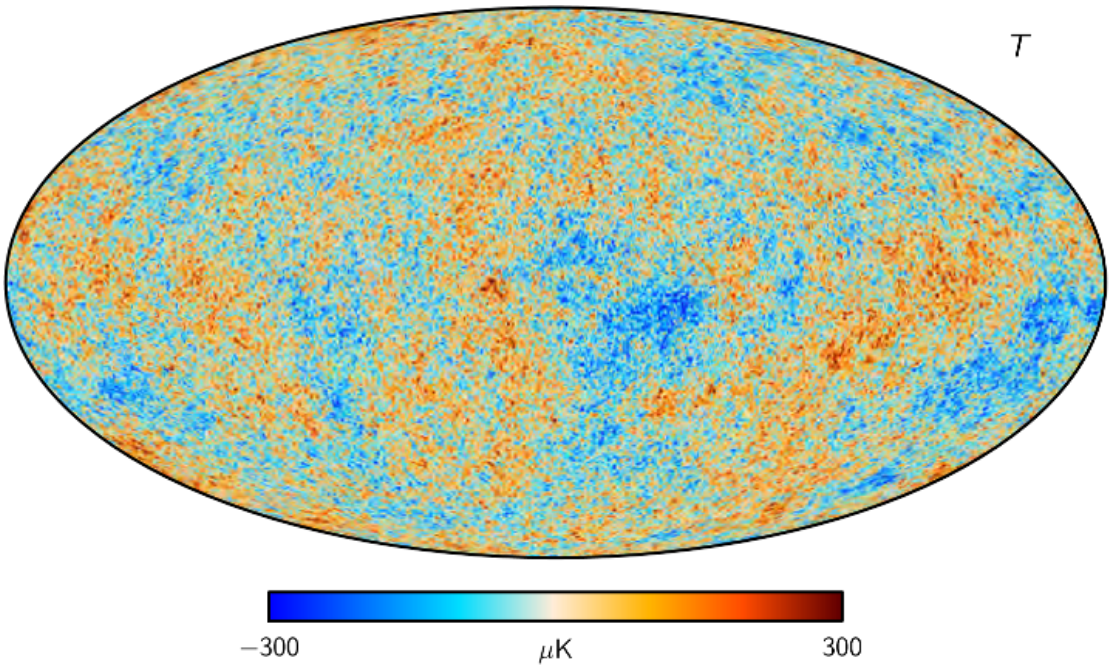

FIGURE 1.1: Planck CMB temperature fluctuation map
CMB observations from the Planck satellite. This figure is taken from Akrami et al. (2020) and is the top panel in Figure G.6 from that work. The colour map denotes temperature fluctuations across the sky, where the foreground emission has been removed replaced with a Gaussian-constrained realisation

1.2 Galaxies

Prior to the 20th century, the Milky Way was the only known galaxy. Whilst many galaxies had been previously observed, with a few being observed since ancient times (e.g. M31) their fundamental nature was not understood until relatively recently.

1.2.1 Dark Matter Halos, and the formation of Galaxies

As section 1.1.2 stated, small variations in the density of material in the early universe are thought to be the seeds of the galaxies and clusters of galaxies we see in our Universe. These initial seeds, start small but over time due to gravity these seeds grew forming large dark matter halos and the galaxies which lie within.

1.2.1.1 Dark Matter Halos

With the majority of the Universes matter being in the form of dark matter and providing the dominant source of gravity, its evolution and subsequent distribution is indispensable in our

understanding of how the baryonic matter will coalesce into the galaxies we see all around us.

From N-body simulations it has been shown that over time non-linear growth of these initial seeds grow and result in an approximately stable configuration supported against its own gravity by the random motion of the particles. The distribution of dark matter is not random, but displays a clear structure. Whilst many different profiles have been proposed to model this distribution, the most commonly applied profile is what is known as the Navarro–Frenk–White (NFW) profile, shown in Equation 1.6.

$$\rho(r) = \frac{\rho_0}{\frac{r}{R_s}\left(1 + \frac{r}{R_s}\right)^2} \tag{1.6}$$

Where ρ is the dark matter density, r is the radius from the centre of the Halo, R_s is the scale radius, ρ_0 is a characteristic density for the Halo, with both R_s and ρ_0 varying between different halos.

It is within these halos, where the baryonic matter also collects producing the stars and galaxies we observe and will be the focus of the rest of this subchapter.

1.2.1.2 Angular Momentum Exchange, Formation of Galactic Disks

In the local universe the dominant morphology of galaxies are that of disks (), that leads to the question of how they obtained their angular momentum. The classical picture presented in (Peebles, 1969), in which both the dark matter halos and the gas within, obtain their angular momentum from tidal torques from interactions with their neighbours.

In this picture, the amount of angular momentum acquired by a halo is strongly dependant on the Halo mass and the epoch in which it formed with $J \propto M^{5/3}$ and $J \propto t$ respectively where t is the lookback time (Catelan and Theuns, 1996). Unlike the dark matter halos, the gas within can cool, in the next section I will briefly describe a couple mechanisms by which this can occur, but the cooling allows the total energy to decrease however the angular momentum will be approximately conserved. As the gas collapses, this causes them to continue to collapse in the direction perpendicular to the rotation plane, and be supported against collapse in the plane by this acquired angular momentum, leading to the formation of rotationally supported disks (Mo et al., 1998).

1.2.1.3 Gas cooling

To allow the gas within the primordial galaxies to collapse and form stars, the gas first needs to cool. Star formation occurs in cold molecular gas ($\sim$ 100K), so mechanisms to cool the hot primordial gas are required.

Compton Cooling

At high redshift ($z > 6$) Compton cooling is the main cooling mechanism of the the gas within galaxies. At these high redshifts the density of CMB photons is such that interactions between the photons and the electrons within the hot plasma in the dark matter halos can significantly cool the gas. Peebles (1968) first derived the equation for this cooling timescale finding

$$\tau_{Compton} = \frac{2m_e c(1+1/x_e)}{8\sigma_T a T_{cmb}^4 (1 - T_{cmb}/T_e)}, \tag{1.7}$$

Where $x_e = n_e/ntot$ with n_e being the electron number density and n_t the number density of all the atoms and ions, a is the scale factor, T_{cmb} and T_e are the CMB and electron temperature respectively, and σ_T is the interaction cross section. As Compton cooling, unlike other cooling mechanisms requires the interaction of a single particle with a cmb photon, the cooling rate only scales linearly with the gas density (and the Compton timescale is independent of it), this is due to the CMB having a constant density throughout the universe. As such Compton cooling can occur in the dense centre of galaxies as well as the less dense outskirts, this is thought to be a significant cooling mechanism at $z > 6$ (Benson, 2010).

Molecular Cooling

Another form of cooling comes from molecular species. Before stars are able to 'pollute' the Interstellar medium (ISM) with heavier elements, this comes in the form of cooling via molecular hydrogen.

A simple explanation behind how this cooling works, is that collisions between molecules (primarily H_2 with itself or another molecule such as CO) will excite electrons within the molecules, and when the electron deexcite, a photon is emitted taking energy from the gas and thus cooling it. Molecular gas cooling unlike compton cooling, requires the collision of molecules and as such, unlike the case of compton cooling has a stronger dependence on density.

1.2.1.4 Star Formation

Arguably the most striking feature observed within galaxies are their stellar populations, with the first stars in the universe thought to have been formed ≈ 200 million years after the big bang. Whilst many questions surrounding the specifics of star formation are still up for debate, I will briefly outline a general picture of the process here.

Molecular gas is the fuel from which galaxies form their stars, and is found in structures known as giant molecular clouds (GMCs), these GMCs can remain in a state of hydrostatic equilibrium, so long as the gravitational attraction is balanced by the gas pressure of the cloud. If the gravitational attraction exceeds that of the gas pressure, either from an external trigger (such as a nearby supernova compressing the gas) or by accreting enough material, the gas cloud will begin to collapse. For a gas cloud, the mass in which it will collapse will be that of its Jeans mass

$$M_J \approx 4 \times 10^4 M_\odot \left(\frac{T}{100K}\right)^{3/2} \left(\frac{n}{cm^{-3}}\right)^{-1/2} \tag{1.8}$$

where T is the temperature of the gas cloud, and n is its density.

As the molecular cloud collapses it fragments into smaller and smaller pieces, until these fragments reach stellar masses. Up to this point much of the energy accrued by the gas, from the gravitational potential energy is radiated away, and as such the gas temperature does not significantly increase. When the fragments become small enough, the gas becomes opaque to the thermal radiation, trapping the energy, and causing the temperature of the fragments to increase until a new equilibrium is reached halting the collapse (as can be seen in equation 1.8, increasing the temperature increases the mass needed for gravitational collapse). At this stage a protostar is formed. After the formation of a protostar, it continues to accrete material further growing and heating as it accrues more gravitational potential energy, when the core reaches temperatures of ≈ 2000K, fusion can occur.

Star formation

1.2.1.5 Feedback

For decades it has been clear that Feedback is necessary and important component in the buildup of galaxies, two key reasons for this are

- The total mass density of baryonic Matter is $\Omega_{0,b} = 0.049$, whereas the total stellar mass density is $\Omega_* = 0.0023$ (Cole et al., 2001)
- The galaxy luminosity function differs from the dark matter halo mass distribution, with there being fewer low and high mass galaxies, than would be expected if dark matter halos turned a constant fraction of baryonic matter into stars. (Benson et al., 2003).

Stellar feedback

To explain the underproduction of low mass galaxies stellar feedback primarily in the form of supernovae, imparting their energy into the ISM. The energy imparted into the ISM in these low mass systems causes some of the gas to be ejected. With less gas now available to form stars, this leads to lower star formation rates than expected and as such lowers the expected number of low mass galaxies.

AGN feedback

For more massive galaxies, stellar feedback is not thought to be efficient enough to regulate the star formation enough to explain the discrepancy between the expected and observed luminosity functions. In this case AGN feedback is thought to be the main mechanism in reducing the number of the brightest galaxies. Whilst the specific mechanisms via which this feedback works is poorly understood, simple energetic arguments can be used to show the potential of AGN feedback in having profound effects on its host galaxy. If the energy imparted into the galaxy by the black hole (E_{BH}) is comparable to the binding energy of the galaxy E_{gal}, than it's clear that it could have a significant effect on the future evolution of the galaxy. If a galaxy has a velocity dispersion σ, than the binding energy is approximately $E_{gal} \approx M_{gal}\sigma^2$. The mass of the central black hole has been found to be intricately linked to the mass of the galaxy, where $M_{BH} \approx 10^{-3} M_{gal}$ (Merritt and Ferrarese, 2001; Kormendy and Gebhardt, 2001; Reines and Volonteri, 2015). Assuming a radiative efficiency of accretion of approximately 10, than the the energy released by the growth of the black hole is $E_{BH} = 0.1 M_{BH} c^2$, or $E_{BH} = 10^{-4} M_{gal} c^2$. From this we can estimate the fraction of the galaxies binding energy is released by the black hole, $\frac{E_{BH}}{E_{gal}} = 10^4 \left(\frac{c}{\sigma}\right)^2$, most galaxies have a velocity dispersion less than $500\,\mathrm{kms}^{-1}$, so $\frac{E_{BH}}{E_{gal}} > 40$, meaning the energy output of the black hole greatly exceeds that of the galaxies binding energy. If only a fraction of this energy is imparted into the gas within the galaxy, than the black hole can have a profound effect on its evolution.

More sophisticated AGN feedback proscriptions than the simple argument presented above have become an integral part of the most detailed galaxy formation models (Kauffmann and Haehnelt,

2000; Di Matteo et al., 2005; Schaye et al., 2015; Davé et al., 2019). Within these models it has been found that AGN feedback can efficiently suppress the number of galaxies at the bright end of the luminosity function and bring it into agreement with the observed distribution.

1.2.2 Hubble Tuning fork

An early attempt at classifying galaxies is the Hubble tuning fork, which separates galaxies based on morphological features in the optical, with elliptical galaxies on one side and spirals, which are split into two classes, corresponding to barred and unbarred spirals (Hubble, 1927). In Hubble's original classification, Elliptical galaxies were classified from E0-E7 measured by their ellipticity, with a spherical galaxy categorised as E0 with E1-7 indicating ever increasing ellipticity. Spirals on the other hand were separated into three separate categories based on the following criterion:

- The relative size of the unresolved nuclear region
- The extent to which the arms are unwound (The openness/angle of the spiral)
- The degree of condensation in the arms

Hubble noted that these three criteria are independent, however there was a clear correlation between the three with a few galaxies having conflicting categorisation. With these criteria, galaxies classified as spirals were given labels Sa, Sb, Sc depending on how tightly wound the spiral arms were, with the barred spirals given the same classifications but labeled SBa, SBb, and SBc, where the capital B indicates the presence of a bar. Bars are as the name suggests bar shaped structures, which are found at the centres of galaxies and composed of stars. Bars are important feature of galaxies with approximately two-thirds of spiral galaxies containing one and one-third possessing a strong one and are a efficient means of funneling gas from the outer regions of the galaxy into the centre (Bournaud and Combes, 2002). Bars vary in their strength and size, and are thought to be formed as a result of major and minor mergers (Hopkins et al., 2009, 2010; Naab et al., 2014).

Whilst most galaxies Hubble looked at were found to fit nicely into the classification scheme, some galaxies were found to be irregular in structure and were classified as such. Lenticular galaxies were unknown to Hubble at the time and were given the classification S0 placing

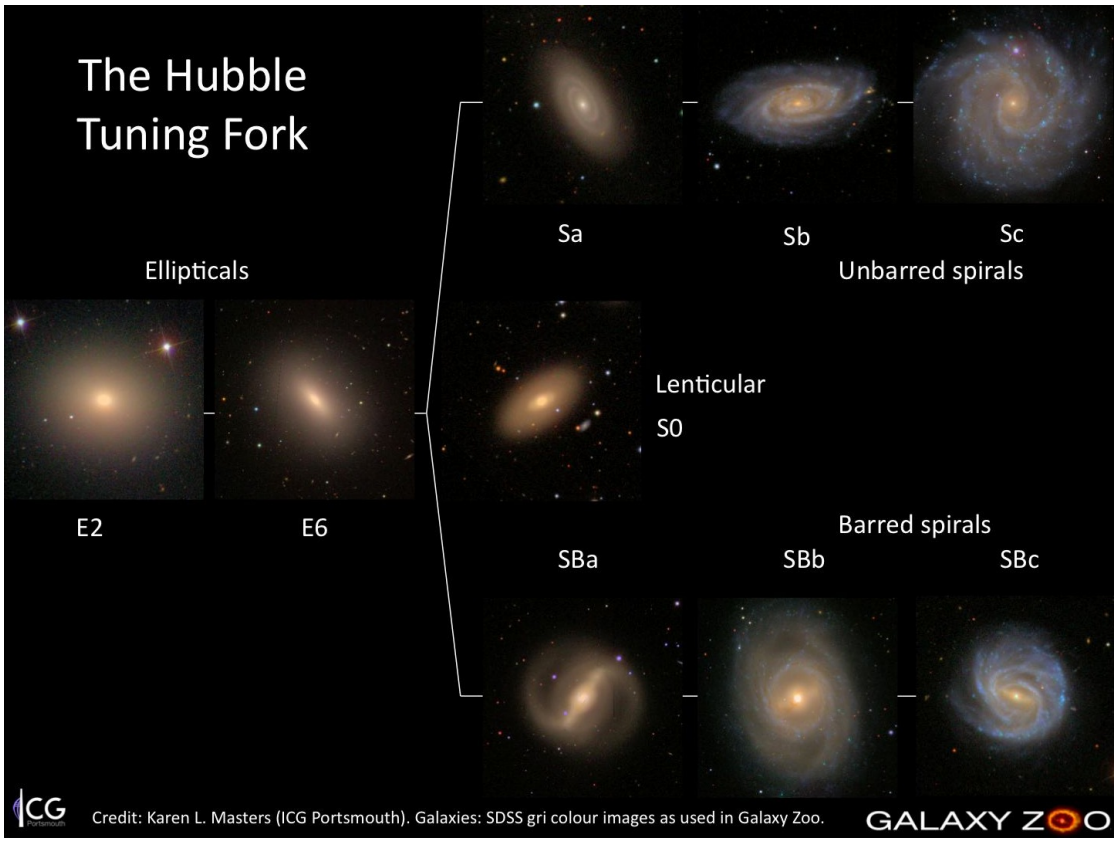

FIGURE 1.2: Hubble tuning fork
Hubble tuning fork diagram, showing examples for each of the classifications. credit: Galaxy Zoo

them at the intersection between Elliptical galaxies and the Spirals. The initial interpretation of the Hubble tuning fork was that it represented an evolutionary progression, from the Elliptical galaxies forming first and evolving into Spiral-like galaxies. This idea has since been rejected, but this and more complicated classification schemes are still an indispensable tool used in understanding galaxy formation and evolution.

1.2.3 Luminous infrared Galaxies

Luminous infrared galaxies (LIRGs) are a class of bright infrared galaxies found in the local Universe. Unlike the Hubble tuning fork classification above, LIRGs are classified not by morphology, but from their infrared luminosities. Infrared luminosities (L_{IR}) are defined over the range $8-1000\mu$m[1].

[1]Definitions of the IR luminosity, can vary with $3-1100\mu$m, being another common definition (Kennicutt and Evans, 2012).

$$\text{LIRG}: 10^{11}\text{L}_{\odot} \leq L_{IR} < 10^{12}\text{L}_{\odot}$$

$$\text{ULIRG}: 10^{12}\text{L}_{\odot} \leq L_{IR} < 10^{13}\text{L}_{\odot}$$

$$\text{HyLIRG}: 10^{13}\text{L}_{\odot} \leq L_{IR} < 10^{14}\text{L}_{\odot}$$

The infrared emission is dominated by the reprocessing of stellar light via dust, with vast quantities of dust being linked to locations of recent star formation, these large luminosities in the infrared and the close relationship between production and sites of recent star formation imply large star formation rates. Using the standard $L_{IR} - SFR$ relation in Kennicutt and Evans (2012) assuming the IR luminosity comes exclusively from sites of star formation, this corresponds to

$$\text{LIRG}: 15\text{M}_{\odot}\text{yr}^{-1} \leq L_{IR} < 150\text{M}_{\odot}\text{yr}^{-1}$$

$$\text{ULIRG}: 150\text{M}_{\odot}\text{yr}^{-1} \leq L_{IR} < 1500\text{M}_{\odot}\text{yr}^{-1}$$

$$\text{HyLIRG}: 1500\text{M}_{\odot}\text{yr}^{-1} \leq L_{IR} < 15000\text{M}_{\odot}\text{yr}^{-1}$$

A natural question to ask is what is triggering the high star formation rates in (U)LIRGs? Are these elevated star formation rates found in merging systems, are secular processes responsible?, or perhaps other environmental conditions such as the galaxies' location within a cluster could provide an explanation.

Studies of (U)LIRGs have found that in the local Universe, ULIRGs are almost exclusively mergers, and this fraction decreases with decreasing IR luminosities (Sanders et al., 1988; Veilleux et al., 2002). Larson et al. (2016) for example with a sample of 65 local (U)LIRGs found that above $L_{IR} > 10^{11.5}$ all of their sample were mergers, but below this single galaxies rapidly start to dominate with $\approx$40% at $10^{11.3}\text{L}_{\odot}$ and $> 80\%$ at $10^{11.1}\text{L}_{\odot}$. The fact that the highest star forming galaxies in the local Universe are a result of mergers is not surprising as mergers or close flybys work to compress and shock the gas within the interstellar medium (ISM) leading to many new sites of star formation (Kim et al., 2009; Saitoh et al., 2009).

1.2.4 Interstellar Medium

Whist the stellar component of galaxies typically dominates much of the emitted light (note as previously mentioned in IR bright sources this is not the case), ISM constitutes a large part of the internal galaxy structure, containing the fuel for future star formation and holding the key to understanding much about their past evolution. The ISM is an overarching term to describe all of the contents of the space within galaxies between its stars. The ISM is primarily made up of Hydrogen and Helium, polluted by metals produced by previous generations of stars. The ISM can be separated into different components based on the density and temperature of the gas.

1.2.4.1 Ionised ISM

The ionised ISM refers to the regions in which hydrogen has been ionised ($E_n = 13.6eV$). This component can be further subdivided into two separate sub-components: the warm ionised medium (WIM), which describes the diffuse component typically consisting of densities of the order of $0.1 cm^{-3}$ and the denser H_{II} regions which lie within molecular clouds at sites of recent star formation, ionised by the massive stars found within.

1.2.4.2 Molecular ISM

The molecular component of the ISM is of unique importance due to it being central in the star formation process. Stars form out of the cool ($< 100K$) molecular gas within galaxies (Elmegreen, 2012), and as such there is a strong relationship between a galaxy's molecular gas abundance and its resulting star formation rate. Starting with Schmidt (1959), it was found that there was a close relation between a galaxies star formation rate surface density and that of its gas surface density, more recent analyses such as that in de los Reyes and Kennicutt (2019) have found that the relationship known as the Kennicutt-Schmidt law and is parameterised by the following power law:

$$\Sigma_{SFR} = A\Sigma_{gas}^{N} \tag{1.9}$$

where Σ_{SFR} and Σ_{gas} correspond to the SFR and gas surface densities, with A and N being the normalisation and slope of the relation. Kennicutt (1998) found that this relation holds over a large range of gas densities and SFRs with an exponent $N \approx 1.4$. The consistency of this relation has meant that this and slight modifications of this relation (such as the inclusion of the

dynamical time) are used throughout the literature and are used to determine the star formation within most cosmological simulations. With star formation being an important part of galaxy formation and evolution, this relation is an important ingredient in such simulations (see e.g. Schaye et al., 2015; Davé et al., 2019).

Whilst the exponent of the relation for molecular gas more generally is found to be N$\approx$ 1.5 a more direct relation between the molecular gas and star formation within a galaxy can be found, with dense molecular gas. Dense molecular gas is usually defined as that of gas at densities exceeding $10^4 \mathrm{cm}^{-3}$, and is thought to be the gas densities in which star formation will be actively occurring. Gao and Solomon (2004) using the sub-mm ground state HCN emission, which traces gas at densities $\mathrm{n}(\mathrm{H}_2) > 3 \times 10^3 \mathrm{cm}^{-3}$ found a strong linear relation between the IR luminosity (and hence SFR) and the HCN(1-0) line luminosity. This pioneering work has since been extended further into sub-galactic scales (see e.g. Krips et al., 2008; Jiménez-Donaire et al., 2019) and into the ULIRG regime (see e.g. Privon et al., 2015; Bigiel et al., 2016), now spanning over many orders of magnitude in IR luminosity.

Much of these detections have been limited to low-z sources, more recent work presented in Rybak et al. (2022) attempted to detect the ground state emission in a small sample of lensed SMGs. Whilst no clear detections of the ground state were found, one source had a tentative detection, and the HCN/LIR ratio from the limits were consistent with that of local $z \sim 0$ ULIRGs, but lower than expected for the aforementioned linear relation. This could be hinting at a deviation from the linear relation at high SFRs, which has been predicted by various models (Krumholz and Thompson, 2007; Narayanan et al., 2008).

1.2.4.3 Dust

The final important ingredient in our discussion of the ISM is dust. Historically the understanding of dust and its behaviour was driven by the need to obtain accurate colours and fluxes of objects due to its obscuring nature (Li and Greenberg, 2003). In recent years dust has become more important as a diagnostic tool, with observatories built with the purpose of observing the thermal emission from it. Understanding of dust is especially important in the case of IR bright galaxies, which are known to contain a large quantity of dust attenuating the stellar light, and constitutes the majority of the emission from these sources.

Whilst the primary production route of dust grains is still up for debate, it is clear that it is produced in a range of sources/environments such as the atmospheres of Asymptotic Giant Branch (AGB) stars (e.g. Ferrarotti and Gail, 2006; Di Criscienzo et al., 2013), cold dense regions of the ISM and ejecta from core collapse supernovae (Todini and Ferrara, 2001; Sarangi and Cherchneff, 2013). Once created, dust evolves by physical processes, which can both help them grow, such as accretion of gas phase metals in dense molecular clouds (Inoue et al., 2016; Köhler et al., 2015) and also facilitate their destruction such as in supernovae shocks, thermal spluttering, and collisions between dust grains (e.g. Draine and Salpeter, 1979; Jones and Nuth, 2011; Bocchio et al., 2014).

1.2.5 The Initial Mass Function

The initial mass function (IMF) is arguably the most important parameter used to interpret our astronomical observations. All derivations of star formation rates, stellar masses, etc. are all dependent on this. The IMF as the name suggests is a measure of the distribution of the initial masses of stars that form in a star-forming environment. As individual stars are practically unobservable outside of the Milky Way and a handful of other galaxies (such as Andromeda and the Magellanic clouds), all direct measurements of it come from these.

IMFs are typically parameterised with power laws, with different IMFs opting for a different number of these to describe various mass ranges, as shown in Table 3.1. The number of stars dN in the mass interval m to $m + d(log(m))$ is therefore given by the following equation.

$$dN \propto m^{\alpha-1} d(log(m)) \tag{1.10}$$

Where α depends on the specific IMF. Starting in the 1950s with work by Edwin Salpeter, who observed stars from G7 to B0 (or stars in the mass range $\sim 1 - 10\mathrm{M}_{\odot}$), found that they could be described by a single power law with a slope of $\alpha = 2.35$ (Salpeter, 1955). Since this work a range of different IMFs have been proposed, with a range of different values for the slope, as well as offering a combination of slopes in different mass ranges (Kroupa et al., 1993; Kroupa, 2001; Chabrier, 2003). Fig 1.3 shows a range of different IMFs with Table 1.1 providing the parameterisations for these.

IMF	Kroupa 1993	Kroupa 2001	Kroupa 2003	Salpeter	Chabrier
M_0	0.1	0.1	0.1	0.1	0.1
M_1	0.5	0.5	0.5	0.5	0.5
M_2	1	1	1	1	1
M_3	100	100	100	100	100
α_0	1.3	1.3	1.3	2.35	- *
α_1	2.3	2.3	2.3	2.35	- *
α_2	2.7	2.3	2.35	2.35	2.3
$M_{>8M_\odot}/M_{tot}$ [%]	8.6	26.1	23.6	13.9	29
Relative Star formation rates	3	1	1.1	1.6	0.9

TABLE 1.1: Parameterisations and relative SFRs of various IMFs in the literature
Parameterisations of Initial Mass Functions that are popularly used in the literature. * The Chabrier IMF is typically parameterised as a log-normal distribution below $M< 1M_\odot$, with the form $\xi(m) = 0.158(1/(m\ln(10)))\exp[-(\log(m)-\log(0.08))^2/(2\times 0.69^2)]$.

As can be seen in Figure 1.3, the high mass slope ($M > 1M_\odot$), is typically parameterised similarly to the Salpeter IMF with a slope of $\alpha_2 \approx 2.3$ with the majority of the variation coming from the low mass end. However there appears to be two camps for the high mass end, with one camp following the Salpeter slope and the other giving a steeper slope of $\alpha_2 \approx 2.7$ first given in Scalo (1986), and typically arises from the different methods used to constrain it (field vs YSO counting).

In the extragalactic Universe, the most commonly adopted IMFs are the Salpeter, Kroupa [2], and Chabrier IMFs all which have a high mass slope of $\alpha \approx 2.3$. Despite their similar high mass slopes these IMFs differ more substantially in their parameterisations of the low mass end. The Chabrier IMF paramaterises the low mass end with a single log-normal distribution below $1M_\odot$, and the Kroupa IMFs opt for extra power law components. For the majority of extragalactic purposes, the Chabrier and Kroupa are in effect interchangable due to their similar mass-to-light ratios, resulting in comparable SFRs as seen in Table 1.1.

1.2.5.1 High-z IMF

Whilst the IMF in the Milky Way a handful of over local (dwarf) galaxies have directly constrained the IMF, outside of this limited range only indirect methods can be used to attempt to

[2]There are multiple Kroupa IMFs in the literature, the ones of note here are Kroupa (2001) where $\alpha_2 = 2.3$ and Kroupa and Weidner (2003), where $\alpha_2 = 2.35$

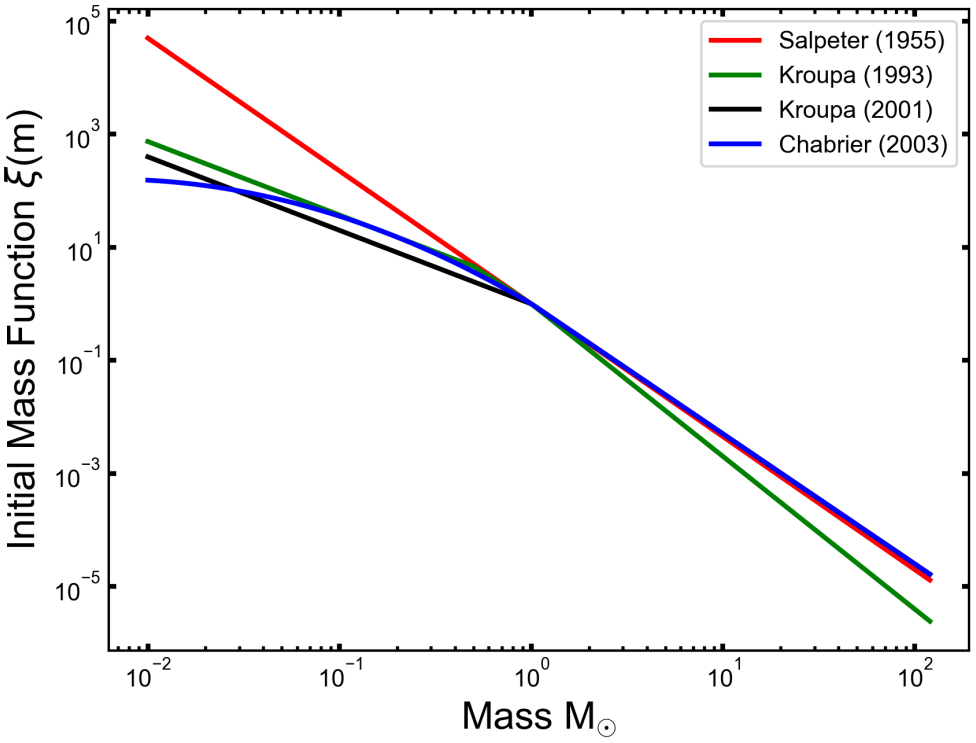

FIGURE 1.3: Commonly adopted IMFs in the literature
Initial Mass Functions that are popularly used in the literature. Most agree well with the canonical Salpeter slope ($\alpha_2 \approx 2.3$), except Kroupa et al. (1993), which has a Scalo (1986) like high mass slope and is typically used in some chemical evolution models (see e.g. Romano et al., 2017, 2019), though the more standard Kroupa (2001) is also used (see e.g. Kobayashi et al., 2011, 2020)

constrain the IMF, with mixed results. Rather than the direct young stellar object (YSO) counting, extragalactic attempts to constrain the IMF often work by comparing a few IMFs to certain properties of galaxies, and see how well the predictions of the IMF match to the observations.

Work on giant elliptical galaxies have typically found evidence of a bottom-heavy IMF in the inner regions by analysing mass to light ratios. This approach requires a luminosity independent way of obtaining stellar mass, such as modelling the stellar kinematics or by observing the deflection of light from a background source, coupling this with a mass to light ratio expected for a standard IMF (typically Kroupa (2001) or Chabrier (2003)). If there is a discrepancy between the two values can be explained either by an excess in stellar remnants (e.g. black holes) or via an excess in brown dwarfs, i.e. a top-heavy/bottom-heavy IMF Smith (2020).

Sub-mm galaxies often thought to be the precursers of the local massive ellipticals, are another class of galaxies in which a heavy-IMF has been inferred (usually a top-heavy IMF is argued)

(Baugh et al., 2005; Zhang et al., 2018b; Romano et al., 2019). For SMGs different methods/arguments have been employed to probe the IMF, early arguments like that presented in Baugh et al. (2005) come from the sub-mm number counts, which measure the 850μm number counts of sub-mm emitting sources, and the apparent inability of a canonical IMF to reproduce the numbers observed. Baugh et al. (2005) found that in their models, they could match both the SMG number counts and the number counts of lyman break galaxies (LBGs), this was the first model able to match both of these populations with previous failing on one or both of these counts. They did this by invoking a top-heavy IMF within bursts of star formation. More recent work on the number counts have alleviated this problem significantly with Cai et al. (2020) and Lovell et al. (2021) finding general agreement with the sub-mm number counts assuming a canonical IMF.

A second approach to constraining the IMF in sub-mm galaxies, comes from observing chemical isotopes of carbon and oxygen, due to their different formation routes where ^{13}C is thought to be produced in intermediate mass stars ($1-4$M$_{\odot}$) and ^{18}O is thought to be produced in massive stars (>8M$_{\odot}$), the relative abundances of these two isotopes should be sensitive to the high mass slope of the IMF (α_2), this approach has more recently been studied in detail in Zhang et al. (2018b), for a sample of SMGs via the rotational transitions of ^{13}CO and C^{18}O, and will also be discussed in more detail in chapter 4

1.2.6 Sub-mm Galaxies

Sub-mm Galaxies (SMGs) are so named due to their brightness at sub-mm wavelengths and their faintness in many of the optical bands, are a class of extreme star forming galaxies found in the high-z ($z>1$) Universe. With the advent of a powerful new generation of sub-mm detectors such as SCUBA on the JCMT in the 1990s (see below), it finally became possible to detect these extreme systems with a multitude of papers (Smail et al., 1997; Hughes et al., 1998) detailing the discovery of this previously unknown population of galaxies. With star formation rates of $100-1000$M$_{\odot}$yr^{-1} (Chapman et al., 2010) typically found (assuming a standard Initial Mass Function see section 1.2.5 for a discussion), SMGs are seen as high-z analogues of the local ULIRGs observed in the local Universe.

1.2.6.1 Sub-mm Spectral energy distribution

For a perfectly absorbing body, one would expect the thermal emission to be in the form of blackbody radiation as given in equation 1.11, however in most astronomical situations including dust emission this is a poor approximation.

$$B_\nu(T) = \frac{2\nu^2}{c^2} \frac{h\nu_{obs}}{e^{h\nu(1+z)/kT} - 1}, \tag{1.11}$$

Thermal dust emission is more accurately modelled by a modified blackbody, which includes an extra component to the conventional blackbody formula to model the emissivity or optical depth of the dust clouds, typically of the form $1 - e^{-\tau}$, with $\tau = \left(\frac{\nu_{em}}{\nu_0}\right)^\beta$ where τ is the frequency dependent optical depth of the dust emission, ν_{em} is the emitted frequency of the light (for a redshifted source this is typically replaced by the observed frequency where $\nu_{em} = \nu_{obs}(1+z)$), and ν_0 is the frequency in which the dust opacity reaches unity. Giving us the modified blackbody formula 1.12.

$$B_\nu(T) = \frac{2\nu^2}{c^2} \left(1 - e^{\left(-\frac{\nu_{obs}*(1+z)}{\nu_0}\right)^\beta}\right) \frac{h\nu_{obs}}{e^{h\nu(1+z)/kT} - 1}, \tag{1.12}$$

1.2.6.2 Negative k-correction

A key advantage of observing at sub-mm wavelengths is the negative k-correction of SMGs. The necessity of applying a k-correction arises from the fact that observing objects which lie at different redshifts with the same frequency, are measuring different parts of the rest frame SED.

For an object at $z \approx 0$ the relationship between apparent and absolute magnitude can be expressed as the following:

$$m = M + 5log_{10}\left(\frac{D_L}{10pc}\right) \tag{1.13}$$

where D_L is the luminosity distance, extending this to objects at $z > 0$, a k-correction component is required due to the observed frequency and the emitted (or obs) frequency no longer being the same ($\nu_{obs} \neq \nu_{em}$).

$$m_{obs} = M_{rest} + 5log_{10}\left(\frac{D_L}{10pc}\right) + K_{rest,obs} \tag{1.14}$$

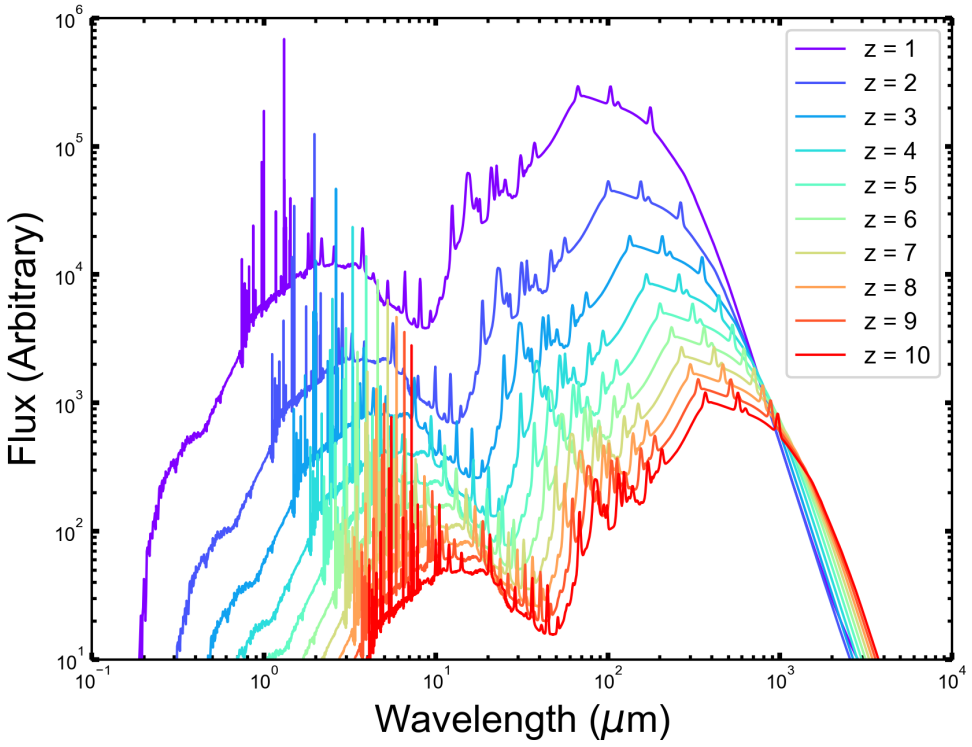

FIGURE 1.4: Example SMG spectral energy distribution
Example SED for a sub-mm bright galaxy from the SED fitting code Prospector, Prospector does not currently include sub-mm emission lines with the 88μm [OIII] being the longest wavelength transition currently included.

in this form, $K_{rest,obs}$ is the k-correction, and is dependant on the redshift of the source and the shape of the SED between the two frequencies ν_{obs} and ν_{obs}.

For sub-mm galaxies in particular, where the SED is well modelled by a equation 1.12, the flux will remain approximately constant throughout a wide range of redshifts. This is true as long as we stay within the Rayleigh-Jeans tail of the SED, in this regime equation 1.12 becomes (as the flux units are typically not given in magnitudes for sub-mm wavelengths here I will work in units of flux density)

$$B_\nu(T) = \frac{2(\nu_{obs}(1+z))^2 k_B T}{c^2}\left(1 - e^{\left(-\frac{\nu_{obs}*(1+z)}{\nu_0}\right)^\beta}\right) \tag{1.15}$$

and as $\nu_{obs}(1+z) \ll \nu_0$, the optical depth term can be rewritten as $1 - e^{-\left(\frac{\nu_{obs}*(1+z)}{\nu_0}\right)^\beta} \approx \left(\frac{\nu_{obs}*(1+z)}{\nu_0}\right)^\beta$ giving us the final approximate form of the SED in the Rayleigh-Jeans tail of

$$B_\nu(T) = \frac{2(\nu_{obs}(1+z))^{2+\beta} k_B T}{c^2 \nu_0^\beta} \propto (1+z)^{2+\beta} \tag{1.16}$$

As the measured flux drops by drops with the luminosity distance squared, which has a $((1+z)^2)^2$ or $(1+z)^4$ dependence, the final measured flux is proportional to

$$S_{\nu_{obs}} \propto (1+z)^{\beta-2} \tag{1.17}$$

Observational and theoretical modelling of dust emission typically find a value of $\beta \approx 2$ (typically between 1 and 3)(Blain et al., 2002). With $\beta \approx 2$ equation 1.17 tells us that the observed flux $S_{\nu_{obs}}$ becomes constant.

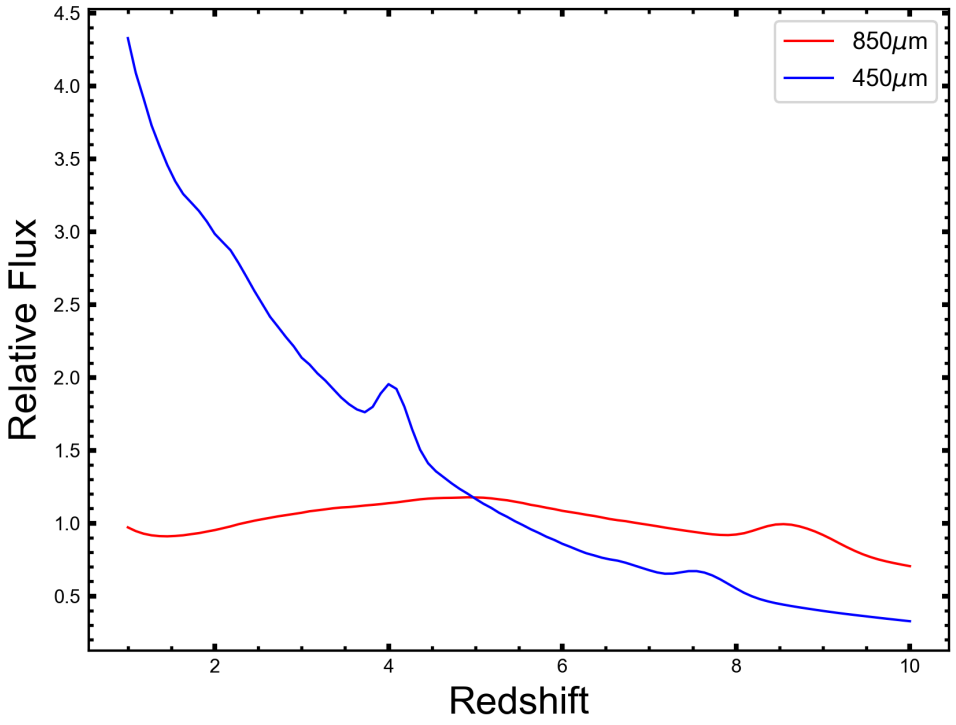

FIGURE 1.5: K-correction at 450μm and 850μm
Measured flux for the Prospector example SED for a range of redshifts for 450μm and 850μm convolved with the JCMT Band-pass. Peaks in the resultant values at particular wavelengths correspond to emission lines in the Prospector model. flux is normalised such that the median value for each wavelength is 1.

Figure 1.5 shows the expected k-correction for the two different observing wavelengths for the JCMT (450μm and 850μm), convolved with the JCMT band-passes. Due to the 450μm lying closer to the peak of the SED and not in the Rayleigh-Jeans tail the above argument does

not apply, however in the case of the 850μm observations, it can be seen that the measured flux density is approximately constant throughout a wide range of redshifts ($z \approx 1-10$). The negative k-correction for 850μm allows SMG to be studied across cosmic time without a strong redshift dependent brightness limit.

1.3 Sub-mm Astronomy

1.3.1 The advent of sub-mm astronomy

Astronomy is an ancient science with humans observing the night sky for thousands of years. For almost all of that time, we were limited to observations in just the optical. With the discovery of infra-red light in the early 1800s (Walker, 2000) it became clear that the light we see consisted of just a small fraction of the total electromagnetic (EM) spectrum.

In the 200 years or so since this discovery astronomy has been revolutionised by technological advances in detectors of these previously unseen wavelengths, gamma ($< 10^{-11}$m), sub-mm ($0.3-1.0$mm), etc. In the last few decades of the 20th century, a range of observatories designed for the sub-mm wavelengths came online, such as the James Clerk Maxwell Telescope (JCMT) in 1987 in Hawaii and more recently arrays, such as the Atacama Large Millimetre/Submillimetre Array (ALMA) in Chile in 2011. Unlike optical wavelengths which detect the direct emission from stars, gas and AGN, sub-mm wavelengths are dominated by the reprocessing of stellar light by dust grains, by absorbing the incident light from the stellar populations and re-emitting it as thermal radiation in the infrared. For illustrative purposes I will outline a brief calculation of how this process works for a single dust grain $\approx$ 10pc from a A-type star.

At the heart of this calculation is that of energy conservation, with the dust grain absorbing the incoming light from the star, heating, and then re-emitting this energy as thermal radiation. The dust grain will continue to heat until it reaches thermal equilibrium.

Assuming that the spectral energy distribution (SED) from the star is a blackbody, we can use the Stefan-Boltzmann law which states

$$I = \sigma T^4 \tag{1.18}$$

Where I is the flux, σ is the Stefan-Boltzmann constant and T is the temperature of the emitting object which in our case this will be the star (T_{star}) and the dust grain (T_{dust}) once it has been heated.

For a star of radius R_{star}, the luminosity L_{star} is given by

$$L_{star} = 4\pi R_{star}^2 \sigma T^4 \tag{1.19}$$

and for a typical dust grain of size r located at distance D from the star, approximating the absorbing area as a circular region of radius (r). We can approximate the flux absorbed I_{ab} as

$$I_{ab} = \frac{L_{star} r^2}{4D^2} \tag{1.20}$$

Which applying the Stefan-Boltzmann law for the star this becomes

$$I_{ab} = \frac{\pi R_{star}^2 \sigma T_{star}^4 r^2}{D^2} \tag{1.21}$$

As energy is conserved, the luminosity of the dust grain L_{dust}, once thermal equilibrium has been reached must match the incident flux absorbed so $I_{ab} = L_{dust}$. This means that I_{ab} in Equation 1.21 can be replaced by L_{dust} giving

$$L_{dust} = \frac{\pi R_{star}^2 \sigma T_{star}^4 r^2}{D^2} \tag{1.22}$$

Assuming that the emission from the dust grain is also that of a blackbody (this is reasonable for individual dust grains but in the case of a large number of dust grains each of which will absorb emitted light from other dust grains, the ensemble is better described by a modified blackbody, see Section 1.2.6.1), we can again apply the Stefan-Boltzmann law, this time to the dust grain. This gives us

$$4\pi r^2 \sigma T_{dust}^4 = \frac{\pi R_{star}^2 \sigma T_{star}^4 r^2}{D^2} \tag{1.23}$$

which as can be seen, simplifies to

$$T_{dust} = \left(\frac{R_{star}^2 T_{star}^4}{4D^2} \right)^{1/4} \tag{1.24}$$

or in a simpler form

$$T_{dust} = T_{star} \sqrt{\frac{R_{star}}{2D}} \tag{1.25}$$

putting in reasonable numbers for our stars parameters, $T_{star} = 8000$K, $R_{star} = 1.8\mathrm{R}_{\odot}(1.3 \times 10^9\mathrm{m})$ which is the approximate temperature and radius for an A-type (A5V) star, and $D = 10$pc $(3.086 \times 10^{17}\mathrm{m})$ we obtain the equilibrium temperature of the dust grain to be $T_{dust} = 0.5$K. This is approximately a factor of 5 below the typically observed dust temperatures of $20-40$K however dust grains will lay at varying distances from stars, which also vary greatly in luminosity. As such this calculation should only be viewed as an illustration of the principles.

A significant limitation of observing with a single dish in the sub-mm wavelengths are resolution constraints. For a diffraction limited telescope the equation that determines the resolving power is:

$$\Delta\theta = \frac{1.22\lambda}{D} \tag{1.26}$$

where λ is the wavelength of the observed light and D is the diameter of the dish. To illustrate the magnitude of the effect, for the JCMT with a 15m dish, the diffraction limited resolution for observations at 450μm is $\sim 8''$, compared to Hubble, which has a 2.4m mirror observing mostly in the optical, the diffraction limit at 500nm is $0.05''$. As the resolution increases linearly with the dish, to obtain Hubble type resolutions would require a infeasibly large dish of $\sim$ 2km, thus alternative methods to obtain comparable resolutions are required.

1.3.2 Interferometry

To overcome the resolution limits of single dish observatories, a technique called interferometry can be used. Interferometers typically overcome this limitation by using many single dish antennae linked together to form an array, this produce an effective telescope with a size defined by the largest separation between any two dishes in the array. Equation 1.27 therefore becomes

$$\Delta\theta = \frac{1.22\lambda}{B} \tag{1.27}$$

Where B is the largest separation between two dishes. Figure 1.6 shows a simple schematic for a two dish inteferometer, but the principles can be applied to an arbitrary number of dishes.

Two-dish Interferometer Starting with the simple case of observing a source with a two dish interferometer as shown in Figure 1.6. From Fig 1.6 we have a plane wave arriving at telescope i and j, which are separated from each other by the vector $\mathbf{B}$. The path delay between the two waves are given by $\mathbf{B}.\mathbf{s}$ with $\mathbf{s}$ being the unit vector in the direction of the source and the phase shift being given by $k\mathbf{B}.\mathbf{s}$ where $k = 2\pi/\lambda$.

If the electric field received at the first dish is E, than the second dish will receive an electric field $Ee^{ik\mathbf{B}.\mathbf{s}}$ due to the phase delay. Multiplying these signals together electronically and then adding together the fringe patterns across the source we arrive at the response R of the interferometer

$$R = \int I(\sigma) e^{ik\mathbf{B}.(\mathbf{s}+\sigma)} \tag{1.28}$$

Where $I(\sigma)$ is the intensity of the source and $(\mathbf{s}+\sigma)$ is the vector in the direction of a particular part of the source (which would have an intensity $I(d\sigma)$.

As $e^{ik\mathbf{B}.\mathbf{s}}$ is a result of the array configuration and not dependent on the source we can remove this from the integral giving

$$R = e^{ik\mathbf{B}.\mathbf{s}} \int I(\sigma) e^{ik\mathbf{B}.\sigma} d\sigma \tag{1.29}$$

and further to this as can be seen in Figure 1.6 σ is parallel to the projected baseline vector $\mathbf{b}$, which allows us to use the following relation $\mathbf{B}.\sigma = \mathbf{b}.\sigma$, giving us a more useful form for the response

$$R = e^{ik\mathbf{B}.\mathbf{s}} \int I(\sigma) e^{ik\mathbf{b}.\sigma} d\sigma \tag{1.30}$$

This leaves us with a set of fringes (contained in the term $e^{ik\mathbf{B}.\mathbf{s}}$) and the integral component that is of interest ($\int I(\sigma) e^{ik\mathbf{b}.\sigma}$). As $\mathbf{B}$ and $\mathbf{s}$ are known, a phase rotation is applied to remove this component, which in radio interferometry usually involves adding electronic delays to the signals.

By decomposing $\mathbf{b}$ and σ into their coordinates such that $\sigma = \sigma_x\mathbf{i} + \sigma_y\mathbf{j} = x\mathbf{i} + y\mathbf{j}$ and $\mathbf{B} = u\mathbf{i} + v\mathbf{j}$ giving

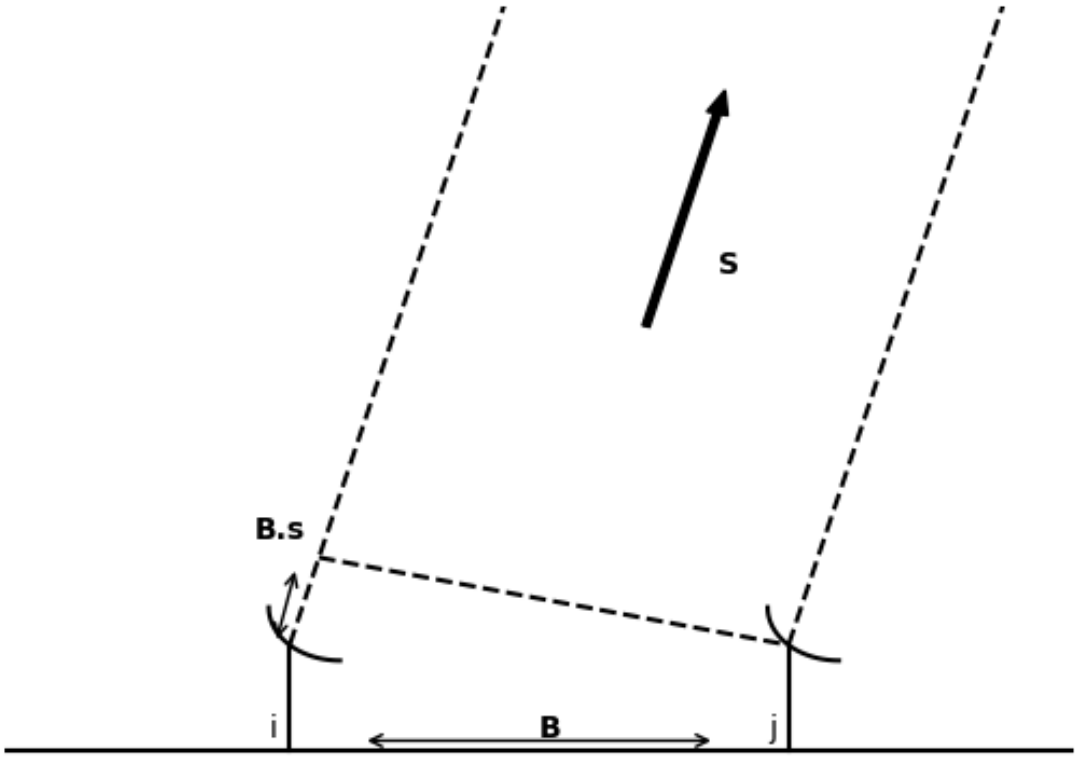

FIGURE 1.6: Two dish interferometer schematic
Simple Schematic of a two dish interferometer. Where i and j are the different dishes, B is the distance between them, $\mathbf{B}.\mathbf{s}$ corresponds to the path difference between the signal received at i and j and S is the direction to the source.

$$R(u,v) = \int I(x,y) e^{2\pi\, i\mathbf{b}.(ux+vy)} dxdy \tag{1.31}$$

This is the familiar Fourier transform, where k becomes 2π as u and v are in wavelength units. The choice of decomposition for $\mathbf{b}$, may seem unusual, however it has a fairly simple interpretation, with one component being parallel to the equator at the nearest point to the source and the second component, parallel to this point and the North Pole. By choosing this decomposition we naturally arrive at the Fourier transform simplifying future calculations.

Filling the uv plane

The key to obtaining good interferometric data, is an understanding of the *uv* plane. The *uv* plane is inversely proportional to physical scales on the sky, which means larger separations in *uv* space correspond to information about smaller physical scales. As can be seen in Figure 1.7, for short integration times, the *uv* plane consists of many points, these correspond to all the various separations of each of the antenna with respect to every other. Many gaps exist in the

uv plane, which means information about a range of spatial scales will also be missing. Ideally there will be no gaps in the *uv* plane over range of scales required for your observations. This is the case for a single dish observation, however as discussed its completely infeasible to build a single dish of the order of a few kilometres. Due to this other ways of filling the *uv* space are required, this is achieved by increasing the number of antennae in the array, as well as taking longer exposures of the source. With increased integration times, the Earth rotates throughout an observation, this rotation changes the relative separations between the antennae which means the *uv* separations also change leading to further population of the *uv* plane. Figure 1.8 gives an example of this effect, by simulating an ALMA observation, similar to the one shown in Figure 1.7, but this time for an integration time of approximately 5 hours. As can be seen, the *uv* plane is considerably more sampled, leading to less 'missing' information across the scales sampled by the synthetic observations. Imaging directly (applying the reverse Fourier transform to return to the *xy* sky plane) using the sampled *uv* plane, gives us what is known as the dirty image.

The CLEAN algorithm

Even in ideal situations the *uv* plane will have gaps, and as we want to be able to image more and more in shorter and shorter integration times, this requires algorithms to take our incomplete *uv* space and produce an accurate image, without artefacts from this incomplete sampling. The CLEAN algorithm, first developed by Högbom (1974), revolutionised radio interferometry. The algorithm and its descendants remain the primary methods used in imaging interferometric data. CLEAN is a non-linear algorithm, which works iteratively starting with the dirty map (I_0), adding a delta function to the position with the largest residual flux (The largest flux value in the region of the map without the source). The response of the antennae to this delta function is then subtracted to produce a new image (I_1), this procedure is then repeated until either the maximum number of iterations is met or until the residuals fall below some preset threshold (e.g. the noise level of the dirty image), giving a final image I_n. When either of these conditions are met it is assumed that the residual values constitute the noise within the observations.

Visibility weighting

When creating an image, interferometric observations allow us to add weightings to the sampled points within the *uv* plane. A simple case would be to weight all of the sampled *uv* plane equally ($W(u,v) = 1$) and all the unsampled regions weighted as zero ($W(u,v) = 0$). In most situations, however, various different weighting schemes are employed to the *uv* plane, the most popular of which are:

Natural Weighting: This weighting scheme can be expressed as $W(u,v) = \frac{1}{\sigma^2}$ (where σ is the noise in the image) for regions with *uv* sampling and 0 outside this range. As there is typically more noise from the longer baselines and hence smaller angular resolutions, this weighting scheme prioritises the sensitivity of the observations whilst reducing the resultant resolution.

Uniform Weighting: This scheme weights the *uv* points inversely proportional to the 'local' density of the *uv* points. As shorter baselines tend to be better sampled than longer baselines, this leads to longer baselines being weighted up, thus reducing sensitivity but increasing the resultant resolution.

Briggs Weighting: This weighting scheme provides a compromise between the two aforementioned weightings with

$$W(u,v) = \frac{1}{\sqrt{1 + \frac{S_N^2}{S_{thresh}^N}}} \tag{1.32}$$

Where S_N^2 is the natural weight for the cell and S_{thresh}^N is known as the robust parameter, this value can be tuned to offer the best compromise between sensitivity and resolution.

1.3.2.1 Atacama large millimetre/sub-millimetre array

As this thesis makes use of one interferometer in particular, it is of relevance to provide a brief outline of it here. ALMA is as its name suggests an interferometer that observes in the sub-millimetre and millimetre wavelengths and is located at an altitude of $\approx$ 5000m in the Atacama desert in Chile. ALMA began operations in 2011 and as of now consists of 66 antennas, 54 of which measure 12m in diameter and the remaining 12 measuring 7m. It offers spectral coverage from approximately $30 - 950$GHz ($0.3 - 10$mm). By using these antennas in different configurations with baselines up to 16km, ALMA can offer a range of resulting resolutions from a few arcseconds in more compact configurations down to a few milliarcseconds in extended configurations.

[3]These figures were created using the ALMA observation support tool, which can be found at the following link: https://almaost.jb.man.ac.uk

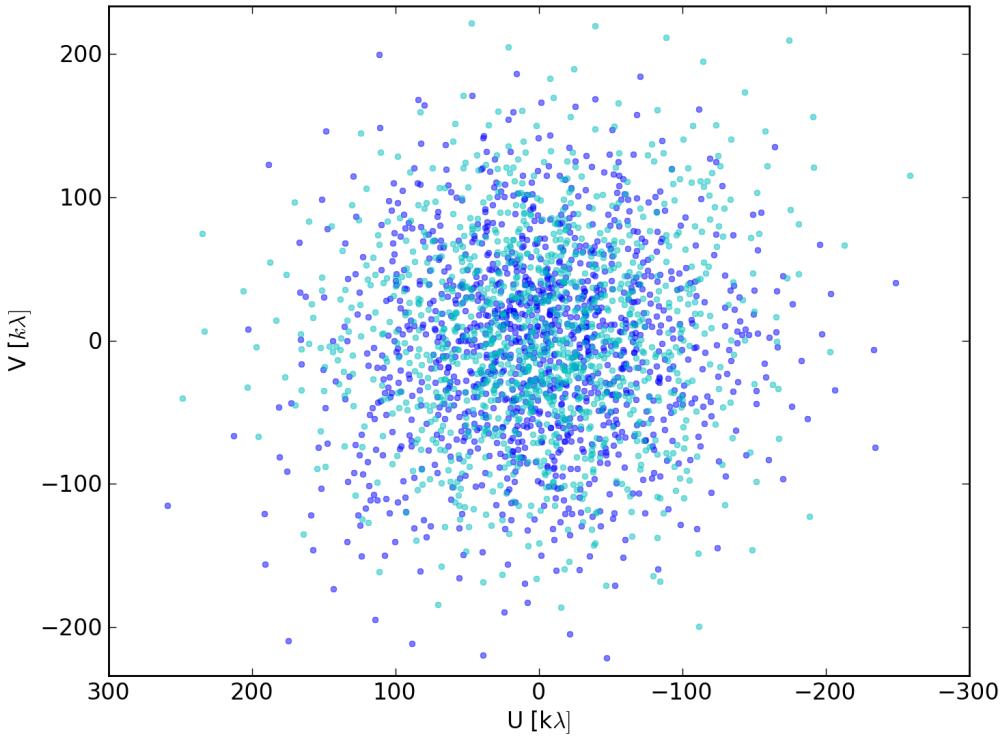

FIGURE 1.7: *uv* plane short exposure
uv plane of a simulated ALMA observation, with an integration time of 20s. The short integration time means that the *uv* plane is dominated by the initial positions of the antennae. The *uv* plane has many gaps corresponding to spatial separation gaps within the array configuration.[3]

1.4 Gravitational Lensing

At high-z the sensitivity and resolution limits of observatories place more stringent limits on what can be observed. Gravitational lensing offers a way to overcome these challenges by magnifying the flux and spatial scales of distant galaxies.

The bending of light in a gravitational field was the first detected during the 1919 Solar eclipse (Dyson et al., 1920), and provided the first direct confirmation of Einstein's general theory of relativity by observing the subtle shift in the position of stars caused by the Sun's gravity. For the Sun this deflection angle is small ($\hat{\alpha} \approx 1.4''$), due to the 'weak' curvature in spacetime due to the sun. However, in stronger gravitational fields like that surrounding black holes this effect is exaggerated, or on larger scales that of galaxies and galaxy clusters due to the negligible proper motions of these objects on the sky, the lensing effect is not transient like that of the sun on timescales typically observable to us.

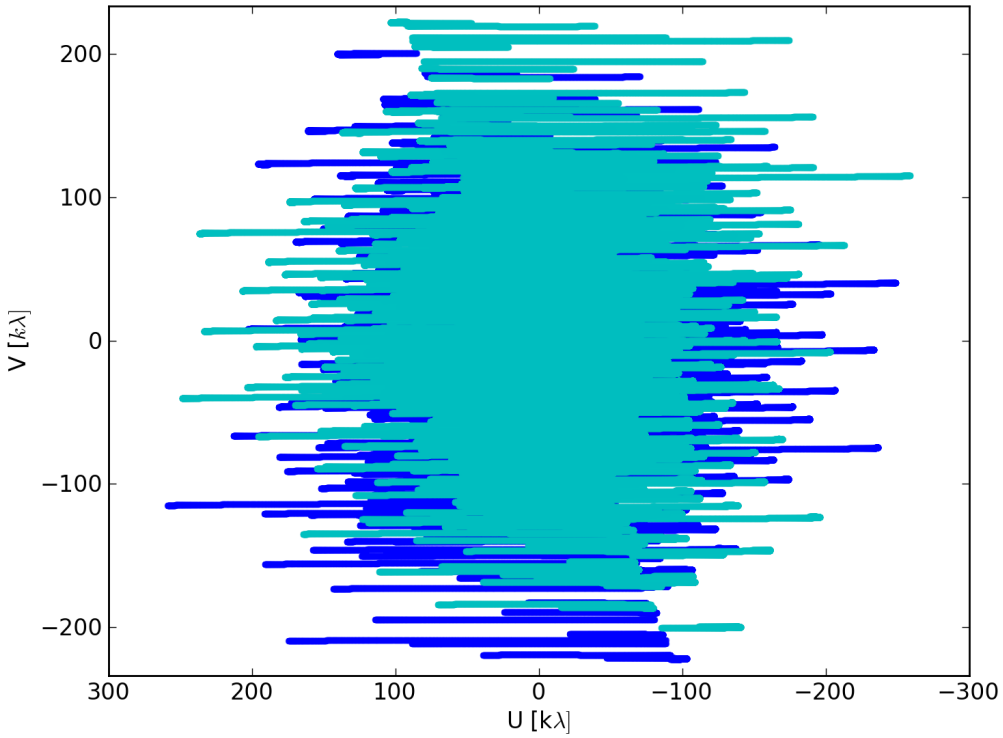

FIGURE 1.8: *uv* plane long exposure
uv plane of a simulated ALMA observation, with an integration time of $\sim$ 5hrs. With increased integration times, due to the earths rotation, much of the previously empty *uv* plane has been populated[3].

1.4.0.1 Simple Lens model

Whilst a full description of gravitational lens modelling is complicated and a thesis length description in of itself, it is beyond the scope of this thesis, and as such I will provide a simplified description here.

As the distances D_{LS} and D_L are typically much greater than the size of the lensing object in galaxy-galaxy lensing, to simplify things I will assume the thin lens approximation. The lens works to change the incoming angle of the light compared to the case where there is no lens, with the angle β between the source and the lens, into a new image with an angle denoted by θ and the reduced lensing angle $\alpha = \theta - \beta$, assuming small angle deflections it can be seen in Figure 1.9 that the actual deflection angle $\hat{\alpha}$ is given by:

$$\alpha = \frac{D_{LS}}{D_S}\hat{\alpha} \tag{1.33}$$

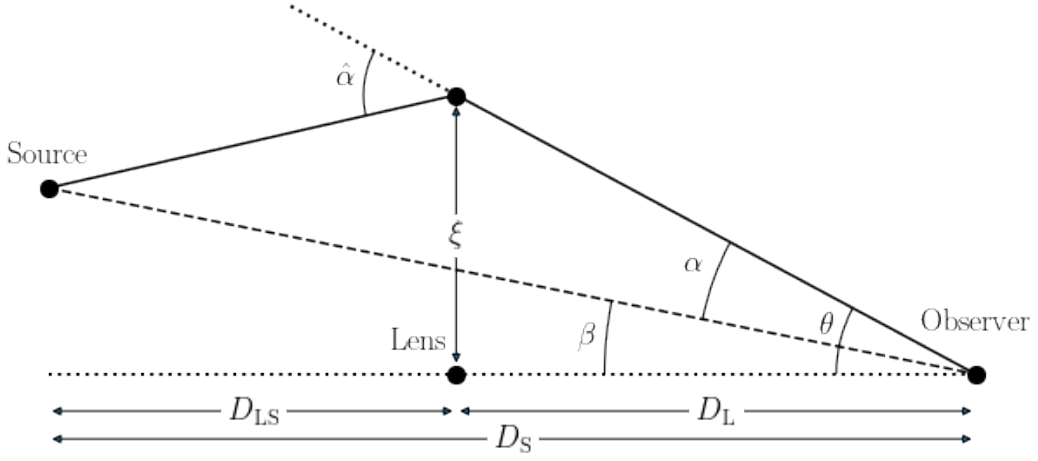

FIGURE 1.9: Gravitational lensing schematic
Gravitational lensing Schematic, credit: Jo Bovey Galaxies book. There are multiple variables in this figure so beginning with the various angles, β is the angle between the source and the lens, α is the angle between the source and the lensed image, θ denotes the angle between the lens and the lensed image (hence $\theta = \alpha + \beta$), and the final angle $\hat{\alpha}$ is the actual deflection angle which is the angle the light has been deflected by the lens. The other variables are for distances with D_{LS}, D_L, and D_S being the distances between the Lens and the source, observer to the lens, and the observer to the source respectively. ξ is the distance between the the light from the source and the lens at its closest approach.

which together with the reduced lensing angle formula gives us the lens equation

$$\beta = \theta - \frac{D_{LS}}{D_S}\hat{\alpha} \tag{1.34}$$

for a point mass, $\hat{\alpha}$ can be expressed as

$$\hat{\alpha} = \frac{4GM}{D_L\theta} \tag{1.35}$$

giving us a new expression for the lens equation

$$\beta = \theta - \frac{4GMD_{LS}}{D_S D_L \theta} \tag{1.36}$$

Setting $\beta = 0$ where the source, observer, and lens are colinear we can we can see that by rearranging equation 1.36 the deflection angle would produce an Einstein ring surrounding the lens, with the angular separation given by the following expression

$$\theta_E = \sqrt{\frac{4GMD_{LS}}{D_S D_L}} \tag{1.37}$$

where θ_E is known as the Einstein angle.

A more appropriate form of this equation, for a galaxy-galaxy lens would be

$$\theta_E = 0.9'' \left(\frac{M}{10^{11} M_\odot}\right)^{0.5} \left(\frac{D}{Gpc}\right)^{-0.5} \tag{1.38}$$

Where $D = \frac{D_S D_L}{D_{LS}}$. With θ_E now calculated, we can be a more general, and include situations in which $\beta \neq 0$. Rewriting equation 1.36 in terms of the Einstein angle, gives us

$$\beta = \theta - \frac{\theta_E^2}{\theta} \tag{1.39}$$

which multiplying through by θ it can be seen that this is a simple quadratic equation with two solutions given by

$$\theta_\pm - \frac{1}{2}\left(\beta \pm \sqrt{\beta^2 + 4\theta_E^2}\right) \tag{1.40}$$

These two solutions indicate that for a point source lens, the lensed source is imaged twice, producing an Einstein ring inside of the Einstein angle (θ_-) and one on the outside (θ_+). As beta increases in equation 1.40 we can see the two images diverge, with one image approaching the lens and the other approaches the true position of the source.

Now we have seen how the Einstein ring changes depending on the relative positions of the source and lens, I will now turn attention to the expected magnification of the lens. Liouville's theorem, which tells us that the surface brightness of the source will be conserved under lensing, shows us that the magnification can be simply calculated by the ratio of the image size to the source size $\mu = \frac{\text{ImageArea}}{\text{SourceArea}}$, and from the lens equation the magnification is given by the following relation

$$\mu = \left| det\left(\frac{\partial \beta}{\partial \theta}\right)\right|^{-1} \tag{1.41}$$

simplifying in the spherically symmetric case to

$$\mu = \frac{\theta}{\beta}\frac{d\theta}{d\beta} \tag{1.42}$$

As we already have the equation for θ with respect to β, we can put in the results to obtain a formula for the magnification, remembering that the two images at θ_+andθ_- add to the magnification such that $\mu = |\mu_+| + |\mu_-|$ where $\mu_{+/-}$ are the values from the corresponding $\theta_{+/-}$.

Therefore we arrive at the magnification for our source

$$\mu = |\mu_+| + |\mu_-| = \left|1 - \left(\frac{\theta_E}{\theta_+}\right)^4\right|^{-1} + \left|1 - \left(\frac{\theta_E}{\theta_-}\right)^4\right|^{-1} \tag{1.43}$$

Using equation 1.40 and substituting $u = \beta/\theta_E$ equation 1.42 can be simplified into the form

$$\mu = \frac{u^2+2}{u\sqrt{u^2+4}} \tag{1.44}$$

As an example, for 9io9, the source of interest to this thesis and discussed in section 1.5, we can obtain a crude value for the magnification using the best fit parameters from the lensing analysis presented in Geach et al. (2015). The best fit parameters for the main lens, give us $\beta = \sqrt{(0.126'')^2 + (-0.094'')^2} = 0.157''$ and $\theta_E = 2.48''$ (Setting the critical radius equal to the Einstein radius, which is true in the Spherically symmetric case (Asada, 1997)) we obtain a magnification factor $\mu \approx 16$, this is in reasonable agreement with the more sophisticated lens modelling which results in $\mu = 14.7 \pm 0.3$ (Geach et al., 2018).

1.5 9io9: a strongly lensed SMG

9io9[4] is a intrinsically hyperluminous SMG lying at $z = 2.55$. First discovered via the citizen science project SpaceWarps (Geach et al., 2015; Marshall et al., 2016; More et al., 2016). The aim of SpaceWarps was to discover new lensing systems in thousands of iJK_s composite images covering the Sloan Digital Sky Survey Stripe 82 field. 9io9 was quickly flagged as a potential lens, the cutout shown to the volunteers can be seen in Fig 1.10, with the red ring clearly visible.

[4]Also referred to as the Red Radio Ring (RRR) in the literature

After its discovery a swathe of observations were taken of 9io9 most notably in the Radio and Sub-mm wavelengths, finding from a modified black-body fit covering a range of sub-mm wavelengths (including the peak of the sub-mm SED with Herschel) that 9io9 is a Hyper-Luminous Infrared Galaxy (HyLIRG, $L_{IR} > 10^{13} L_{\odot}$), inferring a star formation rate of $\approx 2000 M_{\odot} yr^{-1}$ assuming a Chabrier IMF (Geach et al., 2015; Harrington et al., 2019). Alongside its intrinsic brightness, due to it lensed nature it has been magnified with a flux weighted magnification $\mu = 14.7 \pm 0.3$ (Geach et al., 2018). This magnification means its Sub-mm SED peaks at $\approx$ 1Jy making it one of the brightest high-z sub-mm sources and thus an attractive source for follow-up studies. Radio observations also taken at this time, found that 9io9 also emits prolifically in the radio wavebands with a infrared to radio luminosity ratio exceeding that expected from Star-formation alone, hinting at the presence of an AGN at its centre. Equation 1.45 is a simple diagnostic for the presence of AGN, with starforming galaxies being found to have a tight relationship with $\langle q \rangle \approx 2.5$ with a 0.25 dex scatter (Ivison et al., 2010). 9io9 was found to have $q = 1.8 \pm 0.1$ placing it far above this relation and hence potentially hosting an AGN.

Alma follow-up observations presented in Geach et al. (2018) targeting the CO(4-3) and Ci(1-0) transitions tracing the dense star-forming molecular gas and total molecular gas reservoir respectively, found that much of the molecular gas has been driven to high density, fuelling the star formation within. Alongside these lines the blended CN(4-3) and HNC(5-4) transitions were serendipitously detected, after deblending, Geach et al. (2018) found an excess in the red end, potential evidence of interaction between the dense molecular disk and the growing supermassive black hole at its centre producing an outflow.

$$q = \log_{10} \left(\frac{L_{\mathrm{IR}} / 3.75 \times 10^{12}\,\mathrm{W\,m^{-2}}}{L_{1.4\,\mathrm{GHz}} / \mathrm{W\,m^{-2}\,Hz^{-1}}} \right) \tag{1.45}$$

due to its extreme sub-mm flux density 9io9 was also detected and flagged as a potential lensed source in multiple other surveys independently of SpaceWarps, from a combination of the Planck Catalog of compact sources(Harrington et al., 2016), the Herschel-Stripe 82 survey (Viero et al., 2014), and the Atacama Cosmology Telescope (Su et al., 2017).

Since its discovery, 9io9, also referred to as the Red Radio Ring (RRR) in the literature, has become one of the most studied lensed sub-mm galaxies.

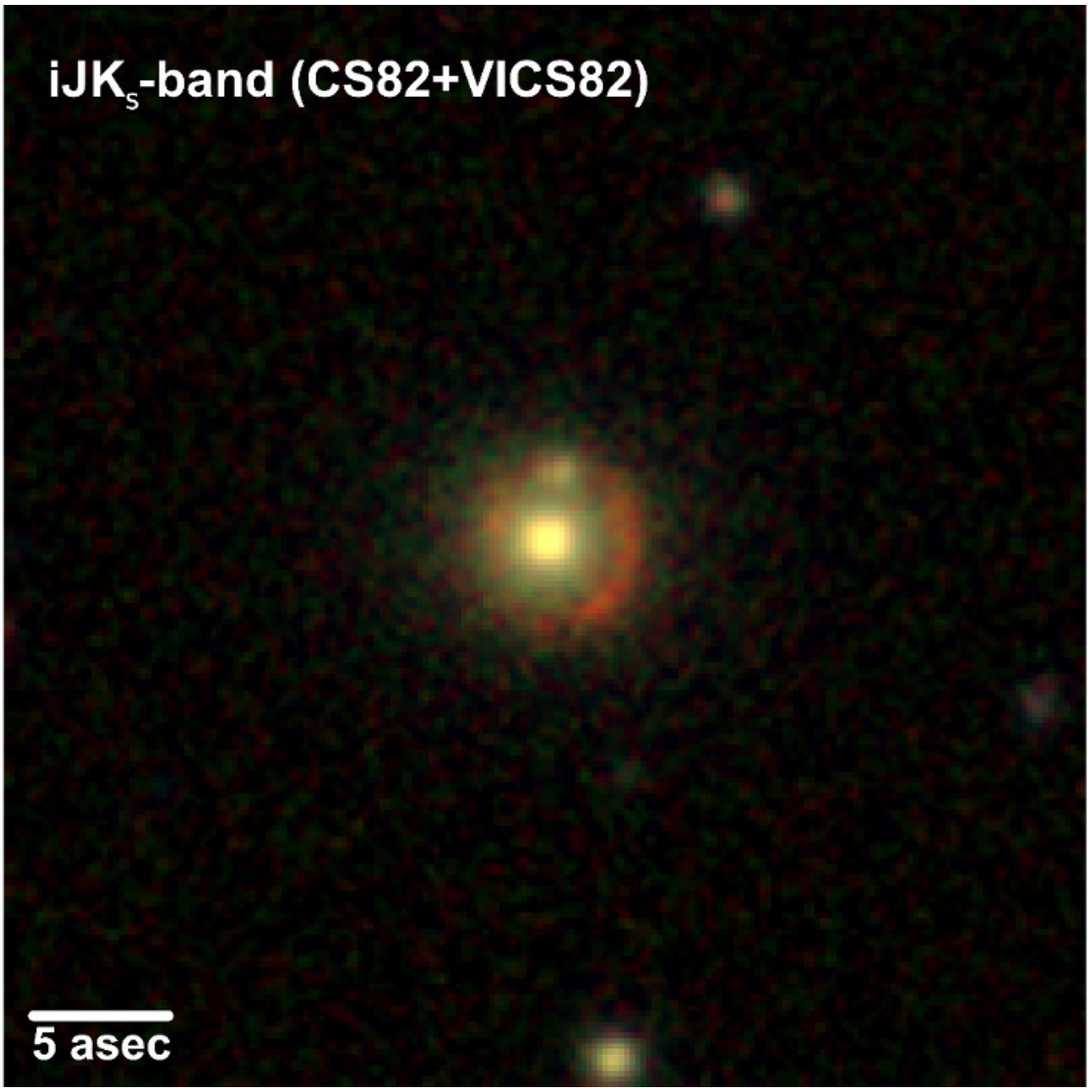

FIGURE 1.10: Colour composite image of 9io9
The composite image of 9io9 that was shown to online volunteers to SPACE WARPS. Volunteers were shown a sequence of 40 arcsec cut-out images where the blue channel represents i-band data from the CHFT Stripe 82 (CS82) survey and the green and red channels are J- and Ks-band from the VISTA-CFHT Stripe 82 (VICS82) survey. the images were centred on luminous red galaxies (LRGs), groups and clusters, and quasars. In the case of 9io9, a red ring of radius ≈ 3 arcsec can be seen around the central galaxy (an LRG at z = 0.2).This lens was identified by numerous volunteers as a pontential lens and quickly became a high confidence canditate lens.

1.6 This Thesis

Having outlined the current picture of cosmology and galaxy evolution, in particular that of dusty infrared bright sources, we move our focus to the aims of this thesis. This thesis aims to investigate the conditions within the ISM of sub-mm galaxies, in particular the aforementioned lensed source 9io9. Our aims are as follows

- Better understand the ionised component of the ISM, are the conditions like that of the Milky Way, a scaled up molecular cloud, or completely different?
- What is driving and sustaining the star formation in 9io9?
- What is the IMF like in these extreme starbursts, do we need to apply a non-canonical IMF in these systems and how does this affect our derived properties.

In chapter 2 we provide observations of ionised gas in 9io9 via the sub-mm [N_{II}] forbidden lines. This work probes the density of the ionised ISM, by utilising both the 122μm and 205μm lines in combination to work as a densiometer of the ionised ISM, to determine whether like the molecular ISM much of this important component of the ISM has been driven to high density.

In chapter 3 we present observations of the ground state rotational transition of Ammonia. This relatively unexplored tracer probes some of the densest gas ($> 10^6 \mathrm{cm}^{-3}$) within the ISM, by comparing the resultant NH_3 / LIR ratio with that of local star forming regions we probe the NH_3 - LIR relation.

In chapter 4 we investigate the IMF within 9io9, using rotational transitions of the CO isotopologues (^{13}CO and C^{18}O). The isotopologue ratio has been found to vary by approximately an order of magnitude between starburst galaxies (ULIRGs and SMGs) and that of local spirals, with this ratio argued to be sensitive to the shape of the high mass slope of the IMF. By incorporating state of the art chemical evolution simulations, and varying the IMF and SFH of a simulated galaxy using stellar yields both with and without the inclusion of stellar rotation we further investigate the conditions under which a variation in the IMF could be warranted.

In Chapter 5 we present a discussion of future work which can build on the work presented here and help further our understanding of the conditions and improving our understanding of 9io9, as well as that of dusty star forming galaxies in general.

Chapter 2

[N II] fine-structure emission at 122 and 205 μm in a galaxy at z=2.6: a globally dense star-forming interstellar medium

Abstract

We present new observations with the Atacama Large Millimeter/sub-millimeter Array of the 122- and 205-μm fine-structure line emission of singly-ionised nitrogen in a strongly lensed starburst galaxy at $z = 2.6$. The 122-/205-μm [N II] line ratio is sensitive to electron density, $n_{\rm e}$, in the ionised interstellar medium, and we use this to measure $n_{\rm e} \approx 300\,{\rm cm}^{-3}$ averaged across the galaxy. This is over an order of magnitude higher than the Milky Way average, but comparable to localised Galactic star-forming regions. Combined with observations of the atomic carbon (C I(1–0)) and carbon monoxide (CO $J = 4$–3) in the same system, we reveal the conditions in this intensely star-forming system. The majority of the molecular interstellar medium has been driven to high density, and the resultant conflagration of star formation produces a correspondingly dense ionised phase, presumably co-located with myriad H II regions that litter the gas-rich disk.

2.1 Introduction

With the discovery of a population of high-redshift submillimeter-selected galaxies (SMGs) over two decades ago (Smail et al., 1997; Barger et al., 1998; Hughes et al., 1998), it became clear that some galaxies undergo episodes of intense star formation in the early Universe, with rates $1000\times$ that of the Milky Way. Thought to be the progenitors of the most massive galaxies in the Universe today (Simpson et al., 2014; Toft et al., 2014), undergoing a period of rapid assembly, a central question has been how such extreme levels of star formation are driven in these galaxies?

With the advent of sensitive, resolved submillimeter and millimeter imaging and spectroscopy of the SMG population at high redshift (see Hodge and da Cunha, 2020, for a recent review), a broad picture is emerging: molecular gas reservoirs are extended on scales of several kiloparsecs (Menéndez-Delmestre et al., 2009; Ivison et al., 2011; Riechers et al., 2011) with a large fraction of the molecular interstellar medium (ISM) driven to high density, driving high instantaneous star-formation rates (SFRs) due to the increased fraction of the ISM participating in star formation at any one time (Gao and Solomon, 2004; Oteo et al., 2017).

But what is the nature of star formation in these extreme systems? Is it essentially identical to what we observe in discrete pockets in the disk of the Milky Way, but occurring more prevalently throughout the ISM? Or is the phenomenon of star formation in these extreme, early systems fundamentally different — perhaps due to systematic differences in metallicity, stellar initial mass function, pressure, magnetic fields, and so-on? Ideally, one would like to understand the internal conditions in more detail: the density and phase structure, chemistry and physical distribution of the gas in high-redshift SMGs, where we use the label 'SMG' to broadly capture extreme star-forming galaxies.

Most progress to date has been in the exploitation of strongly gravitationally lensed systems (e.g. Koopmans et al., 2006; Swinbank et al., 2010; Conley et al., 2011; Wardlow et al., 2013; Dye et al., 2015; Dessauges-Zavadsky et al., 2019; Rybak et al., 2020). For example, SMM J2135−0102 ($z = 2.3$), the so-called 'Cosmic Eyelash' (Swinbank et al., 2010) is one of the most comprehensively studied SMGs to date, and has provided valuable insights into the conditions of the ISM in a galaxy with an SFR roughly $100\times$ that of the Milky Way, close to the peak epoch of galaxy growth (e.g. Ivison et al., 2010; Thomson et al., 2012; George et al., 2014).

Danielson et al. (2011, 2013) showed that the cold molecular gas associated with star formation in the Cosmic Eyelash is exposed to UV radiation fields up to three orders of magnitude more

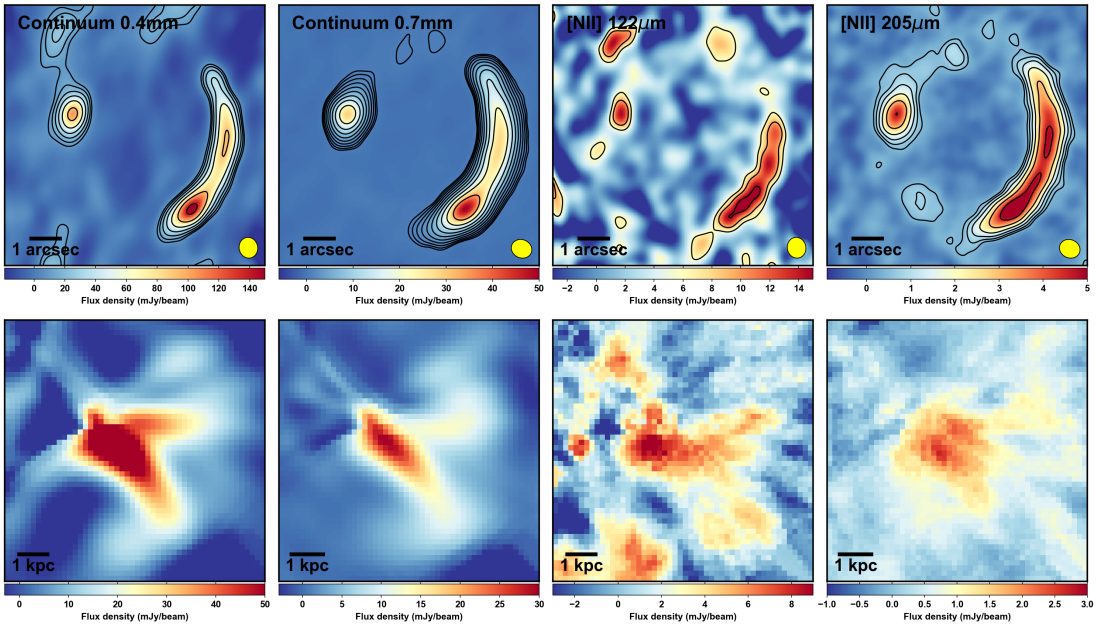

FIGURE 2.1: ALMA bands 8 and 9 observations of 9io9 and [N II] emission maps
ALMA observations of 9io9. Top panels show the continuum at 0.4 and 0.7 mm and the continuum-subtracted [N II] 122- and 205-μm line emission, respectively, in the image plane, lower panels show the corresponding emission in the source plane. Contours in the image plane images are at logarithmically spaced (0.2 dex) intervals of σ, starting at 3σ.

intense than that of the Solar neighbourhood, with the star-forming molecular gas having a characteristic density of $10^4\,\mathrm{cm}^{-3}$, similar to values seen in local ultraluminous infrared galaxies (Davies et al., 2003). Recent work on another well studied lensed system, SDP 81 (Rybak et al., 2020), also suggests that a large fraction of the molecular ISM has been driven to high density, with star-formation occurring throughout the galaxy, but localised in dense star-forming complexes of size $\sim$200 pc with conditions comparable to the Orion Trapezium cluster in the Milky Way (see also Swinbank et al., 2015). We note, however, that the interpretation of 'clumps' detected in high resolution interferometric imaging needs to be treated with caution, with Ivison et al. (2020) demonstrating that previously reported star-forming clumps in the Cosmic Eyelash are in fact spurious artifacts, a result of over-cleaning of relatively low signal-to-noise data.

Targets like the Cosmic Eyelash and SDP 81 are valuable because their lens-amplified flux offers a route to measure diagnostic tracers of the ISM and its conditions in a way that would be impossible in the unlensed case. These targets are, however, intrinsically rare. Here we focus on another strongly lensed SMG: '9io9' (Geach et al., 2015). 9io9 is a galaxy discovered as part of the citizen science project *Spacewarps* (see Marshall et al., 2016; More et al., 2016) and independently as a bright millimetre source by *Planck* (Harrington et al., 2016), *Herschel* (Viero et al., 2014), and the Atacama Cosmology Telescope (Su et al., 2017). 9io9 lies at $z = 2.6$, close

to the peak epoch of galaxy growth (Geach et al., 2018). Even after taking into account the 15× magnification factor, 9io9 appears to have a total infrared luminosity, $L_{\rm IR}$, exceeding $10^{13}\,{\rm L}_{\odot}$, putting in the hyperluminous class, with an inferred SFR of around $2000\,{\rm M}_{\odot}{\rm yr}^{-1}$, *modulo* the sometimes high and often hidden AGN contribution to $L_{\rm IR}$ in such systems (e.g. Ivison et al., 2019), and also *modulo* evidence suggesting that the stellar initial mass function in high-density star-forming regions is markedly top heavy (e.g. Romano et al., 2017; Zhang et al., 2018b; Motte et al., 2018; Schneider et al., 2018; Brown and Wilson, 2019, cf. Romano et al. 2019). It is therefore an excellent laboratory for studying the conditions of intense star formation in the early Universe.

In this paper we present new observations of 9io9 with the Atacama Large Millimeter/submillimeter Array (ALMA), building on the work of Geach et al. (2018). This study focuses on the [N II] 122- and 205-μm fine-structure lines. These lines trace the cool, ionised ISM (Goldsmith et al., 2015), and together can be used to constrain the electron density (e.g. Zhang et al., 2018a, and references therein). With previous ALMA CO $J(4\rightarrow3)$ and C I (1–0) observations (Geach et al., 2018) this allows us to link the properties of the dense molecular and the ionised phases of the ISM on identical scales in 9io9. In Section 2 we describe the observations and data reduction, in Section 3 we present our analysis, in Section 4 we interpret and discuss the main results of the analysis and present our conclusions in Section 5. Throughout we assume a 'Planck 2015' cosmology where $H_0 = 68$ km s^{-1} Mpc^{-1} and $\Omega_{\rm m} = 0.31$ (Planck Collaboration et al., 2016).

2.2 Observations

9io9 ($02^{\rm h}09^{\rm m}413$, $00^{\circ}15'58''5$, $z = 2.5543$) was observed with the ALMA 12-m array in project 2017.1.00814.S in Bands 4, 8 and 9. The details of the Band 4 observations are presented in Geach et al. (2018), and here we present the new Band 8 and 9 data. The Band 8 observations were conducted on 2018 August 26 and 2018 September 07 in two 40-min execution blocks with a representative frequency of approximately 411.5 GHz. The antenna configuration was C43–4 (with 47 antennas), with a maximum baseline of 783 m. The central frequencies of the four spectral windows were 397.466, 399.404, 409.481 and 411.481 GHz, designed to cover the the redshifted [N II] $^3P_1\rightarrow{}^3P_0$ fine-structure line ($\nu_{\rm rest} = 1461.131$ GHz) and continuum emission. Calibrators included J0217+0144, J0423−0120 and J2253+1608. In two executions the total

on-source integration time was 42 min, with an average precipitable water vapor column of 0.73 mm, resulting in an r.m.s. noise of 3 mJy beam^{-1} in a 15.6-MHz channel.

The Band 9 observations were conducted on 2018 August 19 in a single 70-min execution block. The antenna configuration was C43–3 (with 46 antennas), with a maximum baseline of 484 m. The representative frequency was approximately 692.3 GHz with eight spectral windows at 670.311, 672.249, 674.249, 676.202, 686.248, 688.201, 690.200 and 692.138 GHz. The Band 9 observations were designed to contain the redshifted [N II] $^3P_2 \rightarrow ^3P_1$ fine-structure line ($\nu_{\rm rest} = 2459.380$ GHz) and continuum emission. Calibrators included J0217+0144 and J0522−3627. The total time on-source was 31 min, with an average precipitable water vapor column of 0.45 mm, resulting in an r.m.s. noise of 10 mJy beam^{-1} in a 15.6-MHz channel.

For the Band 8 data we used the pipeline-restored calibrated measurement set. For the Band 9 observations, due to unstable phases in two antennas (DA64 and DA24) we re-calibrated manually, flagging both dishes within the pipeline script. We imaged and cleaned the data using the CASA (v.5.1.0-74.el7) task, `tclean`. As in Geach et al. (2018), we employ multi-scale cleaning (at scales of $0'', 0.5'',$and$, 1.25''$). First we produce dirty cubes to establish the r.m.s. (1σ) noise per channel, and then clean down to a threshold of 3σ. With natural weighting, the synthesised beams were $0.43'' \times 0.35''$ (FWHM, position angle 33°) and $0.32'' \times 0.28''$ (position angle 74°) in Bands 8 and 9, respectively. In order to produce data cubes that have closely matched resolution across Band 4, 8 and 9, we also produce *uv*-tapered maps with a scale of $0.6''$ noting that the *uv* plane is well sampled across all bands such that we expect negligible losses to extended emission on the scale of the lens (LAS $\lesssim$3–4$''$). In Fig. 2.1 we present the image-plane maps of the line-free Band 8 (400 GHz) and Band 9 (680 GHz) continuum emission and the line-averaged [N II] $^3P_1 \rightarrow ^3P_0$ and $^3P_2 \rightarrow ^3P_1$ continuum-subtracted emission.

2.3 Analysis

2.3.1 Lens model

We adopt the same lens model as Geach et al. (2018). Briefly, the lens model includes the gravitational potential of both the primary lensing galaxy ($z \approx 0.2$) and its smaller northern companion (assumed to be at the same redshift). The model uses the semi-linear inversion method of Warren and Dye (2003) to reconstruct the source plane surface brightness that best

matches the observed Einstein ring for a given lens model. This process is iterated, varying the lens model and creating a source reconstruction at each iteration, until the global best fit lens model is found (Geach et al., 2018). The best fit model was used to produce source-plane cubes. Each slice was reconstructed with 50 realisations of a randomised Voronoi source plane grid (see Dye et al., 2018, for further details) and the mean taken, weighted by the log of the likelihood of each realisation. In Fig. 2.1 we show the equivalent continuum and line maps in the source plane. The resulting source plane reconstruction has an average beam size of 280 mas (FWHM) corresponding to a physical scale of 2.3 kpc in the source plane. Fig. 2.1 shows the source-plane images of the line-free Band 8 (400 GHz) and Band 9 (680 GHz) continuum emission and the line-averaged [N II] $^3P_1 \rightarrow ^3P_0$ and $^3P_2 \rightarrow ^3P_1$ continuum-subtracted emission. As can be seen in Figure 2.1, the [N II] 122μm line measured in Band 9 appears to have an additional clump of emission to the NE not clearly visible (however detected) in the 205μm map. This feature is multiply imaged in the image plane and also detected in the Band 8 data, so although at low significance (3σ)) unlikely to be spurious. However due to a lack of a continuum detection and the low significance of the detection, the strength of the 122μm line in this region is unreliable. There are several other low significance features that do correlate with emission in other bands along the ring, but due to the relatively low signal-to-noise of the 122μm line we do not attempt to interpret the resolved properties of the line itself, or the line ratio, concentrating our analysis on the integrated properties. Of course, with the 122μm line strength now constrained, future observations could be obtained to address the resolved properties at higher signal-to-noise. Fig. 2.2 shows the [N II] doublet as well as the C I (1–0) and CO $J(4\rightarrow3)$ lines, scaled for comparison. In the following, all analysis is performed in the source plane. The errors quoted for the intrinsic source properties do not include any systematic uncertainty introduced by the prescribed parametric lens model (see e.g. Schneider and Sluse, 2013).

2.3.2 Line and continuum measurements

As we have resolved the global thermal dust continuum emission from 9io9 at high signal-to-noise in each of ALMA Bands 4, 8 and 9, with Band 9 probing close to the redshifted peak of the thermal emission, we can estimate $L_{\rm IR}$ (rest-frame 8–1000 μm) for the source, fully taking into account the effects of differential lensing since $L_{\rm IR}$ can be determined in the source plane. We fit the observed emission with a single-temperature modified blackbody spectrum, allowing the dust emissivity (β), dust temperature ($T_{\rm d}$) and normalisation to be free parameters. Summing the luminosity within the region bound by the $\geq$3σ contour (in Band 8) we measure a total

$L_{\rm IR} = (1.1 \pm 0.2) \times 10^{13}\,{\rm L}_\odot$. Thus, 9io9 is a hyperluminous infrared-luminous galaxy (HyLIRG) at $z \approx 2.6$. For reference, the total Band 8 and Band 9 source plane continuum flux densities are 12 mJy and 43 mJy at observed frequencies of 400 and 680 GHz, respectively.

We evaluate line luminosities using the standard relation Solomon et al. (1997)

$$\frac{L}{{\rm L}_\odot} = \left(\frac{1.04 \times 10^{-3} \nu_{\rm obs}}{\rm GHz}\right) \left(\frac{D_{\rm L}}{\rm Mpc}\right)^2 \left(\frac{S\Delta V}{\rm Jy\ km\ s^{-1}}\right) \tag{2.1}$$

where $D_{\rm L}$ is the luminosity distance, $\nu_{\rm obs}$ is the observed frequency and $S\Delta V$ is the velocity-integrated line flux. Subtracting the continuum model from each pixel based on a linear fit to line free regions of the lines corresponding data cube allowing the gradient and normalisation vary as free parameters, the integrated flux density measured within the same 3σ region as the continuum (which was defined as the 3σ region in the Band 8 datacube) of the [N II] 205-μm line is $\mathbf{S}\Delta V = (2.37 \pm 0.06)$ Jy km s^{-1}, corresponding to $L_{205} = (4.7 \pm 0.1) \times 10^8\,{\rm L}_\odot$. For the [N II] 122-$\mu$m line, the integrated flux density is $\mathrm{S}\Delta V = (7.6 \pm 0.9)$ Jy km s^{-1}, corresponding to $L_{122} = (2.6 \pm 0.3) \times 10^9\,{\rm L}_\odot$, integrating between -500 km s^{-1} and 300 km s^{-1} due to the [N II] lines being incomplete. By comparing to the CO $J(4\rightarrow3)$ and C I (1–0) lines we estimate we are missing $\approx 10\%$ of the total line flux for both lines, however this should not alter the resultant [N II] ratio as both lines are equally affected. Uncertainties are determined by adding Gaussian noise to each channel, with a scale determined from off-source regions of the datacube, taking the standard deviation of the pixel-to-pixel channel noise and scaling by the solid angle subtended by the 3σ mask used to define the total emission. Repeating this 1000 times and integrating the lines for each realisation allows us to estimate the uncertainties.

2.3.3 Electron density

With an ionisation potential of 14.5 eV, N^+ originates exclusively from the ionised ISM. N^+ thus traces H II regions and is a good tracer of massive star formation, with its emission being directly related to the ionising photon rate and thus the number of massive stars (Zhao et al., 2016b; Herrera-Camus et al., 2016). At lower densities ($0.01 \leq n_{\rm e} \leq 0.1$ cm^{-3}), N^+ is also a coolant of the warm ionised medium (WIM).

N^+ has three fine-structure levels: $^3P_{0,1,2}$. These are simply referred to as 0, 1, 2 in the following. If electron collisions are the primary excitation mechanism, we can write the collision rates as

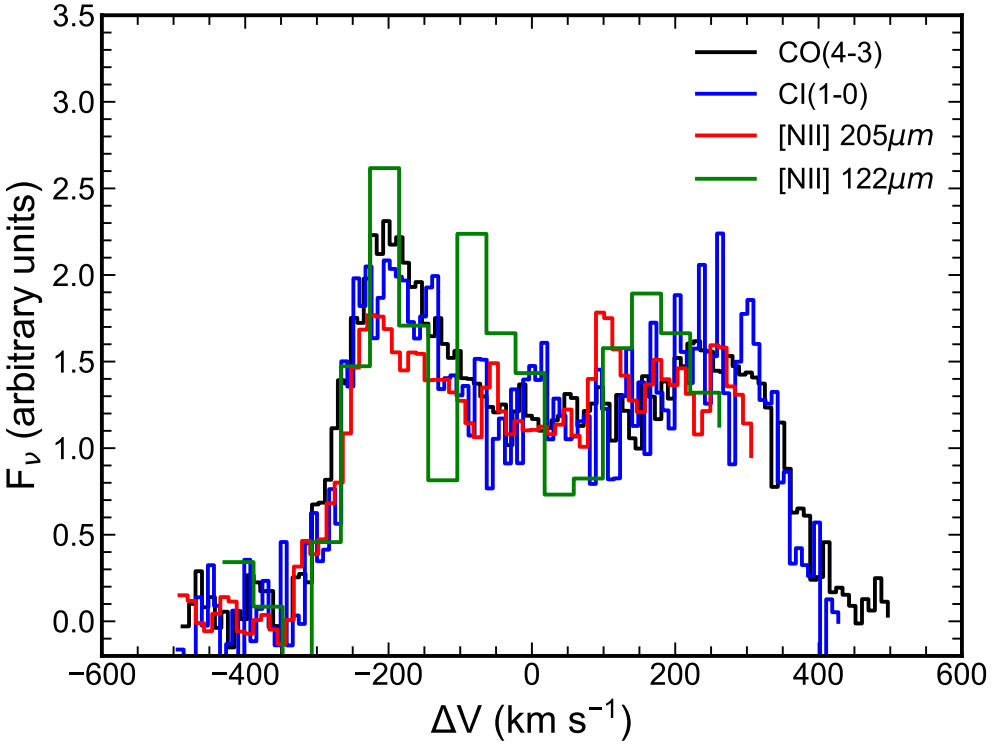

FIGURE 2.2: Source plane line profiles of [N II] doublet, C I (1–0) and CO $J(4\rightarrow3)$ [N II] doublet, C I (1–0) and CO $J(4\rightarrow3)$, scaled such that each line has a common mean (on an arbitrary scale). All lines share a very similar double horned profile, indicating that the molecular and ionized phases are broadly tracing the same structures.

$C_{ij} = R_{ij} n_e$ where R_{ij} is the collision rate coefficient and n_e is the electron density. Following Goldsmith et al. (2015), the rate equations can be written

$$\begin{aligned} -(A_{21}+C_{21}+C_{20})n_2 + C_{12}n_1 + C_{02}n_0 &= 0 \\ (A_{21}+C_{21})n_2 - (A_{10}+C_{10}+C_{12})n_1 + C_{01}n_0 &= 0 \\ C_{20}n_2 + (A_{10}+C_{10})n_1 - (C_{02}+C_{01})n_0 &= 0 \end{aligned} \tag{2.2}$$

where n_0, n_1, and n_2 are the populations of each level, such that $n_0+n_1+n_2 = n(\mathrm{N}^+)$, and A_{ij} are the Einstein coefficients. The 122- and 205-μm emission lines correspond to energy transitions E_{21} and E_{10}, respectively. For optically thin emission these are related to the line intensity of the i $\rightarrow$ j transition as

$$I_{ij} = \frac{A_{ij} E_{ij} N_i}{4\pi}, \tag{2.3}$$

where N_i is the column density of the upper level. The ratio of the line intensities then becomes

$$R = \frac{I_{21}}{I_{10}} = \frac{A_{21}E_{21}n_2}{A_{10}E_{10}n_1}, \tag{2.4}$$

assuming the ratio of column densities equals the ratio of volume densities. The rate equations (2.2) yield

$$\frac{n_2}{n_1} = \frac{C_{12}(C_{01}+C_{02})+C_{02}(A_{10}+C_{10})}{(A_{21}+C_{21}+C_{20})(A_{10}+C_{10})+C_{20}C_{12}}. \tag{2.5}$$

Using $C_{ij} = R_{ij}n_e$, we derive a relation for the electron density which can be written in the form

$$n_e = \frac{d}{c}\frac{R-R_{min}}{R_{max}-R}, \tag{2.6}$$

where

$$\begin{aligned} a &= R_{12}R_{01}+R_{02}R_{10}+R_{02}R_{12} \\ b &= R_{02}A_{10} \\ c &= R_{02}R_{21}+R_{01}R_{21}+R_{01}R_{12} \\ d &= A_{21}(R_{02}+R_{01}) \\ R_{min} &= \frac{A_{21}E_{21}}{A_{10}E_{10}}\frac{b}{d} \\ R_{max} &= \frac{A_{21}E_{21}}{A_{10}E_{10}}\frac{a}{c}. \end{aligned} \tag{2.7}$$

Using collision rates from Tayal (2011) for a kinetic temperature, $T_e = 8000\,\mathrm{K}$, and assuming that collision rates are independent of temperature[1] yields an expression for the electron density based on the line ratios:

$$n_e = 247\left(\frac{R-0.52}{9.73-R}\right)\mathrm{cm}^{-3}. \tag{2.8}$$

Using our measurements of the line intensities, we find an electron density of $n_e = 290^{+90}_{-70}\mathrm{cm}^{-3}$. This elevated electron density could explain the discrepancy found between the [N II] 205μm and L_{IR}-derived SFRs by Harrington et al. (2019), since in that work a low electron density — $n_e \approx 30\ \mathrm{cm}^{-3}$ — was assumed.

[1] Although the relation is not completely temperature independent, the derived electron density does not vary by more than 10% for a 2000 K increase in kinetic temperature, as can be seen in Fig. 2.3.

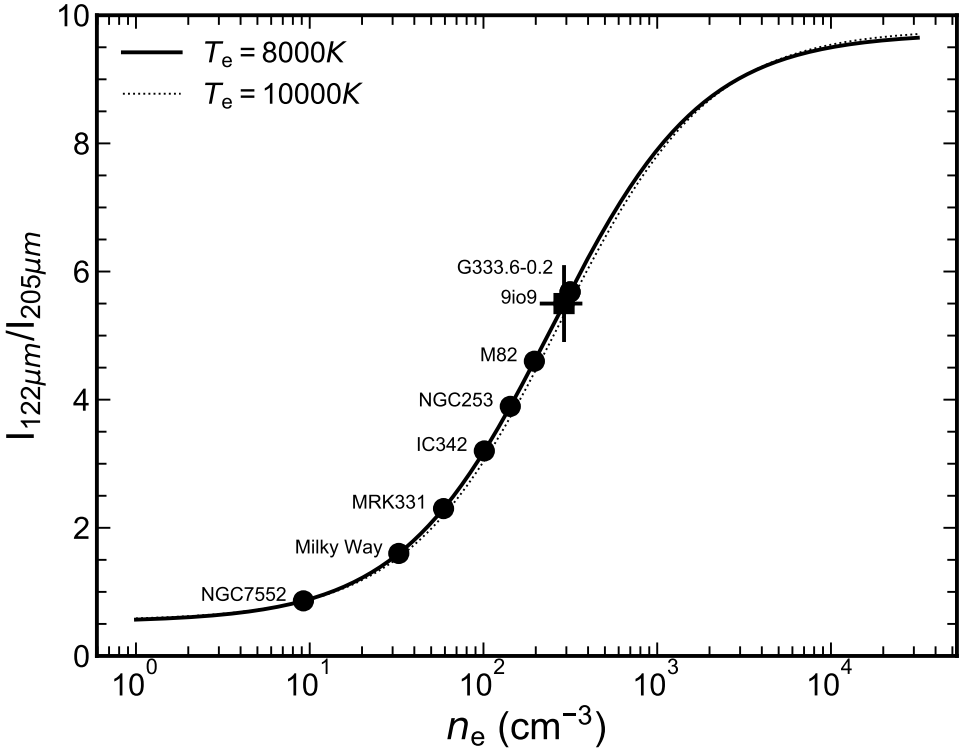

FIGURE 2.3: Derived electron density versus [N II] line ratio
Derived electron density versus [N II] line ratio, including literature values found for a variety of Galactic and extragalactic sources. Note the insensitivity of n_e to the assumed electron temperature.

There may be a potential bias in our measurement if the local radiation field is so intense that optical pumping of [N II] provides a significant contribution to the excitation (Flannery et al., 1979). We can test if this is likely to be important by comparing the pumping collision rate with the inferred collision rate from our data. The pump rate can be expressed as $R_p = 1835 \nu U_\nu$, where νU_ν is a measure of the strength of the radiation field in erg cm^{-3}. In the Solar neighbourhood, $\nu U_\nu \approx 7 \times 10^{-14}$ erg cm^{-3} at $\nu \approx 3 \times 10^{15}$ Hz corresponding to the $^3D_1 \rightarrow ^3P_0$ transition (Draine, 2011). The interstellar UV radiation field in galaxies like 9io9 is not well constrained, however Danielson et al. (2011) found for the Cosmic Eyelash that the cold gas was exposed to a UV radiation field that is roughly 1000× that of the local Galactic ISM. If we assume similar conditions for 9io9, then we obtain a pump rate of $R_p \approx 10^{-7}$ s^{-1}, or approximately 2 per cent of the collision rate. Thus, even with rather extreme local radiation fields — perhaps only relevant for the gas in the immediate vicinity of O and B stars — pumping has a negligible impact on the [N II] excitation.

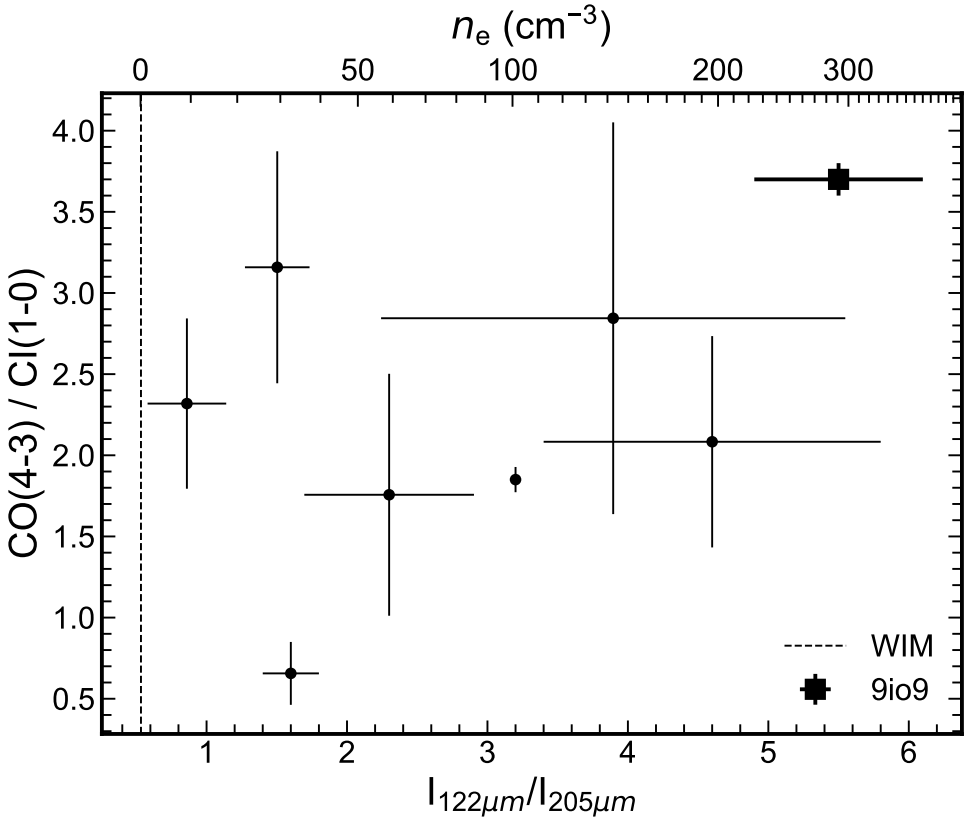

FIGURE 2.4: [N II] line ratio verses CO $J(4\rightarrow3)$/C I (1–0)
[N II] line ratio versus CO $J(4\rightarrow3)$/C I (1–0) (a dense to total molecular gas mass tracer) for a range of sources (Wright et al., 1991; Petuchowski et al., 1994; Zhang et al., 2001; Oberst et al., 2006; Rigopoulou et al., 2013; Rosenberg et al., 2014, 2015; Zhao et al., 2016b).

2.4 Interpretation and discussion

Recent studies of electron densities in the ISM of star-forming galaxies at high redshift using optical/near-infrared (NIR) tracers of n_e — such as O II and S II — have also found values significantly higher than those typically observed in the local Universe, with $n_e \gtrsim 100\,\mathrm{cm}^{-3}$ not uncommon in samples of (Hα-selected) star-forming galaxies with SFR $\sim$ 1–100 s $\mathrm{M}_\odot\,\mathrm{yr}^{-1}$ (Masters et al., 2014; Shirazi et al., 2014). Kaasinen et al. (2017) connected these elevated electron densities to the high SFRs observed in galaxies at $z \sim 1$–2, pointing out that the average electron densities in their high-redshift and local samples are comparable, when controlled for SFR. Shimakawa et al. (2015) and Jiang et al. (2019) note a correlation between the surface density of star formation (Σ_{SFR}) and n_e, providing further evidence of the close relationship between star formation and ionised ISM density. This is not surprising, since if star formation depends on the density distribution of the cold ISM, and Σ_{SFR} is enhanced when a large fraction

of the molecular ISM is driven to high density, then that will likely be reflected in the resultant ionised phase density in the vicinity of those star-forming regions.

The integrated profiles of both [N II] lines resemble the integrated CO $J(4\rightarrow3)$ and C I (1–0) line profiles (recall Fig. 2), indicating that the ionised and molecular tracers originate from the same material and local environments. Geach et al. (2018) modelled the CO $J(4\rightarrow3)$ emission with a rotating disk motivated by the dynamics of circumnuclear gas seen in local ULIRGs (Downes and Solomon, 1998), and this provided an excellent fit to the data, with properties similar to another stongly lensed system, SDP 81 (e.g. Partnership et al., 2015; Swinbank et al., 2015; Dye et al., 2015; Hatsukade et al., 2015; Rybak et al., 2020). It is reasonable to assume that the [N II] emission is tracing the ionised component of the ISM across the same disk, and is broadly co-spatial with the star-forming molecular gas. The measured electron density of $n_{\rm e} = 290^{+90}_{-70}\,{\rm cm}^{-3}$ is significantly higher than that expected for the WIM, which is comprised of material at densities 3–4 orders of magnitude lower (Gaensler et al., 2008; Weisberg et al., 2008).

The electron density in 9io9 is high, but not extreme when we consider individual local star-forming environments. For example, the Galactic H II region, G333.6−0.2, has an electron density, $\approx 300\,{\rm cm}^{-3}$, also determined via the [N II] ratio (Colgan et al., 1993). This is consistent with the conditions in 9io9, with the key difference that we are measuring the characteristic electron density on scales of several kiloparsecs, rather than for an individual star-forming complex. Thus, a possible scenario is that star formation in 9io9 is proceeding in environments that resemble 'normal' star-forming regions like G333.6−0.2 but with the key distinction that, while G333.6−0.2 represents a tiny fraction of the total Milky Way ISM by mass and volume, in 9io9 the *majority* of the ISM may be in this state.

There is support for this 'globally dense' picture in the molecular phase tracers. Papadopoulos and Geach (2012) argue that the CO $J(4\rightarrow3)$/C I (1–0) ratio is an excellent empirical tracer of the ratio of dense, actively star-forming molecular gas to the total molecular reservoir. Geach et al. (2018) show that the observed ratio in 9io9 is consistent with over half of the molecular ISM having been driven to high density. It follows that the H II regions produced by massive star formation should have correspondingly elevated electron densities. Hints of this link can be seen in Fig. 2.4, where we compare the CO $J(4\rightarrow3)$/C I (1–0) ratio to the [N II] line ratio for 9io9 and a sample of sources from the literature spanning a range of densities. Generally, there is a weak trend that galaxies or regions with high electron densities — as traced by the

[N II] line ratio — have a correspondingly high dense molecular gas fraction — as traced by the CO $J(4\rightarrow3)$/C I (1–0) ratio. This trend however is not significant given the current data, applying a Pearsons-r test of significance, puts it at $\approx 1.5\sigma$.

Given 9io9's clear disk-like structure, most evident in the shape of the line profiles and confirmed by the excellent fits achieved for disk- or ring-like kinematic models (Geach et al., 2018), we can consider a detailed picture of star formation in this galaxy. A plausible scenario is that the disk comprises an ensemble of dense clumps containing a large fraction of the total ISM, within which star formation occurs. This is not a novel concept, of course. Early work with *Hubble Space Telescope* suggested that a large fraction of star formation in high-redshift Lyman-break galaxies may occur in large blue clumps, on scales of up to 1 kpc (e.g. Cowie et al., 1995; Elmegreen et al., 2005). More recently, resolved imaging of strongly lensed dusty star-forming systems suggests the presence of distinct regions of embedded high-density star formation on scales of $\sim$100 pc, with luminosity densities comparable to the cores of local giant molecular clouds (e.g. Swinbank et al., 2010, 2015; Hatsukade et al., 2015, though see Ivison et al. 2020). This led to a 'giant clump' model of star formation in the most vigorously star-forming galaxies at high redshift, where the 100 pc-scale clumps thought to be present in objects like the Cosmic Eyelash resemble scaled-up versions of the dense, 1 pc-scale cores within local giant molecular clouds.

The physical argument put forward to explain the formation of such structures is through disk instabilities, which don't preclude but can conveniently circumvent the requirement for mergers or interactions to drive gas to high densities, although interactions are known to be common — perhaps even ubiquitous — amongst SMGs (e.g. Engel et al., 2010). At high gas fractions and surface densities, disks will be Toomre-unstable (Toomre instability occurs when the gravitational force overcomes the thermal pressure and shear forces associated with a differentially rotating disk) and undergo local collapse, fragmenting into multiple star forming regions. (Toomre, 1964; Noguchi, 1999; Dekel et al., 2009b). The gas densities and velocity dispersions typically *inferred* in objects like the Cosmic Eyelash, SDP 81 and 9io9, would give rise to a Jeans length scale on which this fragmentation occurs that is broadly consistent with the $\approx$100 pc clump scales described above (e.g. Swinbank et al., 2015; Hatsukade et al., 2015)[2]. The current source plane resolution in 9io9 is around 300 pc and so we cannot yet address this question; however, the brightness of the target (approaching 1 Jy) makes it a prime candidate for pushing to very

[2]Note that in the case of the Cosmic Eyelash Ivison et al. (2020) have shown these clumps to be spurious — the result of over-cleaning a low-signal-to-noise interferometric image.

long baselines to resolve the disk sub-structure, allowing us to link the physical conditions of the ISM explored here on global scales to the spatial distribution of the gas down to 10s of parsecs.

2.5 Conclusions

We have reported new ALMA Band 8 and 9 observations of a strongly lensed HyLIRG at $z = 2.6$, targeting the [N II] fine-structure line emission and thermal continuum in the rest-frame far-infrared waveband. Our main findings are as follows:

- We report detections of both the 122- and 205-μm [N II] emission lines, which trace the ionised ISM. The [N II] lines match the double-horned line profiles seen in CO $J(4\rightarrow3)$ and C I (1–0), reported by Geach et al. (2018) and well-modelled by a rotating disk. This implies that the ionised gas is broadly co-located with the molecular material on scales of several kiloparsecs.

- We use the 122/205μm line ratio to estimate the average electron density in the ISM, finding $n_{\rm e} \approx 300\,{\rm cm}^{-3}$, an order of magnitude above that of the (average) Milky Way, comparable with measurements of the electron density in discrete Galactic star-forming environments.

- We find a tentative trend ($\approx 1.5\sigma$) between the ratio of dense molecular gas and the total molecular gas reservoir, as traced by CO $J(4\rightarrow3)$ and C I (1–0), and the [N II] line ratio. If the former is a tracer of the dense molecular gas fraction as Papadopoulos and Geach (2012) argue, then the correlation with the [N II] ratio and therefore ionised gas density reveals a picture of 'globally dense' ISM, where a significant fraction of the molecular component has been driven to high density — possibly through violent disk instabilities, with or without galaxy interactions — with myriad individual H II regions dominating the observed [N II] emission.

9io9 is a remarkably extreme system, fortuitously lensed to provide us a glimpse of its inner workings. Our findings support a picture where the nature of star formation in this galaxy might not necessarily differ from the conditions of star formation in our own Milky Way. The key difference is that a far higher fraction of the ISM is currently participating in that star formation.

Chapter 3

Ammonia in the interstellar medium of a starbursting disc at $z = 2.6$

Abstract

We report the detection of the ground state rotational emission of ammonia, ortho-NH_3 ($J_K = 1_0 \rightarrow 0_0$) in a gravitationally lensed, intrinsically hyperluminous, star-bursting galaxy at $z = 2.6$. The integrated line profile is consistent with other molecular and atomic emission lines which have resolved kinematics well-modelled by a 5 kpc-diameter rotating disc. This implies that the gas responsible for NH_3 emission is broadly tracing the global molecular reservoir, but likely distributed in pockets of high density ($n \gtrsim 5 \times 10^4$ cm^{-3}). With a luminosity of $2.8 \times 10^6\, L_\odot$, the NH_3 emission represents 2.5×10^{-7} of the total infrared luminosity of the galaxy, comparable to the ratio observed in the Kleinmann-Low nebula in Orion and consistent with sites of massive star formation in the Milky Way. If L_{NH_3}/L_{IR} serves as a proxy for the 'mode' of star formation, this hints that the nature of star formation in extreme starbursts in the early Universe is similar to that of Galactic star-forming regions, with a large fraction of the cold interstellar medium in this state, plausibly driven by a storm of violent disc instabilities in the gas-dominated disc. This supports the 'full of Orions' picture of star formation in the most extreme galaxies seen close to the peak epoch of stellar mass assembly.

3.1 Introduction

The progenitors of the most massive galaxies today are most likely the population of intense star-bursting galaxies seen at $z \gtrsim 2$ (Smail et al., 1997; Hughes et al., 1998). These starbursts have large gas reservoirs (Bothwell et al., 2013) representing a significant fraction of baryonic mass (Wiklind et al., 2019) fuelling very high rates of star formation, possibly up to three orders of magnitude greater than the Milky Way (Chapman et al., 2004; Barger et al., 2014).

Generally, these gas- and dust-rich systems are obscured in the optical, but radiate strongly in the submillimetre and millimetre through their thermal dust emission. Indeed, the emission from key molecular and atomic tracers of the cool and cold dense interstellar medium (ISM) responsible for fuelling star formation, and its immediate environment is also observed at these wavelengths.

Two key factors have improved our understanding of the nature of these distant, dusty, prodigiously star-forming galaxies over the past decade. One is the identification of large samples of strongly gravitationally lensed systems (e.g. Danielson et al., 2013; Spilker et al., 2014; Rybak et al., 2015; Geach et al., 2015; Rybak et al., 2020). Lensing amplifies flux, revealing emission features otherwise too faint to detect, and magnifies images of galaxies to provide access to spatial scales not achievable by any other means (Rybak et al., 2015; Geach et al., 2018; Rybak et al., 2020). The second is the advent of sensitive, wide bandwidth interferometry across the submillimetre–millimetre using large interferometric arrays, in particular the Atacama Large Millimetre/submillimetre Array (ALMA). The follow-up of lensed galaxies with ALMA has accelerated the establishment of a clearer, albeit still incomplete, picture of the nature of galaxies undergoing intense starbursts in the early Universe.

What astrophysics is responsible for the existence of extreme starbursts at high-z? Compared to the merger-dominated ultra luminous infrared galaxies (ULIRGs) in the local universe with intense circumnuclear star formation, high-z starbursts of equivalent luminosity appear to be sustaining star formation across much larger scales Rujopakarn et al. (2011).

Mergers undoubtedly play a role in the triggering high-z starbursts (Tacconi et al., 2010; Engel et al., 2010), but there is some observational evidence that some of the most intensely star-forming galaxies are simply consistent with large gas-dominated rotationally supported discs (Hodge et al., 2016; Jiménez-Andrade et al., 2018; Geach et al., 2018; Gullberg et al., 2018). In these systems a significant fraction of the ISM appears to have been driven to high density

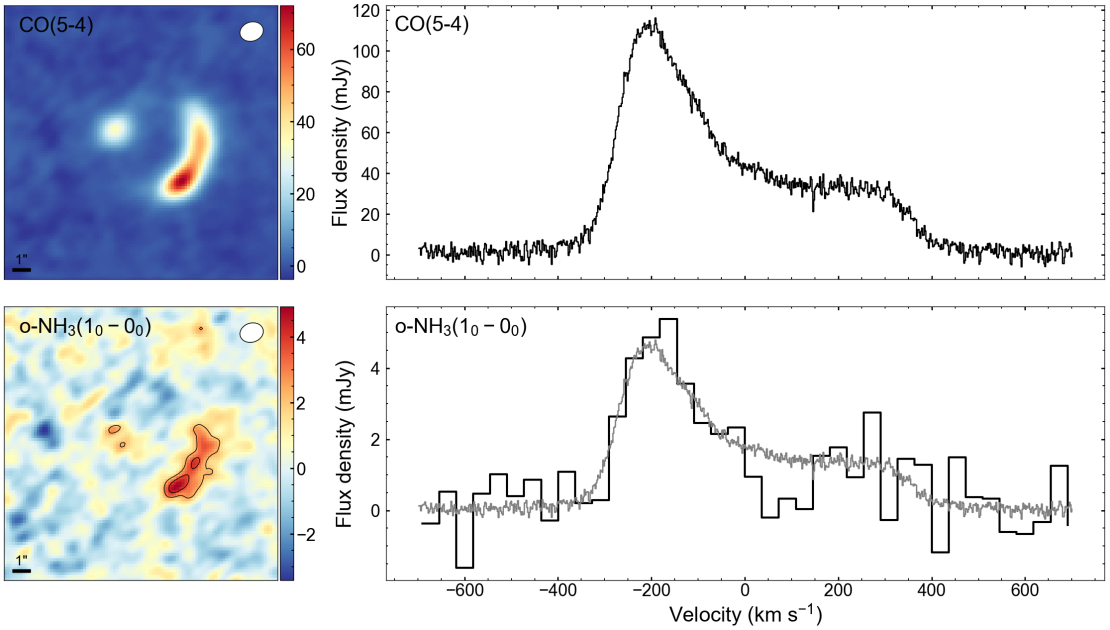

FIGURE 3.1: Maps and spectra for NH_3 and CO(5–4)
Maps and spectra for the NH_3 and CO(5–4) emission in 9io9. (left) Maps show the continuum-subtracted image plane emission averaged over the line with contours shown for the fainter NH_3 starting at 3σ. Synthesised beams are indicated top right. (right) Spectra show the source-integrated emission, with the much brighter CO line acting as a reference profile that can be directly compared with the weaker NH_3, where we overlay a scaled version of the CO(5–4) line to demonstrate the strong similarity between the line profiles, despite NH_3 generally tracing much denser gas (see Section 4 for a discussion). We bin the NH_3 spectrum to $\sim$50 km s^{-1} channels for visualisation purposes. The 'dip' in NH_3 emission at $\sim$100 km s^{-1} is not a significant feature ($\approx 2\sigma$).

(Oteo et al., 2017; Geach et al., 2018; Doherty et al., 2020), possibly via violent disc instabilities (VDIs, e.g. Toomre, 1964; Dekel et al., 2009a,b), and in this case the extreme star formation rates measured can naturally be explained by the sheer quantity of gas available for active participation in star formation (Geach and Papadopoulos, 2012; Papadopoulos and Geach, 2012). We can learn more about the actual conditions of the star-forming ISM, and the conditions of star formation in general by exploiting gravitational lensing to study the astrochemistry of these systems (Danielson et al., 2011; Spilker et al., 2014; Zhang et al., 2018b; Dye et al., 2022). If the density distribution of the cold molecular reservoir is important for driving globally high star formation rates, then observations of species that trace the densest environments are required, particularly heavy rotor molecules (Oteo et al., 2017; Béthermin et al., 2018).

In this work we report the detection of the ground state emission line of ammonia (NH_3) in a (now well-studied) strongly lensed starburst galaxy at $z = 2.6$. A tracer of the dense molecular ISM and intimately linked to the sites of star formation, NH_3 was the first polyatomic molecule

detected in the ISM (Cheung et al., 1968) and is amongst the most studied species in the local universe, primarily through its radio inversion lines (Ott et al., 2011; Schmidt et al., 2016; Fehér et al., 2022). The ground state NH_3 ($J_K = 1_0 \rightarrow 0_0$) ortho line emits at 572.498 GHz in the rest frame, and therefore any ground-based studies of this feature at $z = 0$ are hampered by the near-zero transmission of the atmosphere at this frequency. In Section 2 we present the observations and data reduction, in Section 3 we present our analysis and results, and in Sections 4 and 5 we provide our interpretation and conclusions. Throughout we assume a 'Planck 2015' cosmology where $H_0 = 68$ km s^{-1}Mpc^{-1} and $\Omega_{\rm m} = 0.31$ (Planck Collaboration et al., 2016).

3.2 Observations and data reduction

9io9 (J2000, $02^{\rm h}09^{\rm m}413$, $00^\circ15'58''5$, $z = 2.5543$) was observed with the ALMA 12 m array during project 2019.1.01365.S. The C43-3 configuration was used, employing 48 antennas with baseline separations of 15–784 m. We executed a spectral scan in Band 4 across $\nu_{\rm obs} = 152.5$–162.9 GHz with a total on-source time of approximately 195 minutes over five executions. The precipitable water vapour column was 1.9–3.5 mm and the average system temperature was $T_{\rm sys} = 69$–91 K over the five executions. Atmosphere, bandpass, phase and pointing calibrators included the sources J0423−0120 and J0217+0144. We use the pipeline-restored calibrated measurement set for imaging. We image and CLEANed the data using CASA (v.5.1.0-74.el7) `tclean` with multiscale cleaning at scales of $0''$, $0.5''$, and $1.25''$. First we produce dirty cubes to establish the r.m.s. (1σ) noise per channel, and then cleaned down to a stopping threshold of 3σ. With natural weighting, and setting a common beam to the whole datacube, the synthesized beam has a full width at half maximum of $1.3'' \times 1.0''$ (position angle 72°). The r.m.s. noise per 10 MHz (20 km s^{-1}) channel is 0.3 mJy beam^{-1}.

We adopt the same lens model as Geach et al. (2018). Briefly, the lens model includes the gravitational potential of both the primary lensing galaxy ($z \approx 0.2$) and its smaller northern companion (assumed to be at the same redshift). The model uses the semi-linear inversion method of Warren and Dye (2003) to reconstruct the source plane surface brightness that best matches the observed Einstein ring for a given lens model. This process is iterated, varying the lens model and creating a source reconstruction at each iteration, until the global best fit lens model is found (Geach et al., 2018). The best fit model is used to produce source-plane cubes. In the following, we use the source-plane cube to extract the integrated spectrum, accounting for

magnification of the sources of line emission. However, due to the relatively coarse resolution and signal to noise of the data, we present maps of 9io9 in the image plane.

3.3 Results

We use *Splatalogue* (Remijan et al., 2007) to identify emission lines in the total spectrum. CO $J = 5 \rightarrow 4$ at $\nu_{\rm obs} = 162.133$ GHz is detected at high significance as expected, and exhibits the characteristic double horned profile as other molecular and atomic lines (Geach et al., 2015, 2018; Harrington et al., 2019; Doherty et al., 2020), and well-modelled in the source-plane reconstruction by a rotating disc (Geach et al., 2018). We also detect a fainter, but significant, emission feature at $\nu_{\rm obs} = 161.072$ GHz that is consistent with the redshifted ground state ortho-NH_3 $J_K = 1_0 \rightarrow 0_0$ rotational line at $\nu_{\rm rest} = 572.498$ GHz (Cazzoli et al., 2009, hereafter we refer to the line as NH_3). Image plane integrated spectra of the CO $J = 5 \rightarrow 4$ (hereafter CO(5–4)) and NH_3 lines and maps are presented in Figure 3.1. To our knowledge, the previous highest redshift detection of this transition of ammonia was in absorption in a spiral galaxy at $z = 0.89$, where the galaxy is acting as a lens, magnifying the strong (sub)millimeter continuum emission of the famous background quasar PKS 1830−211 at $z = 2.51$ (Menten et al., 2008; Muller et al., 2014).

To measure the line properties, we subtract continuum emission on a pixel-by-pixel basis, using a simple linear fit to the spectrum in line-free regions around NH_3. We then model the integrated line emission using an empirical template based on the high SNR CO(5–4) emission line. By simply shifting the position of the CO(5–4) emission in frequency space and scaling its amplitude, we can minimise the χ^2 difference between the scaled CO(5–4) and the NH_3 line. Figure 3.1 shows how the scaled CO(5–4) line provides an excellent fit to the NH_3 emission. We discuss the implications of this later. The total integrated line flux is evaluated by summing the flux within an aperture defined by the 3σ contour of the averaged band 4 data cube. We measure $\mu L_{\rm NH_3} = (3.3 \pm 0.2) \times 10^7 L_\odot$, where μ is the lensing magnification. To estimate uncertainties in this procedure, we simply add Gaussian noise to each channel, with a σ determined from the r.m.s. in off-source regions of the data cube and then repeat the fit 1000 times. Applying this same procedure to the source plane reconstructions, we obtain a source plane line luminosity of $L_{\rm NH_3} = (2.8 \pm 0.2) \times 10^6 L_\odot$. If instead of using the scaled CO(5–4) as a model of the emission, we just integrate over the range $\Delta V = \pm 500$ km s^{-1}, we obtain a source plane luminosity of $L_{\rm NH_3} = (3.1 \pm 0.3) \times 10^6 L_\odot$.

3.4 Interpretation

As can be seen from Figure 3.1, the scaled CO(5–4) emission is an excellent description of the NH_3 line emission. In turn, the line profile of the integrated, projected CO emission is well modelled by a nearly edge-on rotating disc (when modelled in the source plane and projected into the image plane) and this profile is shared by the majority of detected lines within this system covering a wide range of conditions, from the relatively low density molecular reservoir traced by C I (1–0) to the warmer, dense, ionised gas traced by N^+ (Su et al., 2017; Geach et al., 2018; Harrington et al., 2019; Doherty et al., 2020). The striking similarity in the observed line profiles imply that the observed NH_3 emission is broadly co-located with the CO-emitting gas, likely emanating from discrete sites of on-going star formation scattered throughout the gas-rich disc.

Ho and Townes (1983) note that NH_3 is a rather ubiquitous molecule, tracing a broad range of interstellar environments containing molecular gas. However, for the rotational transitions in the millimetre, NH_3 is expected to trace dense gas. In the optically thin limit, the critical density of NH_3 is $n_{\rm crit} \gtrsim 10^7\,{\rm cm}^3$ for kinetic temperatures $T_k < 100\,{\rm K}$ (Shirley, 2015). In realistic scenarios, the NH_3 emission will be optically thick, and therefore subject to radiative trapping (Draine, 2011). This serves to lower the effective critical density, but even so, the effective densities for optically thick NH_3 emission are still probing dense gas, with $n_{\rm eff} \gtrsim 5 \times 10^4\,{\rm cm}^3$ for $T_k < 100\,{\rm K}$ and assuming a column density commensurate with dense gas clumps and cores in the Milky Way ($\log_{10}(N_{\rm ref}/{\rm cm}^{-2}) = 14.3$, Shirley (2015)). However, the effective density will further scale down with increasing column density as $N_{\rm ref}/N$. Another caveat is the presence of significant far-infrared background fields, which will be dominated by the ambient radiation field of the galaxy itself due to dust emission, with the most intense emission likely co-located with the dense star-forming gas. This background could lead to significant radiative pumping of NH_3 molecule and therefore a non-collisional route to rotational emission; indeed Schmidt et al. (2016) discuss the potential role of pumping of the NH_3 rotational ground state emission as a solution to the discrepancy between the abundances derived via the NH_3 ground state and its radio inversion lines in some local systems. While radiative pumping would further serve to lower the effective density of the gas responsible for NH_3 emission, we can be reasonably confident that the observed NH_3 is tracing some of the densest molecular gas in 9io9, and therefore the actual sites of star formation.

TABLE 3.1: A comparison of the properties of 9io9 and Galactic sources where NH_3 is detected in emission.

Source	L_{IR} $L_\odot$	L_{NH_3} $L_\odot$	L_{NH_3}/L_{IR} $\times 10^{-7}$
9io9 (this work)	1.1×10^{13}	2.8×10^6	2.5
Orion-KL	8×10^4	0.01	1.3
W31 C	$\sim 10^6$	>0.042	>0.42
W49 N	$\sim 10^7$	>0.048	>0.48

Can we relate the properties of 9io9 to local star formation? Doherty et al. (2020) show that the average electron density ($n_e \approx 300\,cm^{-3}$) associated with warm ionised gas as traced by N^+ fine-structure emission is consistent with the typical density of Galactic star-forming regions. The conclusion is that the conditions are not 'extreme' compared to sites of active star formation in the Milky Way, but clearly a larger fraction of the ISM is participating in star formation in 9io9 and galaxies like it compared to the Milky Way. What of the efficiency, or 'mode' of star formation? A crude approach is to compare proxies for the star formation rate and dense gas that is fuelling it; more efficient star formation is characterised by a higher rate per unit dense gas mass, with a theoretical upper limit set by the Eddington limit (Murray et al., 2005). With the integrated infrared luminosity as a proxy for the total star formation rate (for galaxies dominated by dust) and NH_3 as a tracer of the dense molecular gas actively participating in star formation, we can use L_{IR}/L_{NH_3} as an empirical tracer of the star formation efficiency. In 9io9 we measure $L_{NH_3} = 2.8 \times 10^6 L_\odot$ and luminosity of $L_{IR} = 1.1 \times 10^{13} L_\odot$, yielding $L_{NH_3}/L_{IR} \approx 3 \times 10^{-7}$.

There are relatively few regions where we have robust and integrated infrared luminosities. One such region, the Kleinmann–Low nebula in Orion (Orion-KL) – a dense, hot molecular cloud core close to the Trapezium cluster, which excites the Orion Nebula – is frequently used as a local benchmark in many studies, not the least because of its proximity at ∼400 pc. With $L_{IR} \sim 8 \times 10^4\ L_\odot$ (Gezari et al., 1998) and $L_{NH_3} \approx 0.01 L_\odot$ (Olofsson et al., 2007; Persson et al., 2007), Orion-KL has $L_{NH_3}/L_{IR} \approx 1.3 \times 10^{-7}$, within a factor of a few of the 'global' 9io9 ratio, despite eight orders of magnitude separating the infrared luminosities.

While the Orion molecular clouds have been extensively studied (e.g. Genzel and Stutzki, 1989), we note that it has been argued that the energetics of Orion-KL are not dominated by high mass star formation, but rather by an explosive stellar merger event (Zapata et al., 2011). Although one would expect a correspondingly high density of supernovae in 9io9, Orion-KL is arguably not a typical region in which presently *high mass stars* are forming. In contrast W31 C

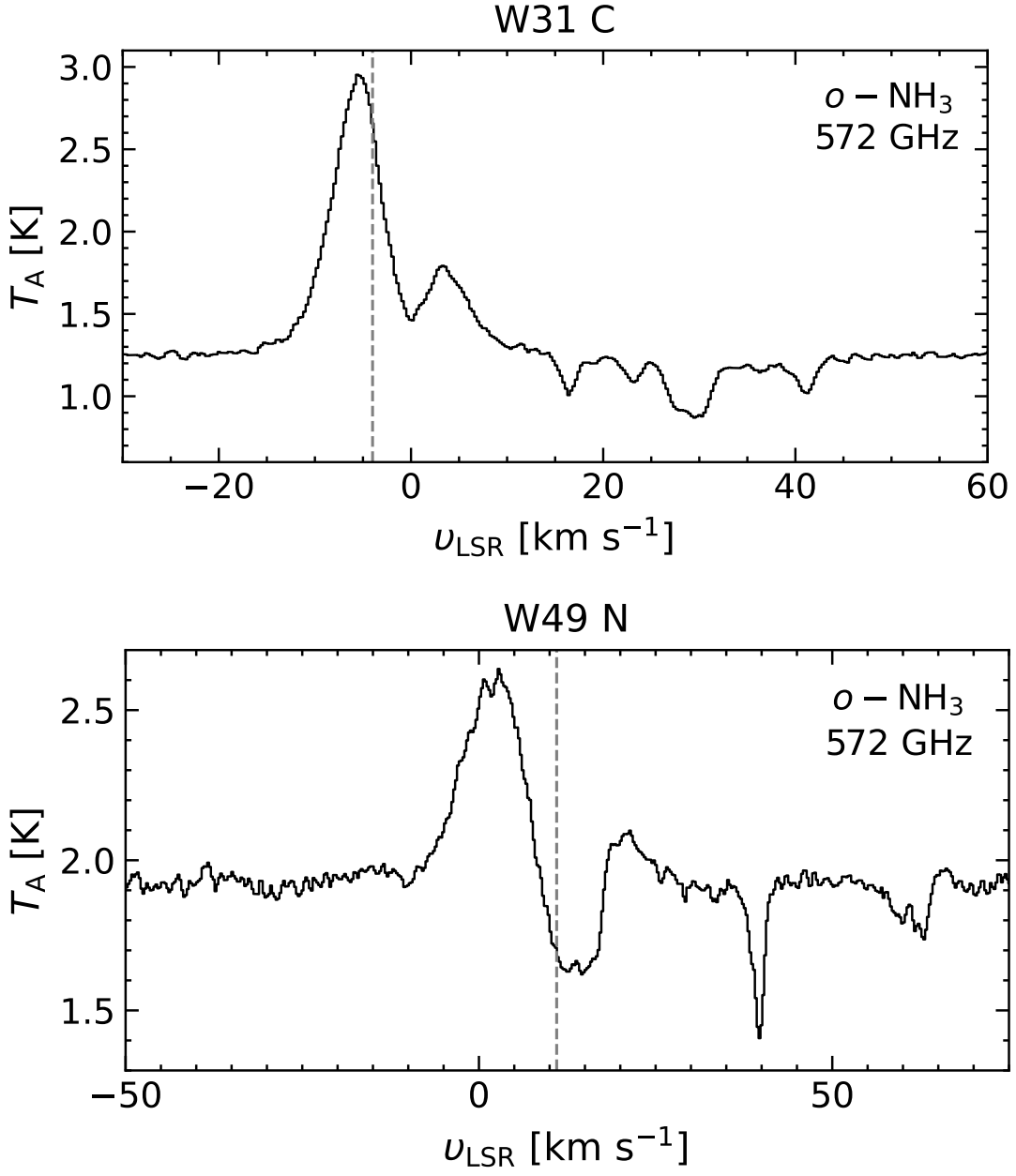

FIGURE 3.2: Ortho-NH_3 line profiles for W31 C and W49 N
The ortho-$NH_3(1_0–0_0)$ line towards W31 C (top) and W49 N (bottom) observed using *Herschel*/HIFI. Vertical dashed grey lines mark the systemic velocities of the two sources.

(G10.6−4) ($L_{\rm IR} \sim 10^6 L_\odot$) and the 'mini-starburst' W49 N ($L_{\rm IR} \sim 10^7 L_\odot$ Wright et al., 1977) are luminous Galactic high-mass star-forming regions located at distances of 4.8 kpc and 11.2 kpc, for which observations of the line have been published (Persson et al., 2010, 2011). Toward both sources, the spectra were taken as part of the *Herschel* key guaranteed time project PRISMAS[1] using the Heterodyne Instrument for the Far-Infrared (HIFI). Unlike the corresponding para-NH_3 lines, which show almost exclusively absorption, toward both W49 N and W31 C, the spectra of the ortho- line is far more complex, displaying strong emission at the velocities of the background sources with self-absorption features slightly offset from the systemic velocities (Figure 3.2). We model the emission by fitting Gaussian profiles centred at the systemic velocity of each source with the line widths optimised to fit the emission wings. Subsequently, the self-absorption features modelled using narrower Gaussian profiles centred at 0 km s^{-1} and 13 km s^{-1} for W31 C and W49 N, respectively, are removed. The resulting fits are then used to derive integrated line intensities of 6.33 K km s^{-1} and 1.33 K km s^{-1} for W31 C and W49 N, respectively. Using a conversion factor of 482 Jy/K this yields line luminosities $L_{\rm NH_3} = 0.042 L_\odot$ and $L_{\rm NH_3} = 0.048 L_\odot$, and $L_{\rm NH_3}/L_{\rm IR}$ of 4.2×10^{-8} and 4.8×10^{-8} toward W31 C and W49 N, respectively. The NH_3 line luminosities should be considered lower limits due to uncertainties in the line intensities estimated and the nature of the observed self-absorption. If there is significant self-absorption of the NH_3 emission when averaged over galaxy scales in 9io9, then our measured luminosity could also be considered a lower limit. In Table 3.1 and Figure 3.3 we compare the luminosity ratios we derive for the Galactic sources with 9io9. The ratios are broadly consistent within a factor of a few, despite the fact that the 9io9 measurement is galaxy-integrated across a system with an overall rate of star formation several orders of magnitude greater than the Milky Way.

3.5 Conclusions

The actual structure of star-forming regions in gas-dominated, high-redshift discs such as 9io9 remains unclear. While some studies have argued for the presence of 'giant clumps' with properties similar to the cores of local Giant Molecular Clouds, but scaled up to sizes of order 100 pc (e.g. Rybak et al., 2015; Hatsukade et al., 2015), others have pointed out that the reality of such features is questionable, and that star formation may well be smoother, or structured on smaller

[1] PRobing InterStellar Molecules with Absorption line Studies (PI: M. Gerin)

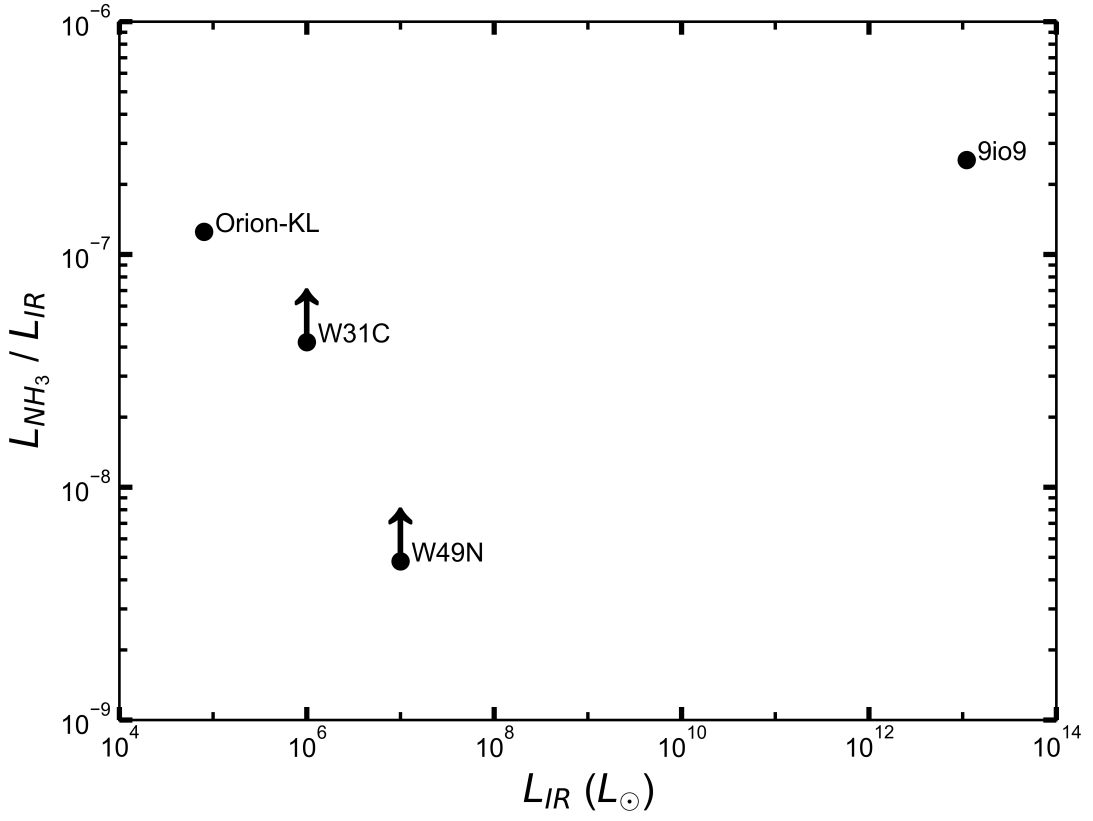

FIGURE 3.3: NH_3 verses L_{IR} for a range of sources
A comparison of the $L_{\rm NH_3}/L_{\rm IR}$ ratio versus $L_{\rm IR}$ for 9io9 at $z = 2.6$ and a small sample of Galactic sources where is detected. The x-axis spans ten orders of magnitude in infrared luminosity, whereas the luminosity ratios are consistent within a factor of 10.

scales than can be reliably imaged interferometrically, even with the assistance of lensing (Ivison et al., 2020). Regardless, it is evident that in order to drive globally elevated star formation, a large fraction of the cold ISM must be driven to high densities.

The introduction of supersonic turbulence is a key mechanism to achieve high gas density fractions (Geach and Papadopoulos, 2012), with the dispersion of the log-normal distribution describing the molecular gas density sensitive to the 1-dimensional average Mach number: $\mathscr{M} = \sigma_v/c_s$, with σ_v the gas velocity dispersion and c_s the speed of sound in the medium (Padoan and Nordlund, 2002). In the local Universe, mergers drive up $\mathscr{M}$ (e.g. Narayanan et al., 2011), and is the primary mechanism for ultraluminous emission in galaxies (Solomon and Vanden Bout, 2005). 9io9 – like many other high redshift starbursts – does not appear to be undergoing a major merger (although see Liu et al., 2022), but VDIs (Dekel et al., 2009b; Inoue et al., 2016) are a viable alternative mechanism for locally driving up $\mathscr{M}$ resulting in pockets of high-density gas, and therefore star formation, across the gas-dominated disc. Confirming this in

practice will require reliable high-resolution imaging (noting the caveat referenced above for interferometric data) that could map out the relative distribution of dense molecular gas compared to the bulk reservoir. It is important to note that minor mergers and interactions can catalyse VDIs (e.g. Swinbank et al., 2011; Saha and Cortesi, 2018).

That a large fraction of the molecular ISM in 9io9 resembles environments like Orion-KL and other Galactic environments, with the broad kinematics of NH_3 consistent with ordered disc rotation across the full range of molecular gas densities, we can picture an ensemble of millions of 'Orion-KLs' embedded throughout the compact disc of 9io9; perhaps individually unremarkable, but en masse driving globally high star formation. This echos the evocative picture Rybak et al. (2020) present of another dusty, star-forming lensed galaxy, SDP.81 ($z \approx 3$): they describe the system as 'full of Orions', based on the similarity of the ISM conditions on sub-kpc scales in SDP.81 compared to Orion. Our results appear to support this picture, and highlight the utility of the fainter, heavy rotor tracers in revealing the structure of the high-density ISM that is physically proximate with active star formation in young massive galaxies.

Chapter 4

^{13}CO/C^{18}O in a lensed hyperluminous galaxy: implications for the stellar initial mass function in distant starbursts

Abstract

We present new Atacama Large Millimetre/submillimetre Array (ALMA) observations of the lensed hyperluminous starburst galaxy '9io9' at $z = 2.554$, detecting CO J=5$\rightarrow$4 and its isotopologues ^{13}CO J=5$\rightarrow$4 and C^{18}O J=5$\rightarrow$4. Since ^{13}C is mainly produced by intermediate-mass stars and ^{18}O is produced by massive stars, ^{13}CO/C^{18}O is sensitive to the shape of the stellar initial mass function (IMF), where the IMF of the Milky Way has a power law slope $\alpha_2 \approx 2.3$–2.6 for stars of masses above $0.5\,M_\odot$. We measure a galaxy-integrated luminosity ratio ^{13}CO/C^{18}O $= 1.6 \pm 0.1$, consistent with the ratio observed in local ultraluminous infrared galaxies and submillimetre-selected galaxies at high redshift, and significantly lower than the ^{13}CO/C^{18}O of the Milky Way. It has been argued that the low ^{13}CO/C^{18}O observed in extreme star-forming galaxies in the early Universe is evidence for a top-heavy IMF in these systems. In this work we use state-of-the-art chemical evolution models to conclude that irrespective of stellar rotation, the observed ^{13}CO/C^{18}O is consistent with a Kroupa IMF with high-mass slope of $\alpha_2 = 2.3$ (as in our Milky Way models) and also the steeper 'top-heavy' $\alpha_2 = 2.1$ slope.

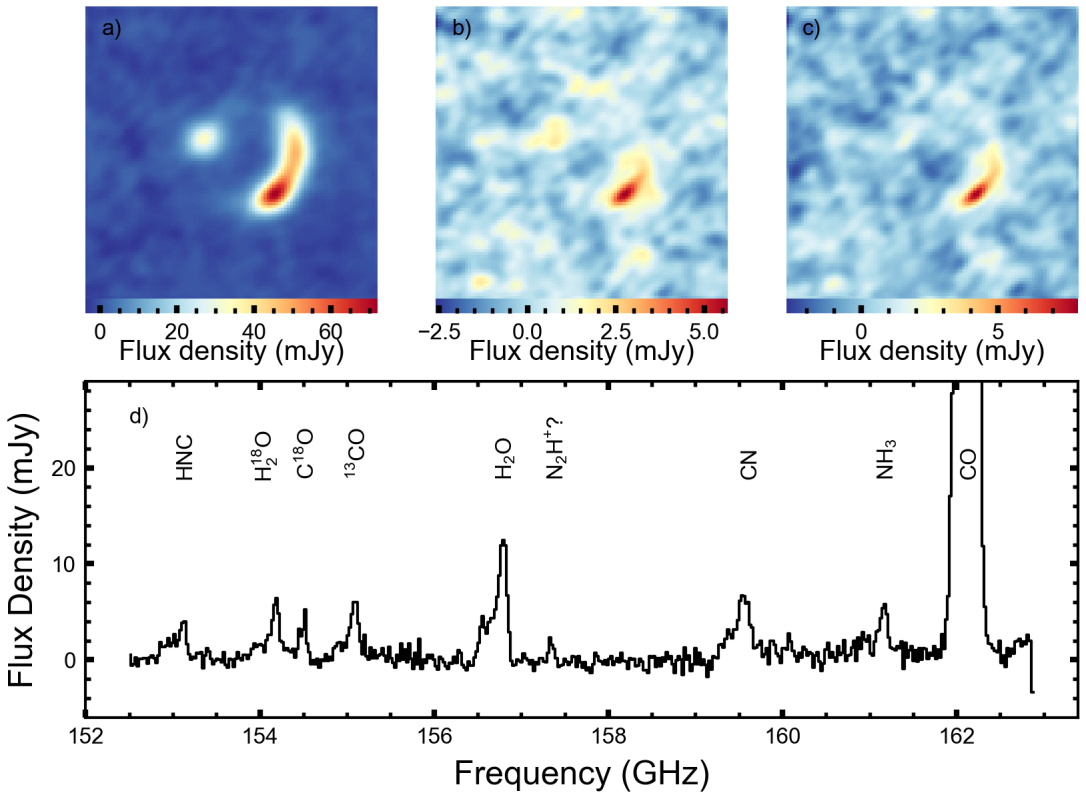

FIGURE 4.1: ALMA maps for CO J=5→4, ^{13}CO and C^{18}O emission, alongside full spectral scan

ALMA observations of 9io9. Panels (a)–(c) show the continuum-subtracted CO J=5→4, ^{13}CO and C^{18}O emission, respectively, in the image plane; panel (d) shows the source-integrated ALMA spectral scan with a diverse range of species being detected. The NH_3 line is discussed in (Doherty et al., 2022) and the other lines not discussed here will be discussed in future work (Doherty et al., in prep).

4.1 Introduction

For decades, star formation in high-redshift galaxies has been assumed to follow a Milky Way-like stellar initial mass function (IMF, Salpeter, 1955; Kroupa, 2001; Chabrier, 2003). Under this assumption, the population of submillimetre-selected galaxies (SMGs), and indeed dusty star-forming galaxies (DSFGs) in general at $z > 1$ are predicted to have star-formation rates (SFRs) of 1000 $M_\odot$ yr^{-1} or more (e.g. Smail et al., 1997; Hughes et al., 1998; Barger et al., 2014). Those at the highest redshifts (e.g. Riechers et al., 2013; Fudamoto et al., 2017) can therefore assemble a large fraction of their stellar mass very quickly in the early Universe (e.g. Oteo et al., 2017; Miller et al., 2018). Indeed, there is evidence for the rapid accumulation of passive galaxies in proto-clusters by $z \approx 3$ (e.g. McConachie et al., 2022). Clearly SMGs and the like represent some of the most luminous galaxies in the Universe, but models of galaxy

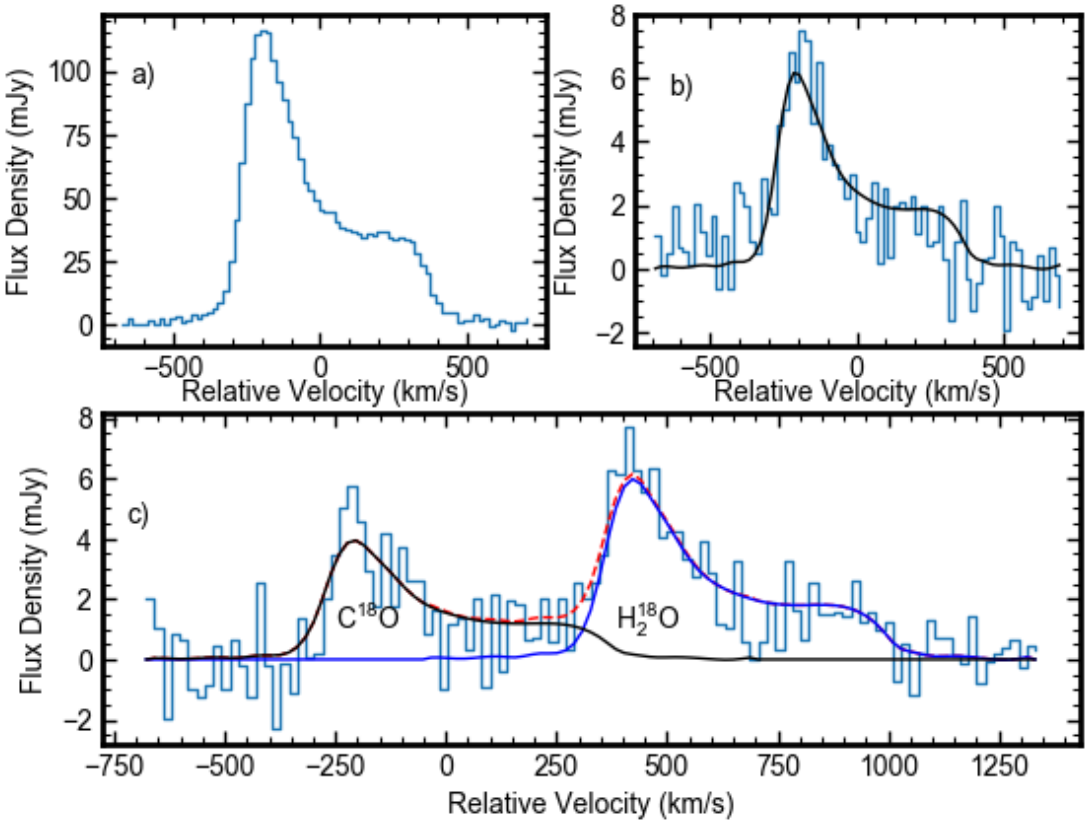

FIGURE 4.2: CO spectra including fits.
CO spectra for 9io9. Panel a) is the CO J=5→4 emission; panel (b) contains the ^{13}CO J=5→4 emission with the best-fit model overlaid; panel (c) includes the C^{18}O J=5→4 emission blended with $H_2^{18}O$.

formation have often struggled to reproduce galaxies with such extreme SFRs (e.g. Baugh et al., 2005; Swinbank et al., 2008; Davé et al., 2010; Hayward et al., 2013, cf. Lovell et al. 2021). This motivates investigations of the true nature of star formation in these systems.

The stellar IMF describes the abundance of stars of different mass and is typically parameterised as a broken power law. For the Milky Way, this takes the form $\xi(m) = m^{-\alpha}$, with $\alpha = 0.8, 1.3, 2.3$ for stellar masses $M < 0.08$, 0.08–0.5 and $\geq 0.5\,M_\odot$, respectively (Kroupa, 2001), though other formulations exist and some argue that $\alpha_2 = 2.7$ is required at $M \geq 0.5\,M_\odot$ to avoid over-producing metals (e.g. Romano et al., 2005). Generally, if the IMF is described as being 'top heavy', this means it has a high abundance of massive (typically meaning $M > 8\,M_\odot$) stars relative to the Milky Way, with the corollary that there is still debate on the nature of the Galactic IMF. In any case, increasing the relative abundance of high mass stars means that a *lower* SFR is required to generate a given luminosity. The conditions within SMGs are certainly different from the Milky Way, where the properties of their interstellar medium (ISM) and its

incident radiation field – the dramatically higher cosmic ray flux, for example – are expected to play an important role in shaping the IMF (e.g. Padoan and Nordlund, 2002; Krumholz, 2006; Bate, 2009; Hopkins, 2013; Bisbas et al., 2015, 2017).

There is some evidence from the local Universe that the IMF becomes top heavy in intensely star-forming environments (e.g. Motte et al., 2018; Pouteau et al., 2022). For example, in 30 Doradus, sometimes taken as an analogue to the low-metallicity, starbursting conditions of some high-redshift galaxies, Schneider et al. (2018) present evidence for a 32 ± 12 per cent overabundance of stars with $M > 30\,\mathrm{M}_{\odot}$ relative to a Salpeter IMF (Salpeter, 1955). If the IMF in luminous galaxies at large redshifts is different – more top-heavy – to the Milky Way, then this has profound consequences for our understanding of the star formation history of the Universe. If SMGs are the progenitors of the most massive elliptical galaxies today, having formed a large fraction of their stars in conditions where a different IMF applied, then the surviving, low mass population of stars in their descendants should give us insight as a 'fossil record' (e.g. Smith et al., 2017). Confusingly, this archaeological evidence suggests that the central stellar populations of local ellipticals formed from a *bottom-heavy* IMF, at least for $M < 1\,\mathrm{M}_{\odot}$, with shallower slopes preferred at $M > 1\,\mathrm{M}_{\odot}$ (see Smith, 2020, for a review).

Counting stars or young stellar objects, which is the most direct method for actually measuring the IMF, becomes impossible at cosmological distances. Alternative, indirect methods are required. A promising technique exploits the chemical signature imprinted on the ISM by massive stars. In particular, the ^{13}C/^{18}O abundance ratio is expected to be sensitive to the shape of the IMF, because ^{18}O is primarily produced in stars with $M > 8\,\mathrm{M}_{\odot}$, whereas ^{13}C is produced in low- and intermediate-mass stars (4–7 $\mathrm{M}_{\odot}$, Kobayashi et al., 2011). After deposition in the ISM, these isotopes become locked into the isotopologues of the abundant and readily observable CO molecule, whose rotational transitions are accessible in the sub-mm/mm window across nearly all of cosmic history.

Zhang et al. (2018b) measured ^{13}CO/C^{18}O in a sample of lensed (note that the isotopologue emission is intrinsically faint) $z \approx 2$–3 SMGs, finding a value close to unity, similar to that found in local ultraluminous infrared galaxies (ULIRGs) and an order of magnitude below typical star-forming disks like the Milky Way. The trend of increasing contribution from C^{18}O with increasing L_{IR} (and therefore SFR) hints at a systematic variation in the abundance of ^{18}O in the intensely star-forming environments of SMGs. Using the chemical evolution model of Romano et al. (2017), which is benchmarked on the Milky Way Zhang et al. (2018b) argued

that the ^{13}CO/C^{18}O ratios of around unity observed in local ULIRGs and high-redshift SMGs are evidence of a top-heavy IMF, at least in their current starbursts. Romano et al. (2019) updated this analysis to include new chemical yields for massive stars with rotation (Limongi and Chieffi, 2018), finding that SMGs require a top-heavy ($\alpha_2 < 2.7$) IMF if the conditions of their ISM favour the formation of rapidly rotating stars. In contrast, a universal IMF can suffice if conditions are unfavourable to the formation of massive stellar fast-rotators. However, clearly a larger sample is required to build up a more representative picture of ^{13}CO/C^{18}O in SMGs at the same epoch.

Here we present a measurement of ^{13}CO/C^{18}O in another strongly lensed SMG, known as 9io9, at $z = 2.6$ (Geach et al., 2015, 2018; Doherty et al., 2020) with the Atacama Large Millimetre/-submillimetre Array (ALMA). Even after correcting for lensing magnification, 9io9 is an intrinsically hyperluminous galaxy, with $L_{\rm IR} > 10^{13}\,{\rm L}_{\odot}$. The bulk of this luminosity is associated with star formation across a 2.5 kpc disk (Geach et al., 2018), and therefore it is an excellent example of (apparently) rapid stellar assembly in a gas-rich rotation dominated system close to the peak of galaxy formation where lensing provides access to emission lines otherwise inaccessible or prohibitively expensive to observe. In §2, we present the observations and data reduction; in §3, we present our results and analysis; in §4, we put forward our interpretation and discussion and conclude in §5. Throughout we assume a cosmology where $H_0 = 68\ {\rm km\,s^{-1}\,Mpc^{-1}}$ and $\Omega_{\rm m} = 0.31$ (Planck Collaboration et al., 2016).

4.2 Observations and data reduction

9io9 ($02^{\rm h}09^{\rm m}413$, $00^{\circ}15'58''5$, $z = 2.5543$) was observed with the ALMA 12-m array as part of project 2019.1.01365.S. The C43-3 configuration was used, employing 48 antennas with baseline separations of 15–784 m. We executed a spectral scan in ALMA band 4 across $\nu_{\rm obs} =$ 152.5–162.9 GHz, designed to span the ^{12}CO, ^{13}CO and C^{18}O $J = 5 \rightarrow 4$ lines, with five executions and a total resulting on-source time of ≈ 195 min. The precipitable water vapour column was 1.9–3.5 mm and the system temperature ranged across $T_{\rm sys} = 69$–91 K for the five executions. Flux density, bandpass and phase calibrators included J0423−0120 and J0217+0144.

We started from the calibrated measurement set produced by the ALMA Science Pipeline. We imaged and cleaned the data using `tclean`, part of CASA (v.5.1.0-74.el7), with multi-scale cleaning at scales of $0''$, $0.5''$ and $1.25''$. First, we produced dirty cubes to establish the r.m.s.

(1σ) noise per channel, and then we cleaned down to a stopping threshold of 3σ. With natural weighting, setting a common beam for the whole datacube, the synthesised beam had a full width at half maximum (FWHM) of $1.3'' \times 1.0''$ (at position angle, 72°). The r.m.s. noise per 10 MHz (20 km s^{-1}) channel was 0.3 mJy beam^{-1}. In Fig. 1 we present our cleaned images of the ^{12}CO, ^{13}CO and C^{18}O $J = 5 \rightarrow 4$ emission, in the image plane, as well as the galaxy-integrated spectrum.

4.3 Results

Since a reliable lens model exists for 9io9 (see Geach et al., 2018, for details), we apply the lens inversion to produce a source-plane datacube. All subsequent analysis is performed in the source plane.

We use *Splatalogue* (Remijan et al., 2007) to identify emission lines in the integrated spectrum. As well as CO emission lines, we identify H_2O, HNC, NH_3, and $H_2^{18}O$ (see Fig. 4.1). These will be the subject of future analysis (Doherty et al., in prep). As expected, the strongest spectral feature is ^{12}CO $J = 5$–4, which has the same characteristic double-horned profile observed previously in ^{12}CO $J = 4$–3, C I 1–0 and [N II] (Geach et al., 2018; Doherty et al., 2020). The C^{18}O $J = 5$–4 line is blended with $H_2^{18}O$ but the majority of lines share the same characteristic profile in the integrated spectrum so following Doherty et al. (2022) we use the high signal-to-noise CO J=5→4 line – which is not blended with other lines – as an empirical template that can be shifted and re-normalised to deblend the C^{18}O $J = 5$–4 and $H_2^{18}O$ emission. Although ^{13}CO is not blended with another line, we also model it with the ^{12}CO template.

We subtract continuum emission on a pixel-by-pixel basis, using a simple linear fit to the spectrum in line-free regions. Next, we model the CO J=5→4 line with a cubic spline with the smoothing parameter set to the noise scale. This is used to create the template for de-blending, which we use as a model for the two isotopologues of interest and their neighbouring lines, assuming all lines are at $z = 2.554$. After fixing the template spectrum to the redshifted frequency of each line, we scale the amplitude of the template, minimising the χ^2 residual between the scaled template and the data. Fig. 2 shows the best fits for the ^{13}CO and C^{18}O lines. To estimate uncertainties on the fits we add Gaussian noise to each channel, with a scale determined from off-source regions of the datacube. We take the standard deviation of the pixel-to-pixel channel noise and scale by the solid angle subtended by the 3σ contour used to define the total

emission. We repeat the fitting procedure 1,000 times for each realisation to estimate the 1σ uncertainty of the model normalisation (and therefore velocity integrated flux $S\Delta V$) for each line. We evaluate line luminosities by integrating $S\Delta V$ for each de-blended emission line, then scale by the luminosity distance. We measure integrated fluxes of 1.41 ± 0.05, 0.96 ± 0.06 and 30.5 ± 0.3 Jy km s^{-1} for the ^{13}CO, C^{18}O and ^{12}CO emission lines, respectively. These correspond to luminosities of $L_{^{13}\mathrm{CO}} = (1.05 \pm 0.04) \times 10^8\,\mathrm{L}_\odot$, $L_{\mathrm{C}^{18}\mathrm{O}} = (7.10 \pm 0.50) \times 10^7\,\mathrm{L}_\odot$ and $L_{^{12}\mathrm{CO}} = (2.37 \pm 0.03) \times 10^9\,\mathrm{L}_\odot$, respectively, using the standard relation found in Solomon et al. (1997).

The typical ^{13}CO/C^{18}O line ratio observed in local spiral disks is approximately 7–10 (Jiménez-Donaire et al., 2017). In contrast, we measure $^{13}\mathrm{CO/C}^{18}\mathrm{O} = 1.6 \pm 0.1$, consistent with the line ratios of close to unity observed by Zhang et al. (2018b) in four lensed SMGs at $z = 2.3$–3.1, in the 'Cosmic Eyelash' at $z = 2.3$ (Danielson et al., 2013) as well as local ultraluminous systems such as Arp 220 and Mrk 231 (Brown and Wilson, 2019).

4.4 Interpretation and discussion

Before discussing the various effects which could affect the observed ratio it is worth briefly discussing our use of a mid-J (5-4) transitions instead of a lower-J transition (where 1-0 is the gold standard) which are typically employed, and some assumptions which may bias the results. As mid-J lines have higher critical densities, this means that the bulk of their emissions arise from denser parts of the ISM, which will miss a large fraction of the total CO masses within the ISM. When converting from a higher J transition, you must use a conversion factor to convert this into an equivalent 1-0 luminosity which can then be used to obtain a total mass within the ISM. This conversion factor will vary with the transition and between galaxies due to the different distributions of gas densities within, as well as the excitation conditions of the gas. As we are using the line ratio of ^{13}CO/C^{1}8O and assume that the conditions in which C^{1}8O and ^{13}CO find themselves are the same and that ^{13}CO is not significantly optically thick, such that the 5-4 and 1-0 ratios will be approximately the same.

Perhaps the biggest limitation of this work, is our use of an integrated flux measurement. We assume in this work that the integrated ratio approximately matches the underlying molecular ratio, the CO emission in this integrated value will arise from many regions of the galaxy covering a range of densities, excitations, and levels of gas processing. Martín et al. (2019) argued using

resolved ^{13}CO and C^{18}O measurements of NGC 253 that the multicomponent nature of the CO emission and optical depth effects could complicate the interpretation of integrated results.

In the following section we discuss a range of effects that could also effect the derived ratio.

4.4.1 Factors affecting the isotopologue ratio

There are several factors that could affect the observed isotopologue ratio. First, we consider line opacity. The CO isotopologues are usually assumed to be optically thin, but if ^{13}CO is optically thick, this would of course affect the observed ratio. Zhang et al. (2018b) showed that even for modest ^{13}CO optical depths, $\tau \sim 0.3$–0.5, under local thermal equilibrium (LTE) conditions ^{13}CO/C^{18}O would only vary by 10–20 per cent. An observed line ratio of approximately unity would then require extreme column densities, $N(\mathrm{H_2}) \gtrsim 10^{25}\,\mathrm{cm^{-2}}$. Whilst extreme, densities approaching this may be present within SMGs, taking a simple model of an edge on homogenous disc of gas, of constant scale height h and radius r, the column density of gas would be given by $\frac{M_{H2}}{m_H r h}$, taking the gas mass to be $M_{H2} \approx 10^{10} M_{\odot}$, $r = 3kpc$ and the scale height $h = 1kpc$, one would obtain a column density of $N_{H2} \approx 10^{24} cm^{-2}$, requiring an overdensity of approximately 10 to produce the densities required for this optical depth. However considering the ^{12}CO/^{13}CO abundance ratio in the Milky Way (^{12}CO/^{13}CO ≈ 70), Zhang et al. (2018b) showed that the ^{12}CO/^{13}CO ratio approaches unity before the ^{13}CO/C^{18}O ratio, meaning that it is difficult to attribute a low ^{13}CO/C^{18}O to optical depth effects since it would then be hard to explain the high observed ^{12}CO/^{13}CO ratio. We therefore argue that the low ^{13}CO/C^{18}O relative the the Milky Way is not due to optical depth effects, however ^{1}3CO could still be moderately optically thick and the optical depth effects have to be considered with respect to the various IMF predictions. For example as can be seen from figure 4.5 the predicted ratio from a $K_{2.3}$ IMF lay between $5 \gtrsim ^{13}$CO/C^{18}O$\gtrsim 1.5$, for the various models. In this case a moderate optical depth on ^{13}CO as described above could potentially explain the difference between the predicted ratio and that of the Zhang et al. (2018b) average. We note that to assess the effects of optical depth in full will require further observations of multiple CO transitions, along with the corresponding isotopologues.

Next, we explore if photochemical effects can explain the observed ratio. For the rarer isotopologues, preferential photodissociation can occur due to a lack of self-shielding, i.e. a larger fraction of ^{13}CO and C^{18}O molecules are exposed to the local UV radiation field and are therefore more susceptible to destruction (Visser et al., 2009). However, if the intrinsic abundance

ratio of $^{13}C/^{18}O \geq 1$ (and so $^{13}CO/C^{18}O \geq 1$) then preferential photodissociation would tend to destroy $C^{18}O$ at a higher rate than ^{13}CO, leading to a higher observed $^{13}CO/C^{18}O$. It is unlikely, therefore, that preferential photodissociation can explain the low observed $^{13}CO/C^{18}O$ line ratio, as argued by Romano et al. (2017) and Sliwa et al. (2017).

Chemical fractionation can occur in cold environments where ion-molecule chemistry dominates, and could also impact $^{13}CO/C^{18}O$. This process could lead to enhanced production of ^{13}CO due to the reaction $^{13}C^{+} + {}^{12}CO \rightleftharpoons {}^{12}C^{+} + {}^{13}CO + \Delta E$, where $\Delta E = 35$ K (Jiménez-Donaire et al., 2017). The analogous reaction for oxygen, $^{18}O^{+} + C^{18}O \rightleftharpoons {}^{16}O^{+} + C^{18}O$ has an activation energy barrier which is not favoured under normal conditions (Watson, 1978) and this reaction can therefore be ignored. The implication is that chemical fractionation would lead to preferential production of ^{13}CO with respect to $C^{18}O$, where the opposite would be required to explain low values of $^{13}CO/C^{18}O$. Furthermore, for kinetic temperatures of order $T_{\rm kin} \approx 20$–30 K, consistent with the bulk of the molecular gas in SMGs and ULIRGs (e.g. Dunne et al., 2022), the ^{13}CO reaction would be just as likely in both the forward and backward directions. Again, we argue that ^{13}CO should not be produced preferentially in SMGs or other intensely star-forming galaxies.

Having established that radiative transfer effects and ISM photochemical processes are unlikely to drive $^{13}CO/C^{18}O$ down in SMGs, we turn to stellar nucleosynthesis, as argued by Zhang et al. (2018b). Since ^{18}O is formed primarily in massive stars ($\geq 8\,M_{\odot}$) while ^{13}C is formed mainly as a secondary element in intermediate-mass stars ($\leq 8\,M_{\odot}$), the ratio of these CO isotopologues will naturally be sensitive to the IMF, however the details of the history of the chemical evolution of the ISM is also clearly important and must be taken into consideration. Next, we explore predictions for $^{13}CO/C^{18}O$ using a state-of-the-art chemical evolution model.

4.4.2 Galactic chemical evolution model

Our galactic chemical evolution (GCE) code is described in Kobayashi et al. (2000), hereafter K20, and combining with the latest nucleosynthesis yields it is possible to reproduce the observed elemental abundances in the solar neighbourhood. Fig. 4.3 shows the evolution of [O/Fe] and [C/Fe] ratios in the gas phase, comparing to the observations of stars that were born at various ages and metallicities. The star formation history in the model is constrained from independent observational constraints, namely the metallicity distribution function (see Figure 1 of K20). The K20 model can accurately reproduce the observed [O/Fe]–[Fe/H] relation, although

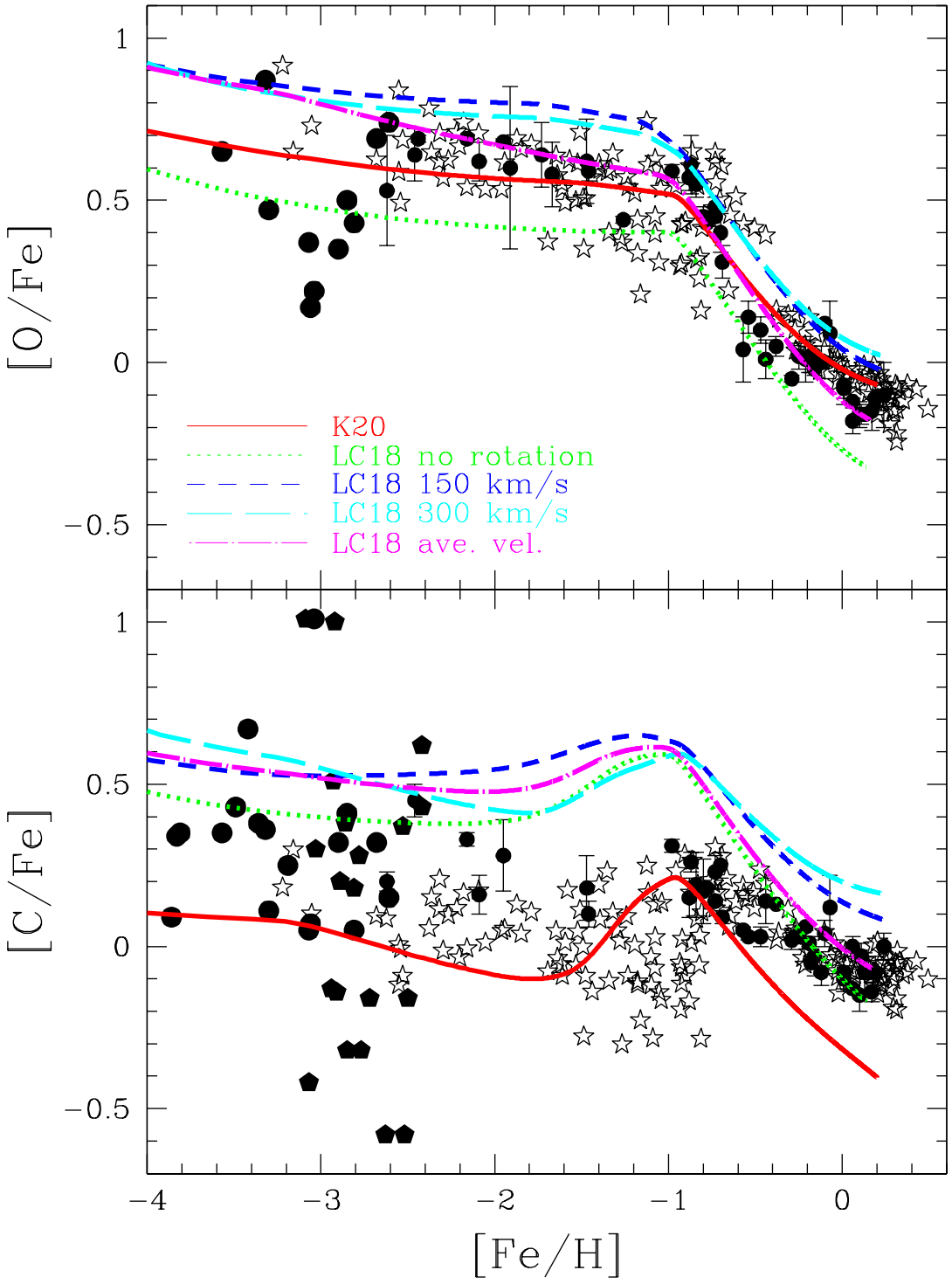

FIGURE 4.3: Evolution of [O/Fe] and [C/Fe] ratios in the solar neighbourhood for the K20 model

Evolution of [O/Fe] and [C/Fe] ratios in the solar neighbourhood for the K20 model (red solid lines), comparing to the models with Limongi and Chieffi (2018)'s yields for no rotation (green dotted lines), rotational velocity of 150 km s^{-1} (blue short-dashed lines), 300 km s^{-1} (cyan long-dashed lines), and the velocity distribution (magenta dot-dashed lines) in Prantzos et al. (2018). The observational data comes from F and G Dwarfs in the solar neighbourhood found in Zhao et al. (2016a). Note the [X/Y] notation corresponds to a log relation [X/Y] $\equiv \log_{10}(X/Y) - \log_{10}(X/Y)_{\odot}$, where X/Y is the ratio of abundances by mass.

[C/Fe] ratios at high metallicities are underproduced in the model, indicating extra production from Wolf–Rayet stars. This model can also reproduce isotopic ratios (see Figure 31 of K20), except for the over-production of ^{17}O from AGB stars (Kobayashi et al., 2011). Fig. 4.4 shows the evolution of isotopic ratios for C and O. The ^{13}C/^{18}O ratio is low at the onset of galaxy formation, and increases via the production of ^{13}C from intermediate-mass stars. Then the ratio gradually decreases as more ^{18}O is produced from more metal-rich, massive stars.

The evolutionary tracks of isotopic ratios can be completely different if the rotation of stars is important. Stellar rotation has been considered in previous works (e.g. Meynet and Maeder, 1997; Hirschi, 2007) but only Limongi and Chieffi (2018) have provided nucleosynthesis yields with their stellar evolution and explosion code for a wide range of parameters including stellar rotation. As shown in previous works (e.g. Kobayashi et al., 2011), elemental abundances and isotopic ratios depend on the assumed stellar rotation. If all stars rotate rapidly (150–300 km s^{-1}), ^{13}C/^{18}O stays low for longer and increases sharply after the formation epoch of the Sun (Romano et al., 2019). This trend can explain the high ^{13}CO/C^{18}O observed in the local ISM at the present day. In this paper, when we consider rotation, we adopt 300 km s^{-1} for all stars, independent of metallicity. Note that constant rotation models over-produce O and C (Figure 4.3). The match to observational data improves if some of the stars do not rotate, namely those at high metallicities (see e.g. Prantzos et al., 2018), but ^{13}C/^{18}O does not then increase as much as observed.

Our GCE code can reproduce the results with no rotation or constant rotational velocity in Romano et al. (2019, their MWG08–10), as well as the velocity distribution in Prantzos et al. (2018). Note that the isotopic ratios are very sensitive to the metallicity of progenitor stars, but the metallicity grid of Limongi and Chieffi (2018) is too coarse. Where Romano et al. (2019) interpolate linearly between contiguous grids, such that the adopted yields are Solar only when the predicted Z is equal to $Z_\odot$, we instead adopt Solar metallicity yields at $Z \geq 0.004$ and extrapolate them at $Z > Z_\odot$. This problem was not apparent in Romano et al. (2019), which is likely because they used the Talbot and Arnett (1973) and Portinari et al. (1998) production matrix to scale the yields with metallicity where the grids provided by full computations are missing. This matrix is valid for secondary element such as ^{14}N, but probably not for primary production of ^{13}C, ^{14}N and ^{18}O in the case with rotation.

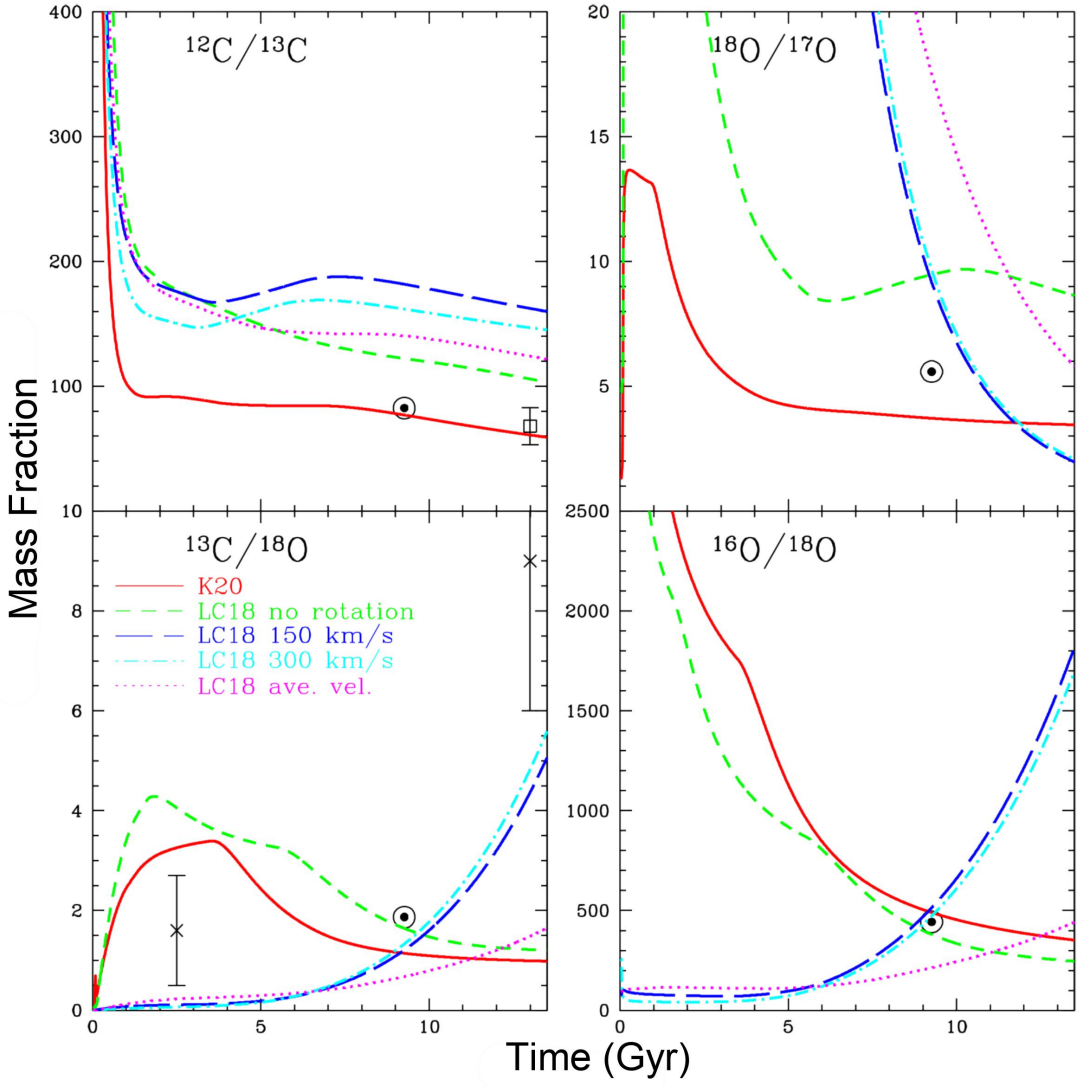

FIGURE 4.4: Evolution of C and O isotopic ratios in the solar neighbourhood for the K20 model

The same as Fig. 4.3, but for C and O isotopic ratios. Observational data are the solar ratios from Asplund et al. (2009) and the measurements in the local ISM (see Romano et al. 2019 for the data) and 9io9 (cross).

4.4.3 Chemical evolution scenarios for 9io9

We now compare our observational results to the predictions of the K20 model, for several different scenarios. As described above, the model predicts the time evolution of the abundances of isotopes (e.g. ^{12}C, ^{13}C, ^{16}O and ^{18}O) in a system that is instantaneously mixed, with a given star-formation history and assumed IMF, and where chemical enrichment is from stars across a wide range of stellar mass, including asymptotic giant branch (AGB) stars, super-AGB stars, core-collapse supernovae and Wolf-Rayet stars.

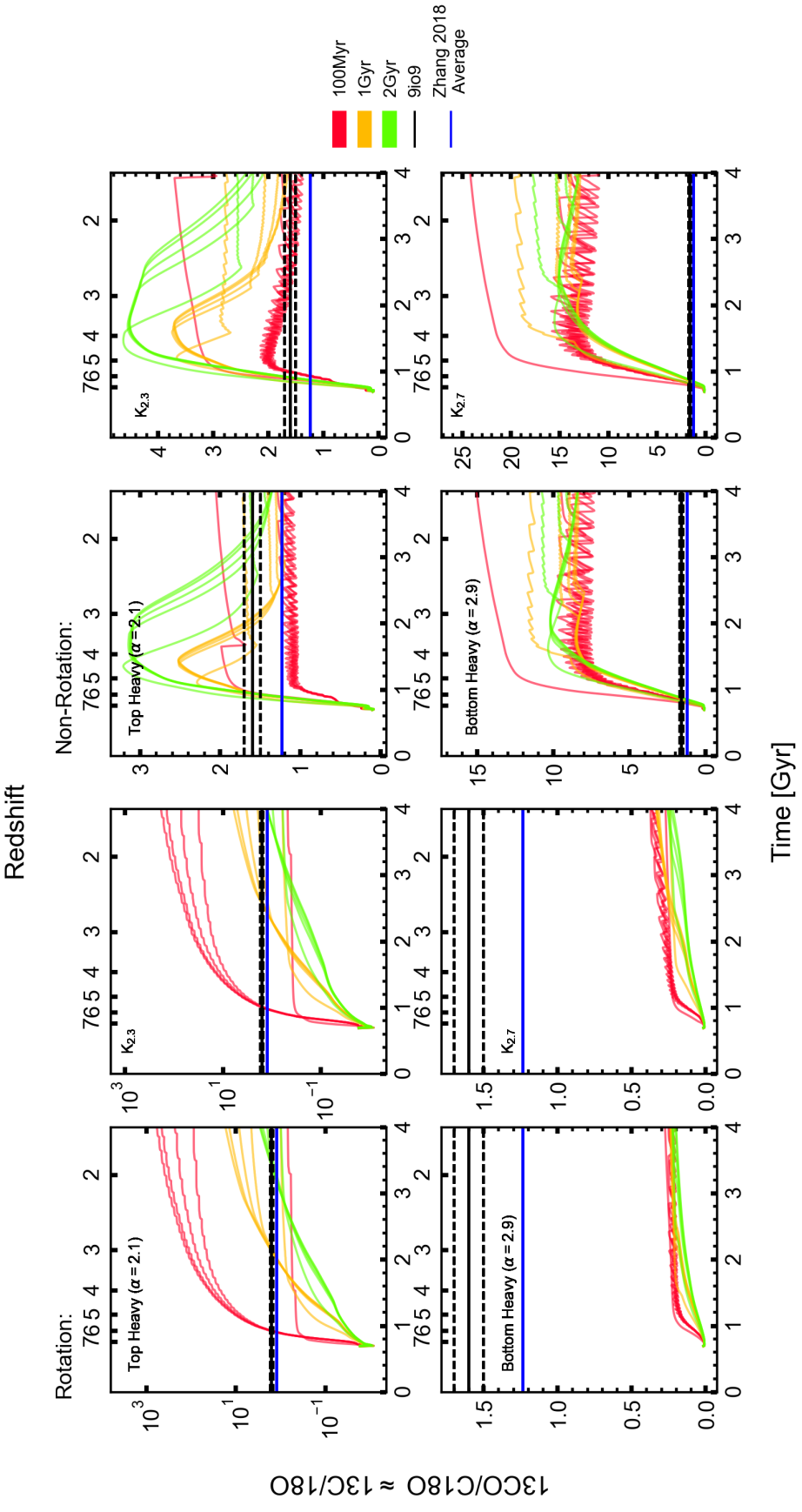

FIGURE 4.5: C and O Mass ratio for a variety of IMFs and SFHs

$^{13}CO/C^{18}O$ mass ratios for a variety of IMFs and star-formation histories across our 108 chemical evolution models (in each panel). Each line colour corresponds to a different star formation timescale (0.1, 1, and 2 Gyrs). The black line corresponds to the observed ratio in 9io9, with the dotted black lines being the 1σ range and the blue line being the average value found for SMGs in Zhang et al. (2018b).

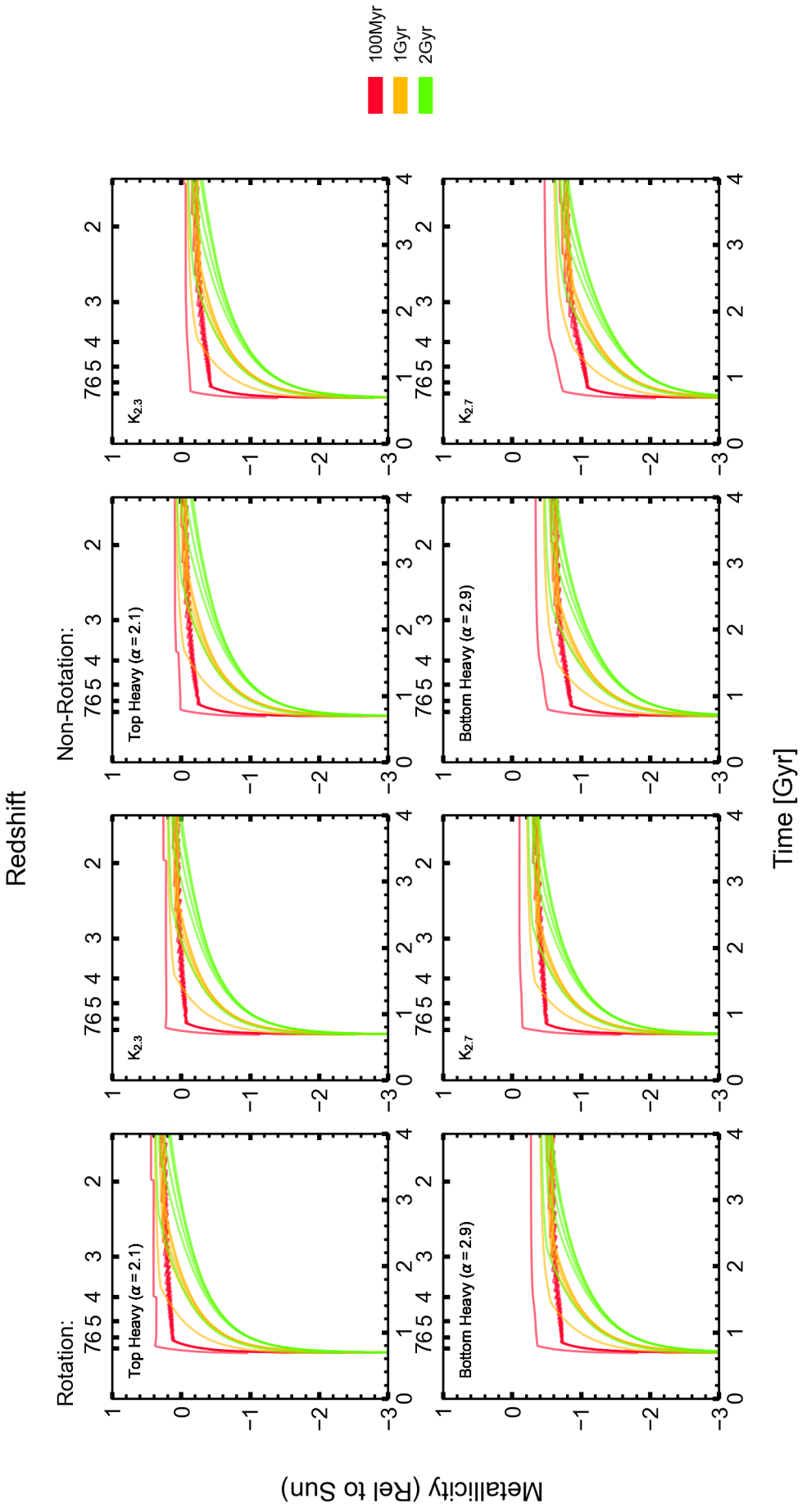

FIGURE 4.6: Metallicity evolution for a variety of IMFs and star-formation histories

Metallicity evolution for a variety of IMFs and star-formation histories across our chemical evolution models (in each panel).

Our fiducial model assumes a Kroupa ($K_{2.3}$) IMF (Kroupa et al., 1993; Kroupa, 2001, 2008) with a three-part power-law function, where $\alpha_0 = 0.3$ at $0.01 \leq M/\mathrm{M}_\odot < 0.08$, $\alpha_1 = 1.3$ at $0.08 \leq M/\mathrm{M}_\odot < 0.5$ and $\alpha_2 = 2.3$ at $0.5 \leq M/\mathrm{M}_\odot \leq 120$, as in Kobayashi et al. (2020). For the Solar neighbourhood, this model can reproduce the results of Romano et al. (2019) if we use the same yields and IMF. We find that $\alpha_2 = 2.3$ gives a better match to the observed elemental abundances than $\alpha_2 = 2.7$, where $\alpha_2 = 2.7$, noting that Romano et al. (2017, 2019) used $\alpha_2 = 2.7$ at $1 \leq M/\mathrm{M}_\odot < 100$ which results in different metallicities and elemental abundance ratios, even with the same star formation history. Furthermore, $\alpha_2 = 2.3$ agrees with the observations of individual stars in the Solar neighbourhood for most of elements (except for Ti) with the K20 yields.

For AGB and super-AGB stars, the nucleosynthesis yields are taken from K20. For pre-supernova and core-collapse supernovae, yields are taken from Limongi and Chieffi (2018) (set 'R'), so that we can test the impact of stellar rotation. For the relevant isotopes, half of the ^{12}C is produced by low-mass stars (1–4 $\mathrm{M}_\odot$) and the rest from massive stars ($M > 10\,\mathrm{M}_\odot$). ^{13}C is synthesised by proton-capture at high temperature in intermediate-mass stars (4–7 $\mathrm{M}_\odot$, hot bottom burning) and massive stars, together with ^{14}N. ^{16}O is mainly produced during hydrostatic burning in massive stars and is ejected via supernovae, while ^{18}O is synthesised by helium burning in massive stars, depending on the metallicity and rotation (Kobayashi et al., 2011). In this paper, the rotational velocity is set to $300\,\mathrm{km\,s^{-1}}$ at 13–120 $\mathrm{M}_\odot$.

For our Solar neighborhood fiducial model, with a star-formation timescale of 4.7 Gyr and infall timescale of 5 Gyr (see Kobayashi et al. 2000 for a detailed definition of the model parameters; cf. 1 and 7 Gyr, respectively, in Romano et al. 2017, 2019), the isotopic mass [number] ratios 4.57 Gyr ago are: $^{12}\mathrm{C}/^{13}\mathrm{C} = 163$ [150], $^{16}\mathrm{O}/^{17}\mathrm{O} = 4,644$ [4,371], which are slightly higher than the Solar ratios ($^{12}\mathrm{C}_\odot/^{13}\mathrm{C}_\odot = 90$ [83] and $^{16}\mathrm{O}_\odot/^{17}\mathrm{O}_\odot = 2,632$ [2,477]), but $^{16}\mathrm{O}/^{18}\mathrm{O} = 419$ [372] and $^{13}\mathrm{C}/^{18}\mathrm{O} = 1.16$ [0.84] are in good agreement with the Solar ratios ($^{16}\mathrm{O}_\odot/^{18}\mathrm{O}_\odot = 496$ [443], $^{13}\mathrm{C}_\odot/^{18}\mathrm{O}_\odot = 2.59$ [1.87], Asplund et al. 2009). The Solar neighbourhood K20 model also predicts a very similar ratio of $^{13}\mathrm{C}/^{18}\mathrm{O} = 1.14$, but predicts lower ratios of $^{12}\mathrm{C}/^{13}\mathrm{C}$ and $^{16}\mathrm{O}/^{17}\mathrm{O}$ due to the lack of contributions from stars with $M > 50\,\mathrm{M}_\odot$ and stellar rotation. Note that for the yields taken from Nomoto et al. (2013), Romano et al. (2017) extrapolated[1] over $40 < M/\mathrm{M}_\odot < 100$, which is not physically correct, whilst less than per cent of the total mass is locked into such stars their metal contribution is significantly larger. ^{17}O yields

[1]Nomoto et al. (2013) do not provide stellar yields for masses larger than 40 $\mathrm{M}_\odot$, whereas Limongi and Chieffi (2018) compute yields up to 120 $\mathrm{M}_\odot$.

were set artificially to zero across $1 < M/\mathrm{M}_{\odot} < 6$ in Romano et al. (2017), which was fixed in Romano et al. (2019), see Romano et al. (2020).

Having established this baseline, we construct a set of chemical evolution models for 9io9. This galaxy has a gas fraction likely exceeding 50 per cent and a SFR, regardless of the assumed IMF, of order $1000\,\mathrm{M}_{\odot}\mathrm{yr}^{-1}$. We do not have useful constraints on its star formation history, given the lack of adequate photometry across the UV-optical-IR (exacerbated by its highly dust attenuated SED). A secure redshift is measured from emission lines, and we postulate that the galaxy cannot be much older than 2 Gyr. We assume 9io9 formed at $z = 7$ and consider a star formation model that can be characterised by two time scales: τ_{s}, (equivalent to the inverse of the efficiency) of exponentially declining star formation, and τ_{i}, of exponential infall of pristine gas. We assume that the star formation history of 9io9 is characterised by an initial burst during which a significant fraction of the stars are formed, followed by intermittent star formation such that star formation stops when the (cold) gas fraction falls below 50 per cent and re-starts when the gas fraction exceeds 50 per cent due to stellar mass loss or any late-phase gas accretion. We consider two model sets, with stellar rotation and no stellar rotation, respectively. Each model set is comprised of 108 star formation histories covering a mesh grid of $\tau_{\mathrm{s}} = 0.1, 1, 2\,\mathrm{Gyr}$, for infall models with $\tau_{\mathrm{i}} = 1, 2, 5, 10\,\mathrm{Gyr}$ or closed-box models (with an initial gas fraction of unity). We also vary the high-mass IMF slope from $\alpha_2 = 2.1$ (top heavy), 2.3, 2.7 and 2.9 (bottom heavy), and also explore very slow star-formation models with $\tau_{\mathrm{s}} = \tau_{\mathrm{i}} = 20\,\mathrm{Gyr}$ and 50 Gyr for the four IMFs under consideration. Clearly this is rather an exhaustive grid; only a sub-set of models likely correspond to 9io9 and galaxies like it. However, in this work we aim to illustrate the sensitivity of the prediction of ^{13}CO/C^{18}O for a fixed GCE model, not only varying the IMF but also the impact of stellar rotation and star formation history. Fig. 4.5 compares the predicted ^{13}CO/C^{18}O as a function of cosmic time for the different models. Note the different y-axis ranges in each panel.

Let us first consider the models with bottom heavy $\alpha_2 = 2.9$ slopes. When stellar rotation is included, ^{13}CO/C^{18}O is less than 0.3 for all star formation histories, with ^{13}CO/C^{18}O increasing for shorter τ_s, and all inconsistent with the observations. Without stellar rotation, the same IMF predicts high ^{13}CO/C^{18}O for all star formation histories, with ^{13}CO/C^{18}O above 7 within about 1 Gyr of formation, albeit with a larger spread in ^{13}CO/C^{18}O at late times.

For $\alpha_2 = 2.7$ – i.e. slightly less bottom heavy, and potentially close to Galactic (see below) – we see a similar picture. In the rotating model ^{13}CO/C^{18}O stays low ($<$0.5) for all star formation

histories, with an identical trend with τ_s. When rotation is included, ^{13}CO/C^{18}O is even more extreme, with ^{13}CO/C^{18}O exceeding 10 for all star formation histories after 1 Gyr. We conclude that the observations are inconsistent with an IMF of slope $\alpha_2 \gtrsim 2.7$; the observed ^{13}CO/C^{18}O is hard to reproduce regardless of the presence of stellar rotation and considering a broad family of star formation histories.

For $\alpha_2 \lesssim 2.3$ – i.e. towards top heavy – we can see that the stellar rotation models produce ^{13}CO/C^{18}O of order unity within a few Gyr for star formation histories with $100\,\mathrm{Myr} \lesssim \tau_s \lesssim 1\,\mathrm{Gyr}$. As τ_s increases, ^{13}CO/C^{18}O is suppressed at later times. The situation is reversed in the non-rotating model, with ^{13}CO/C^{18}O rapidly increasing (exceeding unity, but not evolving to the extreme ^{13}CO/C^{18}O seen in the rotating models) after formation for high values of τ_s. However, again for $100\,\mathrm{Myr} \lesssim \tau_s \lesssim 1\,\mathrm{Gyr}$ these non-rotating models can re-produce the observed ^{13}CO/C^{18}O on realistic time scales, even though the detailed evolution of ^{13}CO/C^{18}O is different to the rotating model. We can conclude that our GCE can reproduce the observed ^{13}CO/C^{18}O of 9io9 with IMFs with slopes $\alpha_2 \lesssim 2.3$ favoured. Bottom-heavy IMFs ($\alpha_2 > 2.3$) cannot produce the observed ^{13}CO/C^{18}O regardless of star formation history or the presence of rotating stars.

Also note how the inclusion of rotation has a significant effect on the ratios, primarily by *inverting* the IMF—CO ratio relation. This is due to the production of ^{13}C no longer being limited to intermediate-mass stars, with a separate production route also being present in the more massive Wolf-Rayet population.

There are a few reasons both direct and indirect, as to why stellar rotation has such a significant effect on the resultant stellar yields. Stellar rotation causes mixing within stellar layers, this has the effect of bringing different nuclear species into contact with each other, where in the absence of rotation they would have remained well separated. Other effects of stellar rotation is that it alters the size of the various convective regions within a star, as well as its surface properties. This alters the future evolution of the star, with the latter causing more significantly more mass loss than would be expected in the non rotation case, thus changing the conditions in which the nucleosynthesis is occurring (Prantzos et al., 2018).

An important diagnostic tool tool to further differentiate the models comes from their metallicities. Figure 4.6, shows the metallicity evolution for each of our models. As one would expect, the more top heavy IMFs due to their higher fraction of massive stars produce higher metallicities. What can also be seen is significant variation in the metallicity tracks based on the star formation history and unlike the case of the C/O ratio, there is no inversion of the relation when

moving between the rotation and non-rotation model sets. The effects of stellar rotation in the case of metallicity are more subtle, with the rotation model sets resulting in a higher metallicity than those without, given the same SFH and IMF. This effect is less pronounced than the variation in metallicity from the variation in star formation history and τ_s, and thus a measure of the metallicity in combination with the C/O ratio could be used in combination with the CO isotopologues to provide further constraints on the range of acceptable models.

4.5 Conclusions

In debates around the possibility of non-universal IMFs, we usually refer to the Galactic IMF, with terms like 'top heavy' and 'bottom heavy' relative to this reference. But what is the 'canonical' Milky Way-like IMF? In Zhang et al. (2018b), this is assumed to have a Kroupa form with high-mass slope of $\alpha_2 = 2.7$ (Kroupa et al., 1993). However, (Kroupa, 2001) argue for the heavier $\alpha_2 = 2.3$. This discrepancy is due to different methods of constraining the IMF within the Milky Way, with some authors arguing that a high-mass slope $\alpha_2 > 2.3$ is required to explain the local field star IMF and chemical abundances (Scalo, 1986; Kroupa et al., 1993; Mor et al., 2017; Jeřábková et al., 2018) while other approaches argue for a high-mass slope of $\alpha_2 = 2.3$ (Salpeter, 1955; Kroupa, 2001; Chabrier, 2003). Therefore we should conclude that, in the context of the discussion above, the IMF in 9io9 – a galaxy with a star formation rate up to three orders of magnitude greater that the Milky Way – is consistent with a Galactic IMF only if the latter is best represented by $\alpha_2 \approx 2.3$ (Kroupa, 2001). Generally, IMFs more top heavier than this are favoured, consistent with the conclusions of Zhang et al. (2018b).

Perhaps the most important conclusion we can draw from this study is the sensitivity of the predicted ^{13}CO/C^{18}O ratio on the chemical evolution model. Figure 4.5 clearly illustrates the profound impact the presence of rotating stars has for example: the differences in the evolutionary tract of ^{13}CO/C^{18}O for any given IMF is inverted when compared to the models without, with the more top-heavy IMFs giving a higher predicted ratio. IMFs, where $\alpha_2 \geq 2.3$, also no longer show a well constrained predicted ratio, but instead vary by orders of magnitude, with strong sensitivity to the SFH and star formation timescales. The more bottom-heavy IMFs $\alpha_2 \leq 2.7$, on the other hand remain tightly constrained but the resultant ratio is approximately two orders of magnitude below that of the non-rotating case. This difference exceeds the effect

of IMF variation in the non-rotating case. The importance of stellar rotation on the ultimate enrichment within galaxies such as 9io9, could limit the ability to derive conclusions with respect to the IMF based off of CO isotopologues.

Chapter 5

Ongoing and Future Work

With a wealth of observatories covering much of the electromagnetic spectrum now online, it is a golden age for astronomical data. In this section I will discuss some ongoing and future work that can be done to help us better understand dusty star forming galaxies, with the main focus being on 9io9, however much of this discussion can also be extended to other sources.

5.1 Ongoing Work: Spectral Scan of 9io9

As previously mentioned in Chapter 3 and 4, the observations described were collected as part of a spectral scan. This spectral scan offered a wealth of data and molecular transitions, which during the course of this thesis have yet to be explored. As such a brief discussion and outline of the preliminary work on these and what they can tell us about 9io9 are warranted.

5.1.1 Water Lines

Water is one of the most abundant molecules and has some of the brightest emission lines in the sub-mm bands, it owes this fact to containing two of the most common interstellar elements in Hydrogen and Oxygen. Sub-mm wavelengths contain a plethora of water lines both para- and ortho- types, being observed in both emission and absorption. We have detected both the 557 GHz ground state o-H_2O emission and its isotopologue o-$H_2^{18}O$ at 548 GHz. This line is often observed in both emission and absorption, in the case of 9io9 we do not observe any clear absorption with the line profile being consistent with the double horned profile of the CO

emission as well as other lines detected within this system (Geach et al., 2018; Harrington et al., 2019).

Work by Liu et al. (2017) detected the ground state o-H_2O emission for a sample of star-forming galaxies, with this sample they found a linear trend between the luminosity of the line and the FIR luminosity (with a slope of $N = 1.11 \pm 0.21$), 9io9 an intrinsic HyLIRG ($L_{IR} \geq 10^{13} L_{\odot}$), provides the brightest IR galaxy to contain a 557 GHz detection and potentially the first detection of this transition in the high-z universe. Does 9io9 lay on the expected relation? Or is there evidence of deviation from this relation? Whilst a proper analysis of the line is yet to be done we tentatively find a line luminosity for the water line to be $\mu L_{H_2O} = 7.26 \times 10^{11}$K km s^{-1}pc^2, where μ is the magnification factor. With a already well constrained lens model we will be able to de-lens the flux to the source plane to obtain a source plane luminosity.

5.1.2 Dense gas tracers: HNC and CN

To gain a full picture of the molecular gas within 9io9 requires observing a wide range of different tracers probing the gas across a range of density ranges and temperatures. Being amongst the brightest emission lines in the mm/sub-mm range CO transitions are typically observed, due to the extreme brightness of 9io9 we can go beyond this and start probing a variety of other species tracing the dense gas.

With clear detections of both the HNC(6-5) and CN(5-4) emission lines and the lower J-transitions HNC(5-4) and CN(4-3) detected in a previous ALMA cycle (Geach et al., 2018), we can now start constraining the conditions of the dense gas within 9io9. These species were first detected in the high-z universe in Guélin et al. (2007) where the blended HNC(5-4) and CN(4-3) were detected, after decomposition they found that the HNC was the dominant emission with a luminosity ratio of approximately 2, though the CN was only tentatively detected. Other detections of these lines by Béthermin et al. (2018) and Cañameras et al. (2021) find a dominant HNC component consistent with Guélin et al. (2007). Geach et al. (2018) using the source plane reconstruction of the the same blended lines for 9io9, found that the CN emission dominated but with significant redshift dependence on this.

Now with clear detections of the non blended higher transitions, we can now break this redshift degeneracy. As can be seen in figure 5.2 each of the lines detected have the clear double horned profile, similar to the CO emission, as such we can use the high S/N CO $J(5\rightarrow4)$ transition as

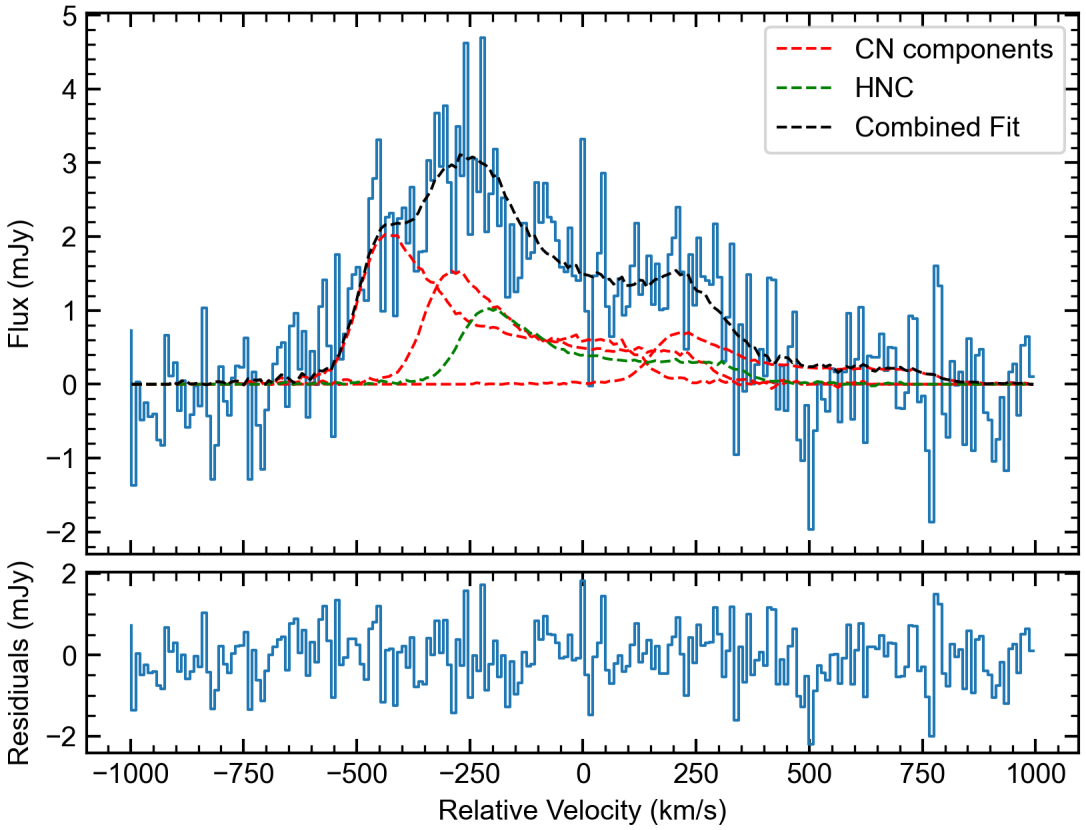

FIGURE 5.1: Image plane deblending of CN(4–3) and HNC(5–4)
The image plane emission of the blended CN and HNC emission first presented in Geach et al. (2018), using the High S/N CO $J(5\rightarrow4)$ transition as a model to decompose the lines. The lower panel is the resulting residuals from the decomposition.

an empirical template to decompose the CN/HNC emission. As we are using this empirical template the redshift assumption is not required (though we do assume all the lines lie at the same redshift) as the template is shifted by the ratio of the frequency of CO $J(5\rightarrow4)$ to target line frequency, thus breaking the redshift degeneracy noted in Geach et al. (2018), by varying the normalisation of this template for each of the lines independently we can determine best fit for the contribution for each of the resulting lines. To determine the 1σ uncertainty on these fits we add gaussian noise to each frequency channel determined by off source regions of the datacube and scaled to match the subtending region. Doing this for 1000 realisations we obtain robust uncertainties for each of the corresponding fits. As can be seen in Figure 5.1, the resulting fit provides a good match to the observed line profile. Surprisingly the third CN component is $\sim 5\times$ the expected theoretical value, with Geach et al. (2018) interpreting this excess as a potential outflow, however as seen in Figure 5.1 the location of this excess matches the expected location of the third hyperfine structure emission peak.

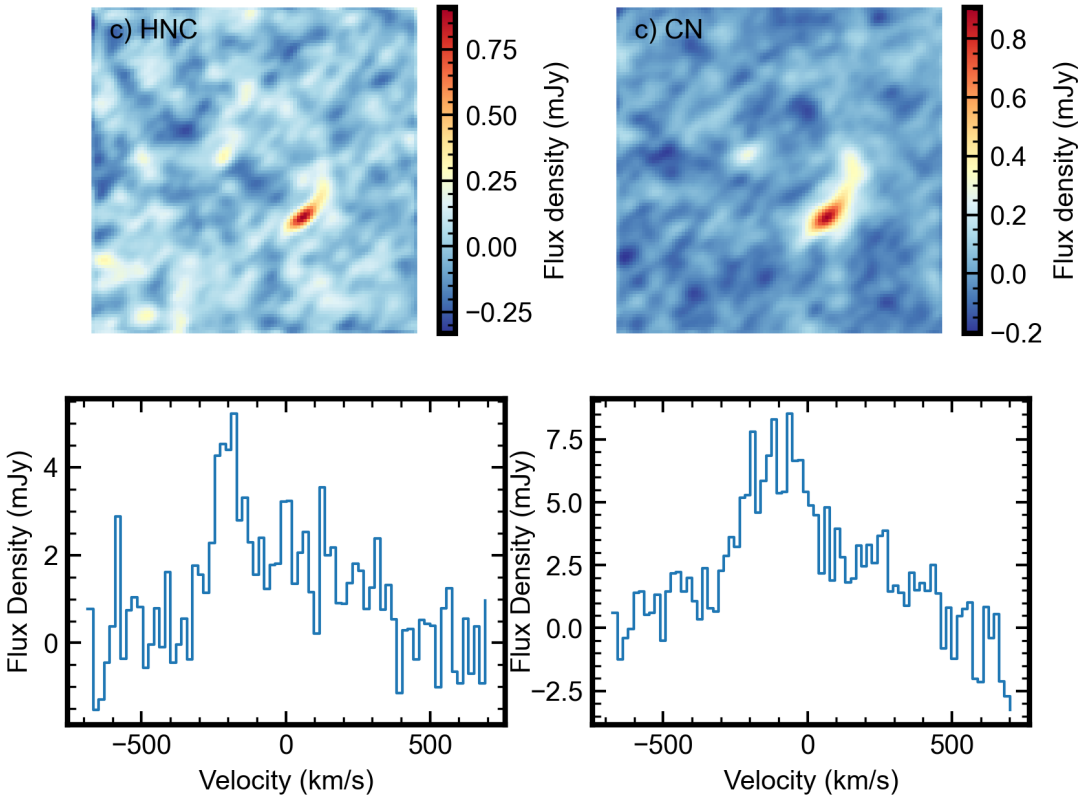

FIGURE 5.2: Image plane emission of CN(5–4) and HNC(6–5)

Now with detections of a couple transitions for both species we can start to try and model the conditions of the dense gas within 9io9. To do this we would use the program RADEX Tak et al. (2007) via the python package ndradex, and this is work in progress.

5.1.3 N_2H+

The final transition of interest in this spectral scan is what we have tentatively identified as N_2H+(5-4) (This feature can be seen in 4.1). N_2H+ is a tracer of the cosmic ray ionisation in UV opaque and even X-ray opaque regions, and being an ion of similar structure, chemical origin and excitation conditions is thought to originate in similar regions and trace similar structures to the more commonly detected HCO+ (Ceccarelli et al., 2014; Gaches et al., 2019).

Cosmic rays heat the gas within galaxies and are a driver of interstellar chemistry (Dalgarno, 2006), so constraining their importance within a galaxy could have important implications on our understanding of the conditions and chemistry present in high-z star forming systems in comparison to local analogues.

5.2 Future Work

5.2.1 ALMA: High Resolution Imaging

On top of existing data to constrain conditions, a natural next step for work on 9io9 would be to obtain higher resolution observations. Due to its lensed nature it provides a perfect opportunity to study high-z star formation on scales otherwise unobtainable. Our previous observations have been limited to approximately 300mas, corresponding to around 300pc in the source plane, by further increasing this to around 50mas, which is in reach of ALMA, would allow us to probe the conditions and star formation on scales comparable to that of giant molecular clouds (GMCs) within 9io9. Setting up the observations such that important tracers of the ISM lay within the observations, could allow us to both the dust and gas on these scales and below (combined with previous observations) are a few of the questions that this sort of observations could help us address, including the CI (2→1) and CO J(7→6) in our set-up:

- **Dust morphology at the scale of star formation:** Measure the thermal dust emission to high significance probing the structure of the gas disk and star formation down to scales of 100 pc in the source plane, approaching the scales of GMCs. *Is there evidence of clumps?, or is star formation smoothly distributed at 100 pc scales?*
- **Resolving molecular disk structure:** Map both the CO J(7→6) and CI (2→1) emission across 9io9 to the same resolution as the dust. This would allow us to probe the distribution of both the star forming gas and the total molecular gas within 9io9, map any variation between the dust continuum and molecular gas across the source, as well as better constrain the kinematic model and be able to measure the Toomre Q parameter across the source to probe the level of disk instability. *What is the level of dynamical instability in the gas-rich disk?; Is there evidence of minor mergers driving activity?*
- **Lensing halo sub-structure:** The high-resolution data would also allow us to probe the sub-structure of the foreground lens galaxies in greater detail, as the lensing substructure leaves imprints on the shape and structure of the lens itself. Via sophisticated lens modelling coupled with high resolution data we can tease out this structure. *What is the distribution of the dark matter sub-structure in the lensing halo?*

- **Mapping Kinetic temperature and gas mass:** In combination with the previously detected C I (1–0) (at a resolution of $\sim$ 300mas) we would be able to map the kinetic temperature of the emitting gas on scales of $\sim$ 300pc, allowing us to probe both the conditions and distribution of the total molecular gas reservoir across 9io9. *Is there significant variation in the gas conditions across 9io9; Is the central AGN heating the gas in the galactic centre?*

5.2.2 James Webb Space Telescope

With the advent of the James Webb Space Telescope (JWST), which launched on Christmas Day 2021, has allowed the most sensitive observations of the sky in the infrared. With its resolution and sensitivity, JWST allows previous tracers and diagnostics to be explored on scales previously unobtainable for sources at high-z. Here I will briefly discuss a potential avenue for research in furthering our understanding of 9io9.

5.2.2.1 Mid-Infrared Instrument

One such avenue of research, would utilise the mid-infrared instrument (MIRI) on JWST. MIRI covers the wavelength range $5-28\mu$m, which at 9io9's redshift ($z=2.56$) covers many polycyclic aromatic hydrocarbons (PAH) transition features. Many of these PAH features have been shown to be good diagnostics of AGN activity within sources, with signatures from AGN dominated regions, and that of star formation dominated regions can be easily differentiated based off the lines equivalent widths. (Imanishi et al., 2010; Yamada et al., 2013; Inami et al., 2018).

Recent work on a lensed SMG presented in Spilker et al. (2023) looked at the 3.3μm PAH feature, which depending on its equivalent width can classify sources into Star-forming dominated or AGN dominated. In this work they found an equivalent width of 125 ± 15nm far larger than that expected for AGN dominated emission and thus supporting the conclusion that much of the emission in this source is dominated by star formation.

For 9io9 in which there is some tentative evidence of AGN activity from the blended dense gas tracers, CN and HNC (Geach et al., 2018), as well as the high radio-LIR ratio, which was found to be higher than that expected from pure star formation. This technique would be invaluable in helping confirm/disconfirm the influence of this AGN and its importance in future interpretations of the FIR emission and diagnostics.

5.2.3 Building up a sample

The spectral scan of 9io9 as mentioned detected a wealth of species, that can be seen in figure 4.2. The main goals of my research plan would be to obtain spectral scans targeting the same restframe frequencies. The restframe frequency range which is between approximately $540-580$GHz has remained relatively unexplored due to the atmosphere being opaque to these frequencies, thus local exploration has been limited to space observatories such as the Herschel and Odin satellites, both of which are now offline. Due to SMGs laying at redshifts > 1, these frequencies have been redshifted into regions of the atmosphere which are more transparent and within reach of observatories such as ALMA. This provides a rare opportunity in which high-z studies can provide insights beyond that of local studies.

Fortuitously the spectral range of interest has also covered in the spectral stack of 22 SMGs first published in Spilker et al. (2014), with the final complete stack containing 78 sources presented in Reuter et al. (2023). Whilst all the sources did not cover the whole range of the stack ≈ 30 sources were included over the region of interest between $\nu_{rest} = 540-580$GHz. This allows it to be compared directly with the 9io9 spectra and as such provide a reference frame for which lines could be of interest in follow-up targeting. Figure 4 in Reuter et al. (2023) shows the result of their stack, by comparison to 9io9 it can be seen that there are significant differences in the result of the stack and our observed spectra. Whilst spectral stacks have great utility there are complications in interpreting various line strengths and line ratios, due to a wide range of sources of different SFR and evolutionary histories being included, which could have a spread of line ratios involved. As such are not a perfect replacement for high sensitivity observations of a range of sources, to examine the rich diversity of galaxy populations. Due to the intrinsic faintness of the lines of interest($> 10\%$ the neighbouring CO(5-4)), their study is limited to a small sample of the SMG population, namely lensed sources. By utilizing gravitational lensing, these transitions are detectable with ALMA with a few hours of integration time per source, instead of a few days in the unlensed case. Table 5.1 gives the preliminary sample of targets of interest, four of which come from the SPT sample (Vieira et al. 2013) with the final being that of SDP.81 one of the most studied SMGs in the literature. These sources cover a range of redshifts and intrinsic IR luminosities.

Source:	SPT0125-47	SPT0551-50	SDP.81	SPT0103-45	SPT0125-50
z	2.5148	3.1641	3.042	3.0917	3.9593
L_{IR} ($10^{12}L_{\odot}$)	9.63	10.02	3.1	6.19	3.92
Magnification	18.9	6.3	17	14.4	26.7
ALMA Band	5	4	4	4	3

TABLE 5.1: Information on the preliminary sample of sources, including what ALMA band the observations would lay in.

5.3 Concluding Remarks

Over the past century since the first discovery of external galaxies, our understanding of galaxy formation and evolution has come a long way. We have broadened our view from the optical to cover the whole range of the electromagnetic spectrum and now beyond into the age of multi-messenger astronomy. What has become clear is that there exists huge diversity in the population of galaxies both in the local universe and through cosmic time, to truly understand the physical processes which drive the formation and evolution of galaxies requires a diverse approach both using large samples of galaxies, probing the statistical properties of various galaxy groups, and that of more in depth studies of a smaller number, trying to understand the specific evolutionary path and conditions which led to specific galaxies outcomes.

How does 9io9 and the work presented in this thesis fit into this ever growing picture of galaxy evolution, both amongst ULIRGs/HyLIRGs and that of the more general galaxy population?

Chapter 2 focuses on the ionised ISM, up til now few studies on SMGs have focused on the density of this important component, through tracers such as the [N II] doublet. We found that the ionised ISM, just like the molecular ISM is significantly denser than that of normal star forming galaxies such as our Milky Way, with a derived density approximately an order of magnitude above and consistent with that of a galactic star formation region. In chapter 3, we again found similarity between that of galactic star forming regions and that of the integrated values found within 9io9, this similarity found via the ground state Ammonia transition, likely traces some of the densest gas within galaxies. These similarities between that of star forming regions within the Milky Way and that of the most prolific star forming galaxies could show that much of the star formation occurring in galaxies like ULIRGs is not that different form that of other galaxies, but that they are able to sustain this star formation across much of their extent.

In recent years the CO isotopologues ^{13}CO and C^{18}O, have been argued to provide evidence that in extreme starbursts such as 9io9 and more generally the ULIRG population, must be top

heavy. This result would have far reaching implications, due to the centrality of the IMF in deriving many important galactic properties such as stellar masses and Star formation rates. Evidence of IMF variation, would lead to more suble effects on galaxies as well, for example by changing the expected supernova rates and thus the efficiency of stellar feedback, or the level of enrichment with heavier elements in galaxies. Even if the evidence first arises in extreme systems such as 9io9 it opens up a range of questions for the wider galaxy populaton, If the IMF varies, by how much does it vary? Does it vary by galaxy type? does it vary within galaxies?. In Chapter 4 by using a range of star formation histories, IMFs, and the effects of stellar rotation to probe the resultant ratio we found that the importance of stellar rotation can not be ignored, and has a huge effect on the result. In the cases of $\alpha_2 = 2.7$ and $\alpha_2 = 2.9$ the effect of stellar rotation has a larger effect on the ratio than that of varying the IMF in the non-rotation case. For $\alpha_2 = 2.3$ and $\alpha_2 = 2.1$, stellar rotation causes the ratio to be sensitive to the star formation histories, varying by orders of magnitude between models. If stellar rotation is important this could have strong implications on whether CO isotopologues could be useful in constraining the IMF. However we also found that in both the case of stellar rotation and without the most commonly adopted IMF in deriving galaxy properties can reproduce the low ratio observed in the wider ULIRG population in some of the models, such that if the ratio is indeed a probe of othe IMF it does not provide reason strong reasons to revise our galactic properties for the most extreme star forming environments.

The overall picture found within this thesis is that even in galaxies that are far from that of our own, the differences between them could just be due to scale with the ULIRG/SMG populations having conditions similar to regions found within our own galaxy but across much of its extent. Whilst many questions surrounding galaxy formation and evolution remain unanswered, over the past 25 years since the discovery of SMGs, much has been learnt about this special class of galaxies. With JWST, ALMA, and a host of other observatories now operating or set to come online in the coming years spanning much of the EM spectrum, the coming decades will almost certainly be a fruitful time in furthering our understanding of SMGs and galaxies more generally.

Bibliography

Akrami, Y., Ashdown, M., Aumont, J., et al., 2020. Planck 2018 results - IV. Diffuse component separation. *Astronomy & Astrophysics*, 641:A4. Publisher: EDP Sciences.

Asada, H., 1997. Critical Lines in Gravitational Lenses and the Determination of Cosmological Parameters. *The Astrophysical Journal*, 485:460. ADS Bibcode: 1997ApJ...485..460A.

Asplund, M., Grevesse, N., Sauval, A.J., et al., 2009. The Chemical Composition of the Sun. *Annual Review of Astronomy and Astrophysics*, 47:481.

Barger, A.J., Cowie, L.L., Chen, C.C., et al., 2014. IS THERE A MAXIMUM STAR FORMATION RATE IN HIGH-REDSHIFT GALAXIES?, , ,. *The Astrophysical Journal*, 784(1):9.

Barger, A.J., Cowie, L.L., Sanders, D.B., et al., 1998. Submillimetre-wavelength detection of dusty star-forming galaxies at high redshift. *Nature*, 394:248.

Bate, M.R., 2009. The importance of radiative feedback for the stellar initial mass function. *Monthly Notices of the Royal Astronomical Society*, 392(4):1363.

Baugh, C.M., Lacey, C.G., Frenk, C.S., et al., 2005. Can the faint submillimetre galaxies be explained in the cold dark matter model? *Monthly Notices of the Royal Astronomical Society*, 356:1191. ADS Bibcode: 2005MNRAS.356.1191B.

Benson, A.J., 2010. Galaxy formation theory. *Physics Reports*, 495(2):33.

Benson, A.J., Bower, R.G., Frenk, C.S., et al., 2003. What Shapes the Luminosity Function of Galaxies? *The Astrophysical Journal*, 599:38. ADS Bibcode: 2003ApJ...599...38B.

Bigiel, F., Leroy, A.K., Jiménez-Donaire, M.J., et al., 2016. The EMPIRE Survey: Systematic Variations in the Dense Gas Fraction and Star Formation Efficiency from Full-disk Mapping of M51. *The Astrophysical Journal*, 822:L26. ADS Bibcode: 2016ApJ...822L..26B.

Bisbas, T.G., Dishoeck, E.F.v., Papadopoulos, P.P., et al., 2017. Cosmic-ray Induced Destruction of CO in Star-forming Galaxies. *The Astrophysical Journal*, 839(2):90. Publisher: The American Astronomical Society.

Bisbas, T.G., Papadopoulos, P.P., and Viti, S., 2015. EFFECTIVE DESTRUCTION OF CO BY COSMIC RAYS: IMPLICATIONS FOR TRACING H2 GAS IN THE UNIVERSE. *The Astrophysical Journal*, 803(1):37. Publisher: The American Astronomical Society.

Blain, A.W., Smail, I., Ivison, R.J., et al., 2002. Submillimeter galaxies. *Physics Reports*, 369(2):111.

Bocchio, M., Jones, A.P., and Slavin, J.D., 2014. A re-evaluation of dust processing in supernova shock waves. *Astronomy and Astrophysics*, 570:A32. ADS Bibcode: 2014A&A...570A..32B.

Bothwell, M.S., Smail, I., Chapman, S.C., et al., 2013. A survey of molecular gas in luminous sub-millimetre galaxies. *Monthly Notices of the Royal Astronomical Society*, 429(4):3047.

Bournaud, F. and Combes, F., 2002. Gas accretion on spiral galaxies: Bar formation and renewal. *Astronomy & Astrophysics*, 392(1):83. Number: 1 Publisher: EDP Sciences.

Brown, T. and Wilson, C.D., 2019. Extreme CO Isotopologue Line Ratios in ULIRGS: Evidence for a Top-heavy IMF. *The Astrophysical Journal*, 879(1):17. Publisher: American Astronomical Society.

Béthermin, M., Greve, T.R., De Breuck, C., et al., 2018. Dense-gas tracers and carbon isotopes in five $2.5 < z < 4$ lensed dusty star-forming galaxies from the SPT SMG sample. *Astronomy & Astrophysics*, 620:A115.

Cai, Z.Y., Zotti, G.D., and Bonato, M., 2020. High- z Dusty Star-forming Galaxies: A Top-heavy Initial Mass Function? *The Astrophysical Journal*, 891(1):74.

Catelan, P. and Theuns, T., 1996. Evolution of the angular momentum of protogalaxies from tidal torques: Zel'dovich approximation. *Monthly Notices of the Royal Astronomical Society*, 282(2):436.

Cazzoli, G., Dore, L., and Puzzarini, C., 2009. The hyperfine structure of the inversion-rotation transition JK = of NH3 investigated by Lamb-dip spectroscopy. *Astronomy & Astrophysics*, 507(3):1707. Number: 3 Publisher: EDP Sciences.

Cañameras, R., Nesvadba, N.P.H., Kneissl, R., et al., 2021. *Planck* 's Dusty GEMS: VIII. Dense-gas reservoirs in the most active dusty starbursts at z 3. *Astronomy & Astrophysics*, 645:A45.

Ceccarelli, C., Dominik, C., López-Sepulcre, A., et al., 2014. HERSCHEL FINDS EVIDENCE FOR SLAR WIND PARTICLES IN A PROTOSLAR ENVELOPE: IS THIS WHAT HAPPENED TO THE YOUNG SUN? *The Astrophysical Journal Letters*, 790(1):L1. Publisher: The American Astronomical Society.

Chabrier, G., 2003. Galactic Stellar and Substellar Initial Mass Function. *Publications of the Astronomical Society of the Pacific*, 115(809):763.

Chapman, S.C., Ivison, R.J., Roseboom, I.G., et al., 2010. Herschel-SPIRE, far-infrared properties of millimetre-bright and -faint radio galaxies. *Monthly Notices of the Royal Astronomical Society: Letters*, 409(1):L13.

Chapman, S.C., Smail, I., Windhorst, R., et al., 2004. Evidence for Extended, Obscured Starbursts in Submillimeter Galaxies. *The Astrophysical Journal*, 611(2):732.

Cheung, A.C., Rank, D.M., Townes, C.H., et al., 1968. Detection of N${\mathrm{H}}_{3}$ Molecules in the Interstellar Medium by Their Microwave Emission. *Physical Review Letters*, 21(25):1701. Publisher: American Physical Society.

Cole, S., Norberg, P., Baugh, C.M., et al., 2001. The 2dF galaxy redshift survey: near-infrared galaxy luminosity functions. *Monthly Notices of the Royal Astronomical Society*, 326:255. ADS Bibcode: 2001MNRAS.326..255C.

Colgan, S.W.J., Haas, M.R., Erickson, E.F., et al., 1993. Detection of the N II 122 and 205 micron lines - Densities in G333.6-0.2. *The Astrophysical Journal*, 413:237.

Conley, A., Cooray, A., Vieira, J.D., et al., 2011. Discovery of a Multiply Lensed Submillimeter Galaxy in Early HerMES Herschel/SPIRE Data. *The Astrophysical Journal*, 732(2):L35.

Cowie, L.L., Hu, E.M., and Songaila, A., 1995. Faintest Galaxy Morphologies From HST WFPC2 Imaging of the Hawaii Survey Fields. *The Astronomical Journal*, 110:1576.

Dalgarno, A., 2006. The galactic cosmic ray ionization rate. *Proceedings of the National Academy of Sciences*, 103(33):12269. Publisher: Proceedings of the National Academy of Sciences.

Danielson, A.L.R., Swinbank, A.M., Smail, I., et al., 2011. The properties of the interstellar medium within a star-forming galaxy at z= 2.3. *Monthly Notices of the Royal Astronomical Society*, 410(3):1687.

Danielson, A.L.R., Swinbank, A.M., Smail, I., et al., 2013. 13CO and C18O emission from a dense gas disc at z = 2.3: abundance variations, cosmic rays and the initial conditions for star formation. *Monthly Notices of the Royal Astronomical Society*, 436(3):2793.

Davies, R.I., Sternberg, A., Lehnert, M., et al., 2003. Molecular Hydrogen Excitation in Ultraluminous Infrared Galaxies. *The Astrophysical Journal*, 597(2):907.

Davé, R., Anglés-Alcázar, D., Narayanan, D., et al., 2019. simba: Cosmological simulations with black hole growth and feedback. *Monthly Notices of the Royal Astronomical Society*, 486(2):2827.

Davé, R., Finlator, K., Oppenheimer, B.D., et al., 2010. The nature of submillimetre galaxies in cosmological hydrodynamic simulations. *Monthly Notices of the Royal Astronomical Society*, 404:1355.

de los Reyes, M.A.C. and Kennicutt, Jr., R.C., 2019. Revisiting the Integrated Star Formation Law. I. Non-starbursting Galaxies. *The Astrophysical Journal*, 872:16. ADS Bibcode: 2019ApJ...872...16D.

Dekel, A., Birnboim, Y., Engel, G., et al., 2009a. Cold streams in early massive hot haloes as the main mode of galaxy formation. *Nature*, 457:451.

Dekel, A., Sari, R., and Ceverino, D., 2009b. Formation of Massive Galaxies at High Redshift: Cold Streams, Clumpy Disks, and Compact Spheroids. *The Astrophysical Journal*, 703:785.

Dessauges-Zavadsky, M., Richard, J., Combes, F., et al., 2019. Molecular clouds in the Cosmic Snake normal star-forming galaxy 8 billion years ago. *Nature Astronomy*, 3(12):1115. Number: 12 Publisher: Nature Publishing Group.

Di Criscienzo, M., Dell'Agli, F., Ventura, P., et al., 2013. Dust formation in the winds of AGBs: the contribution at low metallicities. *Monthly Notices of the Royal Astronomical Society*, 433:313. ADS Bibcode: 2013MNRAS.433..313D.

Di Matteo, T., Springel, V., and Hernquist, L., 2005. Energy input from quasars regulates the growth and activity of black holes and their host galaxies. *Nature*, 433(7026):604. Number: 7026 Publisher: Nature Publishing Group.

Dicke, R.H., Peebles, P.J.E., Roll, P.G., et al., 1965. Cosmic Black-Body Radiation. *The Astrophysical Journal*, 142:414. ADS Bibcode: 1965ApJ...142..414D.

Doherty, M.J., Geach, J.E., Ivison, R.J., et al., 2020. [N ii] Fine-structure Emission at 122 and 205 $\upmu$m in a Galaxy at z = 2.6: A Globally Dense Star-forming Interstellar Medium. *The Astrophysical Journal*, 905(2):152. Publisher: American Astronomical Society.

Doherty, M.J., Geach, J.E., Ivison, R.J., et al., 2022. Ammonia in the interstellar medium of a starbursting disc at z = 2.6. *Monthly Notices of the Royal Astronomical Society: Letters*, page slac111.

Downes, D. and Solomon, P.M., 1998. Rotating Nuclear Rings and Extreme Starbursts in Ultraluminous Galaxies. *The Astrophysical Journal*, 507:615.

Draine, B.T., 2011. *Physics of the Interstellar and Intergalactic Medium*. Princeton University Press. Google-Books-ID: XWOYDwAAQBAJ.

Draine, B.T. and Salpeter, E.E., 1979. On the physics of dust grains in hot gas. *The Astrophysical Journal*, 231:77. ADS Bibcode: 1979ApJ...231...77D.

Dunne, L., Maddox, S.J., Papadopoulos, P.P., et al., 2022. Dust, CO, and [Ci]: cross-calibration of molecular gas mass tracers in metal-rich galaxies across cosmic time. *Monthly Notices of the Royal Astronomical Society*, 517(1):962.

Dye, S., Eales, S.A., Gomez, H.L., et al., 2022. A high-resolution investigation of the multiphase ISM in a galaxy during the first two billion years. *Monthly Notices of the Royal Astronomical Society*, 510(3):3734.

Dye, S., Furlanetto, C., Dunne, L., et al., 2018. Modelling high-resolution ALMA observations of strongly lensed highly star-forming galaxies detected by Herschel. *Monthly Notices of the Royal Astronomical Society*, 476:4383.

Dye, S., Furlanetto, C., Swinbank, A.M., et al., 2015. Revealing the complex nature of the strong gravitationally lensed system H-ATLAS J090311.6+003906 using ALMA. *Monthly Notices of the Royal Astronomical Society*, 452(3):2258.

Dyson, F.W., Eddington, A.S., and Davidson, C., 1920. IX. A determination of the deflection of light by the sun's gravitational field, from observations made at the total eclipse of May

29, 1919. *Philosophical Transactions of the Royal Society of London. Series A, Containing Papers of a Mathematical or Physical Character*, 220(571-581):291. Publisher: Royal Society.

Einstein, A., 1916. Die Grundlage der allgemeinen Relativitätstheorie. *Annalen der Physik*, 354:769. ADS Bibcode: 1916AnP...354..769E.

Einstein, A., 1936. Lens-Like Action of a Star by the Deviation of Light in the Gravitational Field. *Science*, 84:506. ADS Bibcode: 1936Sci....84..506E.

Elmegreen, B.G., 2012. What triggers star formation in galaxies? 284:317. Conference Name: The Spectral Energy Distribution of Galaxies - SED 2011 Place: eprint: arXiv:1201.3659 ADS Bibcode: 2012IAUS..284..317E.

Elmegreen, D.M., Elmegreen, B.G., Rubin, D.S., et al., 2005. Galaxy Morphologies in the Hubble Ultra Deep Field: Dominance of Linear Structures at the Detection Limit. *The Astrophysical Journal*, 631(1):85.

Engel, H., Tacconi, L.J., Davies, R.I., et al., 2010. Most Submillimeter Galaxies are Major Mergers. *The Astrophysical Journal*, 724:233. ADS Bibcode: 2010ApJ...724..233E.

Fehér, O., Tóth, L.V., Kraus, A., et al., 2022. Ammonia Emission in Various Star-forming Environments: A Pilot Study of Planck Galactic Cold Clumps. *The Astrophysical Journal Supplement Series*, 258(1):17.

Ferrarotti, A.S. and Gail, H.P., 2006. Composition and quantities of dust produced by AGB-stars and returned to the interstellar medium. *Astronomy and Astrophysics*, 447:553. ADS Bibcode: 2006A&A...447..553F.

Flannery, B.P., Rybicki, G.B., and Sarazin, C.L., 1979. Ultraviolet pumping of N/+/ fine-structure levels. *The Astrophysical Journal*, 229:1057.

Friedmann, A., 1922. Über die Krümmung des Raumes. *Zeitschrift fur Physik*, 10:377. ADS Bibcode: 1922ZPhy...10..377F.

Fudamoto, Y., Ivison, R.J., Oteo, I., et al., 2017. The most distant, luminous, dusty star-forming galaxies: redshifts from NOEMA and ALMA spectral scans. *Monthly Notices of the Royal Astronomical Society*, 472(2):2028.

Gaches, B.A.L., Offner, S.S.R., and Bisbas, T.G., 2019. The Astrochemical Impact of Cosmic Rays in Protoclusters. I. Molecular Cloud Chemistry. *The Astrophysical Journal*, 878(2):105. Publisher: The American Astronomical Society.

Gaensler, B.M., Madsen, G.J., Chatterjee, S., et al., 2008. The Vertical Structure of Warm Ionised Gas in the Milky Way. *Publications of the Astronomical Society of Australia*, 25(4):184.

Gao, Y. and Solomon, P.M., 2004. The Star Formation Rate and Dense Molecular Gas in Galaxies. *ApJ*, 606(1):271.

Geach, J.E., Ivison, R.J., Dye, S., et al., 2018. A Magnified View of Circumnuclear Star Formation and Feedback around an Active Galactic Nucleus at z = 2.6. *The Astrophysical Journal*, 866(1):L12.

Geach, J.E., More, A., Verma, A., et al., 2015. The Red Radio Ring: a gravitationally lensed hyperluminous infrared radio galaxy at z = 2.553 discovered through the citizen science project Space Warps. *Monthly Notices of the Royal Astronomical Society*, 452(1):502.

Geach, J.E. and Papadopoulos, P.P., 2012. MOLECULAR AND ATOMIC LINE SURVEYS OF GALAXIES. I. THE DENSE, STAR-FORMING GAS PHASE AS A BEACON. *The Astrophysical Journal*, 757(2):156.

Genzel, R. and Stutzki, J., 1989. The Orion Molecular Cloud and Star-Forming Region. *Annual Review of Astronomy and Astrophysics*, 27(1):41. _eprint: https://doi.org/10.1146/annurev.aa.27.090189.000353.

George, R.D., Ivison, R.J., Smail, I., et al., 2014. Herschel reveals a molecular outflow in a z = 2.3 ULIRG. *Monthly Notices of the Royal Astronomical Society*, 442(2):1877.

Gezari, D.Y., Backman, D.E., and Werner, M.W., 1998. Mid-Infrared Imaging of Orion BN/KL. II. Luminosity Sources, Extinction Distribution, and the Nature of IRc2. *The Astrophysical Journal*, 509:283. ADS Bibcode: 1998ApJ...509..283G.

Goldsmith, P.F., Yıldız, U.A., Langer, W.D., et al., 2015. *HERSCHEL* GALACTIC PLANE SURVEY OF [N ii] FINE STRUCTURE EMISSION. *The Astrophysical Journal*, 814(2):133.

Gullberg, B., Swinbank, A.M., Smail, I., et al., 2018. The Dust and [C ii] Morphologies of Redshift 4.5 Sub-millimeter Galaxies at 200 pc Resolution: The Absence of Large Clumps in the Interstellar Medium at High-redshift. *The Astrophysical Journal*, 859(1):12.

Guth, A.H., 1981. Inflationary universe: A possible solution to the horizon and flatness problems. *Physical Review D*, 23(2):347. Publisher: American Physical Society.

Guélin, M., Salomé, P., Neri, R., et al., 2007. Detection of HNC and tentative detection of CN at $z = 3.9$. *Astronomy & Astrophysics*, 462(3):L45.

Harrington, K.C., Vishwas, A., Weiß, A., et al., 2019. The 'Red Radio Ring': ionized and molecular gas in a starburst/active galactic nucleus at z 2.55. *Monthly Notices of the Royal Astronomical Society*, 488(2):1489.

Harrington, K.C., Yun, M.S., Cybulski, R., et al., 2016. Early science with the Large Millimeter Telescope: observations of extremely luminous high-z sources identified by Planck. *Monthly Notices of the Royal Astronomical Society*, 458:4383.

Hatsukade, B., Tamura, Y., Iono, D., et al., 2015. High-resolution ALMA observations of SDP.81. II. Molecular clump properties of a lensed submillimeter galaxy at z = 3.042. *Publications of the Astronomical Society of Japan*, 67(5):93.

Hayward, C.C., Narayanan, D., Kereš, D., et al., 2013. Submillimetre galaxies in a hierarchical universe: number counts, redshift distribution and implications for the IMF. *Monthly Notices of the Royal Astronomical Society*, 428(3):2529. Publisher: Oxford Academic.

Herrera-Camus, R., Bolatto, A., Smith, J.D., et al., 2016. THE IONIZED GAS IN NEARBY GALAXIES AS TRACED BY THE [NII] 122 AND 205 m TRANSITIONS. *The Astrophysical Journal*, 826(2):175.

Hirschi, R., 2007. Very low-metallicity massive stars:: Pre-SN evolution models and primary nitrogen production. *Astronomy & Astrophysics*, 461(2):571.

Ho, P.T.P. and Townes, C.H., 1983. Interstellar ammonia. *Annual Review of Astronomy and Astrophysics*, 21:239.

Hodge, J.A. and da Cunha, E., 2020. High-redshift star formation in the ALMA era. *arXiv:2004.00934 [astro-ph]*. ArXiv: 2004.00934.

Hodge, J.A., Swinbank, A.M., Simpson, J.M., et al., 2016. KILOPARSEC-SCALE DUST DISKS IN HIGH-REDSHIFT LUMINOUS SUBMILLIMETER GALAXIES. *The Astrophysical Journal*, 833(1):103.

Hopkins, P.F., 2013. Variations in the stellar CMF and IMF: from bottom to top. *Monthly Notices of the Royal Astronomical Society*, 433(1):170. Publisher: Oxford Academic.

Hopkins, P.F., Bundy, K., Croton, D., et al., 2010. Mergers and Bulge Formation in CDM: Which Mergers Matter? *The Astrophysical Journal*, 715:202. ADS Bibcode: 2010ApJ...715..202H.

Hopkins, P.F., Cox, T.J., Younger, J.D., et al., 2009. How do Disks Survive Mergers? *The Astrophysical Journal*, 691:1168. ADS Bibcode: 2009ApJ...691.1168H.

Hubble, E., 1929. A Relation between Distance and Radial Velocity among Extra-Galactic Nebulae. *Proceedings of the National Academy of Science*, 15:168. ADS Bibcode: 1929PNAS...15..168H.

Hubble, E.P., 1927. The classification of spiral nebulae. *The Observatory*, 50:276. ADS Bibcode: 1927Obs....50..276H.

Hughes, D.H., Serjeant, S., Dunlop, J., et al., 1998. High-redshift star formation in the Hubble Deep Field revealed by a submillimetre-wavelength survey. *Nature*, 394:241.

Högbom, J.A., 1974. Aperture Synthesis with a Non-Regular Distribution of Interferometer Baselines. *Astronomy and Astrophysics Supplement Series*, 15:417. ADS Bibcode: 1974A&AS...15..417H.

Imanishi, M., Nakagawa, T., Shirahata, M., et al., 2010. AKARI IRC Infrared 2.5-5 m Spectroscopy of a Large Sample of Luminous Infrared Galaxies. *The Astrophysical Journal*, 721:1233. ADS Bibcode: 2010ApJ...721.1233I.

Inami, H., Armus, L., Matsuhara, H., et al., 2018. The AKARI 2.5–5 micron spectra of luminous infrared galaxies in the local Universe. *Astronomy & Astrophysics*, 617:A130. Publisher: EDP Sciences.

Inoue, S., Dekel, A., Mandelker, N., et al., 2016. Non-linear violent disc instability with high Toomre's Q in high-redshift clumpy disc galaxies. *Monthly Notices of the Royal Astronomical Society*, 456(2):2052.

Ivison, R.J., Page, M.J., Cirasuolo, M., et al., 2019. Hyperluminous starburst gives up its secrets. *Monthly Notices of the Royal Astronomical Society*, 489(1):427.

Ivison, R.J., Papadopoulos, P.P., Smail, I., et al., 2011. Tracing the molecular gas in distant submillimetre galaxies via CO(1-0) imaging with the Expanded Very Large Array: EVLA

imaging of CO(1-0) in submm galaxies. *Monthly Notices of the Royal Astronomical Society*, 412(3):1913.

Ivison, R.J., Richard, J., Biggs, A.D., et al., 2020. Giant star-forming clumps? *Monthly Notices of the Royal Astronomical Society: Letters*, 495(1):L1. ArXiv: 2003.07863.

Ivison, R.J., Swinbank, A.M., Swinyard, B., et al., 2010. *Herschel* and SCUBA-2 imaging and spectroscopy of a bright, lensed submillimetre galaxy at $z = 2.3$. *Astronomy and Astrophysics*, 518:L35.

Jeřábková, T., Hasani Zonoozi, A., Kroupa, P., et al., 2018. Impact of metallicity and star formation rate on the time-dependent, galaxy-wide stellar initial mass function. *Astronomy and Astrophysics*, 620:A39.

Jiang, T., Malhotra, S., Yang, H., et al., 2019. Correlation between SFR Surface Density and Thermal Pressure of Ionized Gas in Local Analogs of High-redshift Galaxies. *The Astrophysical Journal*, 872(2):146.

Jiménez-Andrade, E.F., Magnelli, B., Karim, A., et al., 2018. Molecular gas in AzTEC/C159: a star-forming disk galaxy 1.3 Gyr after the Big Bang. *Astronomy & Astrophysics*, 615:A25. Publisher: EDP Sciences.

Jiménez-Donaire, M.J., Bigiel, F., Leroy, A.K., et al., 2019. EMPIRE: The IRAM 30 m Dense Gas Survey of Nearby Galaxies. *The Astrophysical Journal*, 880(2):127. Publisher: The American Astronomical Society.

Jiménez-Donaire, M.J., Cormier, D., Bigiel, F., et al., 2017. 13 CO/C 18 O Gradients across the Disks of Nearby Spiral Galaxies. *The Astrophysical Journal*, 836(2):L29. Publisher: American Astronomical Society.

Jones, A.P. and Nuth, J.A., 2011. Dust destruction in the ISM: a re-evaluation of dust lifetimes. *Astronomy and Astrophysics*, 530:A44. ADS Bibcode: 2011A&A...530A..44J.

Kaasinen, M., Bian, F., Groves, B., et al., 2017. The COSMOS [OII] Survey: Evolution of Electron Density with Star Formation Rate. *Monthly Notices of the Royal Astronomical Society*, 465(3):3220. ArXiv: 1611.01166.

Kauffmann, G. and Haehnelt, M., 2000. A unified model for the evolution of galaxies and quasars. *Monthly Notices of the Royal Astronomical Society*, 311(3):576.

Kennicutt, R.C., 1998. STAR FORMATION IN GALAXIES ALONG THE HUBBLE SEQUENCE. *Annual Review of Astronomy and Astrophysics*, 36(1):189.

Kennicutt, R.C. and Evans, N.J., 2012. Star Formation in the Milky Way and Nearby Galaxies. *Annual Review of Astronomy and Astrophysics*, 50:531.

Kim, J.h., Wise, J.H., and Abel, T., 2009. Galaxy Mergers with Adaptive Mesh Refinement: Star Formation and Hot Gas Outflow. *The Astrophysical Journal*, 694:L123. ADS Bibcode: 2009ApJ...694L.123K.

Kobayashi, C., Karakas, A.I., and Lugaro, M., 2020. The Origin of Elements from Carbon to Uranium. *The Astrophysical Journal*, 900:179. ADS Bibcode: 2020ApJ...900..179K.

Kobayashi, C., Karakas, A.I., and Umeda, H., 2011. The evolution of isotope ratios in the Milky Way Galaxy. *Monthly Notices of the Royal Astronomical Society*, 414:3231.

Kobayashi, C., Tsujimoto, T., and Nomoto, K., 2000. The History of the Cosmic Supernova Rate Derived from the Evolution of the Host Galaxies. *The Astrophysical Journal*, 539:26.

Koopmans, L.V.E., Treu, T., Bolton, A.S., et al., 2006. The Sloan Lens ACS Survey. III. The Structure and Formation of Early-Type Galaxies and Their Evolution since z 1. *The Astrophysical Journal*, 649(2):599.

Kormendy, J. and Gebhardt, K., 2001. Supermassive black holes in galactic nuclei. 586:363. Conference Name: 20th Texas Symposium on relativistic astrophysics Place: eprint: arXiv:astro-ph/0105230 ADS Bibcode: 2001AIPC..586..363K.

Krips, M., Neri, R., García-Burillo, S., et al., 2008. A Multi-Transition HCN and HCO+ Study of 12 Nearby Active Galaxies: Active Galactic Nucleus versus Starburst Environments. *The Astrophysical Journal*, 677:262. ADS Bibcode: 2008ApJ...677..262K.

Kroupa, P., 2001. On the variation of the initial mass function. *Monthly Notices of the Royal Astronomical Society*, 322(2):231.

Kroupa, P., 2008. The IMF of Simple and Composite Populations. volume 390, page 3. Place: eprint: arXiv:0708.1164 ADS Bibcode: 2008ASPC..390....3K.

Kroupa, P., Tout, C.A., and Gilmore, G., 1993. The distribution of low-mass stars in the Galactic disc. *Monthly Notices of the Royal Astronomical Society*, 262:545.

Kroupa, P. and Weidner, C., 2003. Galactic-Field Initial Mass Functions of Massive Stars. *The Astrophysical Journal*, 598(2):1076.

Krumholz, M.R., 2006. High Mass Star Formation by Gravitational Collapse of Massive Cores. *arXiv Astrophysics e-prints*, pages arXiv:astro–ph/0607429.

Krumholz, M.R. and Thompson, T.A., 2007. The Relationship between Molecular Gas Tracers and Kennicutt-Schmidt Laws. *The Astrophysical Journal*, 669:289. ADS Bibcode: 2007ApJ...669..289K.

Köhler, M., Ysard, N., and Jones, A.P., 2015. Dust evolution in the transition towards the denser ISM: impact on dust temperature, opacity, and spectral index. *Astronomy and Astrophysics*, 579:A15. ADS Bibcode: 2015A&A...579A..15K.

Larson, K.L., Sanders, D.B., Barnes, J.E., et al., 2016. MORPHOLOGY AND MOLECULAR GAS FRACTIONS OF LOCAL LUMINOUS INFRARED GALAXIES AS A FUNCTION OF INFRARED LUMINOSITY AND MERGER STAGE. *The Astrophysical Journal*, 825(2):128. Publisher: The American Astronomical Society.

Leavitt, H.S., 1908. 1777 variables in the Magellanic Clouds. *Annals of Harvard College Observatory*, 60:87. ADS Bibcode: 1908AnHar..60...87L.

Li, A. and Greenberg, J.M., 2003. *In dust we trust: an overview of observations and theories of interstellar dust*, volume 120. eprint: arXiv:astro-ph/0204392. Conference Name: Solid State Astrochemistry Pages: 37-84 ADS Bibcode: 2003ssac.proc...37L.

Limongi, M. and Chieffi, A., 2018. Presupernova Evolution and Explosive Nucleosynthesis of Rotating Massive Stars in the Metallicity Range -3 $\leq$ [Fe/H] $\leq$ 0. *The Astrophysical Journal Supplement Series*, 237(1):13. Publisher: American Astronomical Society.

Linde, A.D., 1983. Chaotic inflation. *Physics Letters B*, 129(3):177.

Liu, B., Chartab, N., Nayyeri, H., et al., 2022. Massive Molecular Gas Reservoir in a Luminous Submillimeter Galaxy during Cosmic Noon. *The Astrophysical Journal*, 929(1):41.

Liu, L., Weiß, A., Perez-Beaupuits, J.P., et al., 2017. HIFI Spectroscopy of H2O Submillimeter Lines in Nuclei of Actively Star-forming Galaxies. *The Astrophysical Journal*, 846(1):5. Publisher: American Astronomical Society.

Lovell, C.C., Geach, J.E., Davé, R., et al., 2021. Reproducing sub-millimetre galaxy number counts with cosmological hydrodynamic simulations. *Monthly Notices of the Royal Astronomical Society*, (staa4043).

Marshall, P.J., Verma, A., More, A., et al., 2016. SPACE WARPS - I. Crowdsourcing the discovery of gravitational lenses. *Monthly Notices of the Royal Astronomical Society*, 455:1171.

Martín, S., Muller, S., Henkel, C., et al., 2019. Spatially resolved carbon and oxygen isotopic ratios in NGC 253 using optically thin tracers. *Astronomy & Astrophysics*, 624:A125. Publisher: EDP Sciences.

Masters, D., McCarthy, P., Siana, B., et al., 2014. PHYSICAL PROPERTIES OF EMISSION-LINE GALAXIES AT z 2 FROM NEAR-INFRARED SPECTROSCOPY WITH MAGELLAN FIRE. *The Astrophysical Journal*, 785(2):153.

Mather, J.C., Cheng, E.S., Eplee, Jr., R.E., et al., 1990. A Preliminary Measurement of the Cosmic Microwave Background Spectrum by the Cosmic Background Explorer (COBE) Satellite. *The Astrophysical Journal*, 354:L37. ADS Bibcode: 1990ApJ...354L..37M.

McConachie, I., Wilson, G., Forrest, B., et al., 2022. Spectroscopic Confirmation of a Protocluster at z = 3.37 with a High Fraction of Quiescent Galaxies. *The Astrophysical Journal*, 926(1):37. Publisher: The American Astronomical Society.

Menten, K.M., Guesten, R., Leurini, S., et al., 2008. Submillimeter water and ammonia absorption by the peculiar z˜0.89 interstellar medium in the gravitational lens of the PKS 1830-211 system. *Astronomy & Astrophysics*, 492(3):725. ArXiv: 0810.2782.

Menéndez-Delmestre, K., Blain, A.W., Smail, I., et al., 2009. MID-INFRARED SPECTROSCOPY OF SUBMILLIMETER GALAXIES: EXTENDED STAR FORMATION IN MASSIVE HIGH-REDSHIFT GALAXIES. *The Astrophysical Journal*, 699(1):667.

Merritt, D. and Ferrarese, L., 2001. The M•- Relation for Supermassive Black Holes. *The Astrophysical Journal*, 547:140. ADS Bibcode: 2001ApJ...547..140M.

Meynet, G. and Maeder, A., 1997. Stellar evolution with rotation. I. The computational method and the inhibiting effect of the -gradient. *Astronomy and Astrophysics*, 321:465.

Miller, T.B., Chapman, S.C., Aravena, M., et al., 2018. A massive core for a cluster of galaxies at a redshift of 4.3. *Nature*, 556(7702):469. Number: 7702 Publisher: Nature Publishing Group.

Mo, H.J., Mao, S., and White, S.D.M., 1998. The formation of galactic discs.

Mor, R., Robin, A.C., Figueras, F., et al., 2017. Constraining the thin disc initial mass function using Galactic classical Cepheids. *Astronomy and Astrophysics*, 599:A17.

More, A., Verma, A., Marshall, P.J., et al., 2016. SPACE WARPS- II. New gravitational lens candidates from the CFHTLS discovered through citizen science. *Monthly Notices of the Royal Astronomical Society*, 455:1191.

Motte, F., Nony, T., Louvet, F., et al., 2018. The unexpectedly large proportion of high-mass star-forming cores in a Galactic mini-starburst. *Nature Astronomy*, 2(6):478. Number: 6 Publisher: Nature Publishing Group.

Muller, S., Combes, F., Guélin, M., et al., 2014. An ALMA Early Science survey of molecular absorption lines toward PKS 1830-211. Analysis of the absorption profiles. *Astronomy and Astrophysics*, 566:A112. ADS Bibcode: 2014A&A...566A.112M.

Murray, N., Quataert, E., and Thompson, T.A., 2005. On the Maximum Luminosity of Galaxies and Their Central Black Holes: Feedback from Momentum-driven Winds. *The Astrophysical Journal*, 618(2):569. Publisher: IOP Publishing.

Naab, T., Oser, L., Emsellem, E., et al., 2014. The ATLAS3D project - XXV. Two-dimensional kinematic analysis of simulated galaxies and the cosmological origin of fast and slow rotators. *Monthly Notices of the Royal Astronomical Society*, 444:3357. ADS Bibcode: 2014MNRAS.444.3357N.

Narayanan, D., Cox, T.J., Shirley, Y., et al., 2008. Molecular Star Formation Rate Indicators in Galaxies. *The Astrophysical Journal*, 684:996. ADS Bibcode: 2008ApJ...684..996N.

Narayanan, D., Krumholz, M., Ostriker, E.C., et al., 2011. The CO–H2 conversion factor in disc galaxies and mergers. *Monthly Notices of the Royal Astronomical Society*, 418(1):664.

Noguchi, M., 1999. Early Evolution of Disk Galaxies: Formation of Bulges in Clumpy Young Galactic Disks. *The Astrophysical Journal*, 514(1):77. Publisher: IOP Publishing.

Nomoto, K., Kobayashi, C., and Tominaga, N., 2013. Nucleosynthesis in Stars and the Chemical Enrichment of Galaxies. *Annual Review of Astronomy and Astrophysics*, 51:457. ADS Bibcode: 2013ARA&A..51..457N.

Oberst, T.E., Parshley, S.C., Stacey, G.J., et al., 2006. Detection of the 205 $\upmu$m [N ii] Line from the Carina Nebula. *The Astrophysical Journal*, 652(2):L125. Publisher: IOP Publishing.

Olofsson, A.O.H., Persson, C.M., Koning, N., et al., 2007. A spectral line survey of Orion KL in the bands 486–492 and 541–577 GHz with the Odin satellite: I. The observational data. *Astronomy & Astrophysics*, 476(2):791.

Oteo, I., Zhang, Z.Y., Yang, C., et al., 2017. High Dense Gas Fraction in Intensely Star-forming Dusty Galaxies. *The Astrophysical Journal*, 850(2):170. Publisher: American Astronomical Society.

Ott, J., Henkel, C., Braatz, J.A., et al., 2011. Ammonia as a Temperature Tracer in the Ultraluminous Galaxy Merger Arp 220. *The Astrophysical Journal*, 742:95. ADS Bibcode: 2011ApJ...742...95O.

Padoan, P. and Nordlund, , 2002. The Stellar Initial Mass Function from Turbulent Fragmentation. *The Astrophysical Journal*, 576:870. ADS Bibcode: 2002ApJ...576..870P.

Papadopoulos, P.P. and Geach, J.E., 2012. MOLECULAR AND ATOMIC LINE SURVEYS OF GALAXIES. II. UNBIASED ESTIMATES OF THEIR STAR FORMATION MODE. *The Astrophysical Journal*, 757(2):157. Publisher: IOP Publishing.

Partnership, A., Vlahakis, C., Hunter, T.R., et al., 2015. THE 2014 ALMA LONG BASELINE CAMPAIGN: OBSERVATIONS OF THE STRONGLY LENSED SUBMILLIMETER GALAXY HATLAS J090311.6+003906 AT z = 3.042*. *The Astrophysical Journal Letters*, 808(1):L4. Publisher: The American Astronomical Society.

Peebles, P.J.E., 1968. Recombination of the Primeval Plasma. *The Astrophysical Journal*, 153:1. ADS Bibcode: 1968ApJ...153....1P.

Peebles, P.J.E., 1969. Origin of the Angular Momentum of Galaxies. *The Astrophysical Journal*, 155:393. ADS Bibcode: 1969ApJ...155..393P.

Penzias, A.A. and Wilson, R.W., 1965. A Measurement of Excess Antenna Temperature at 4080 Mc/s. *The Astrophysical Journal*, 142:419. ADS Bibcode: 1965ApJ...142..419P.

Persson, C.M., Black, J.H., Cernicharo, J., et al., 2010. Nitrogen hydrides in interstellar gas. Herschel/HIFI observations towards G10.6-0.4 (W31C). *Astronomy and Astrophysics*, 521:L45. ADS Bibcode: 2010A&A...521L..45P.

Persson, C.M., de Luca, M., Mookerjea, B., et al., 2011. Nitrogen hydrides in interstellar gas towards G10.6-0.4 (W31C) and W49N. 280:296. Conference Name: The Molecular Universe ADS Bibcode: 2011IAUS..280P.296P.

Persson, C.M., Olofsson, A.O.H., Koning, N., et al., 2007. A spectral line survey of Orion KL in the bands 486-492 and 541-577 GHz with the Odin satellite - II. Data analysis. *Astronomy & Astrophysics*, 476(2):807. Number: 2 Publisher: EDP Sciences.

Petuchowski, S.J., Bennett, C.L., Haas, M.R., et al., 1994. The N (II) 205 micron line in M82: The warm ionized medium. *The Astrophysical Journal Letters*, 427:L17.

Planck Collaboration, Ade, P.A.R., Aghanim, N., et al., 2016. Planck 2015 results. XIII. Cosmological parameters. *Astronomy and Astrophysics*, 594:A13.

Portinari, L., Chiosi, C., and Bressan, A., 1998. Galactic chemical enrichment with new metallicity dependent stellar yields. *Astronomy and Astrophysics*, 334:505. ADS Bibcode: 1998A&A...334..505P.

Pouteau, Y., Motte, F., Nony, T., et al., 2022. ALMA-IMF. III. Investigating the origin of stellar masses: top-heavy core mass function in the W43-MM2&MM3 mini-starburst. *Astronomy and Astrophysics*, 664:A26. ADS Bibcode: 2022A&A...664A..26P.

Prantzos, N., Abia, C., Limongi, M., et al., 2018. Chemical evolution with rotating massive star yields – I. The solar neighbourhood and the s-process elements. *Monthly Notices of the Royal Astronomical Society*, 476(3):3432.

Privon, G.C., Herrero-Illana, R., Evans, A.S., et al., 2015. EXCITATION MECHANISMS FOR HCN(1–0) AND HCO+(1–0) IN GALAXIES FROM THE GREAT OBSERVATORIES ALL-SKY LIRG SURVEY*. *The Astrophysical Journal*, 814(1):39. Publisher: The American Astronomical Society.

Reines, A.E. and Volonteri, M., 2015. RELATIONS BETWEEN CENTRAL BLACK HOLE MASS AND TOTAL GALAXY SLAR MASS IN THE LOCAL UNIVERSE. *The Astrophysical Journal*, 813(2):82. Publisher: The American Astronomical Society.

Remijan, A.J., Markwick-Kemper, A., and ALMA Working Group on Spectral Line Frequencies, 2007. Splatalogue: Database for Astronomical Spectroscopy. ADS Bibcode: 2007AAS...21113211R.

Reuter, C., Spilker, J.S., Vieira, J.D., et al., 2023. The Rest-frame Submillimeter Spectrum of High-redshift, Dusty, Star-forming Galaxies from the SPT-SZ Survey. *The Astrophysical Journal*, 948:44. ADS Bibcode: 2023ApJ...948...44R.

Riechers, D.A., Bradford, C.M., Clements, D.L., et al., 2013. A dust-obscured massive maximum-starburst galaxy at a redshift of 6.34. *Nature*, 496(7445):329. Number: 7445 Publisher: Nature Publishing Group.

Riechers, D.A., Hodge, J., Walter, F., et al., 2011. EXTENDED COLD MOLECULAR GAS RESERVOIRS IN z $\simeq$ 3.4 SUBMILLIMETER GALAXIES. *The Astrophysical Journal*, 739(1):L31. Publisher: IOP Publishing.

Rigopoulou, D., Hurley, P.D., Swinyard, B.M., et al., 2013. Herschel-SPIRE Fourier transform spectroscopy of the nearby spiral galaxy IC 342. *Monthly Notices of the Royal Astronomical Society*, 434(3):2051.

Romano, D., Chiappini, C., Matteucci, F., et al., 2005. Quantifying the uncertainties of chemical evolution studies - I. Stellar lifetimes and initial mass function. *Astronomy & Astrophysics*, 430(2):491. Number: 2 Publisher: EDP Sciences.

Romano, D., Matteucci, F., Zhang, Z.Y., et al., 2017. The evolution of CNO isotopes: a new window on cosmic star formation history and the stellar IMF in the age of ALMA. *Monthly Notices of the Royal Astronomical Society*, 470(1):401.

Romano, D., Matteucci, F., Zhang, Z.Y., et al., 2019. The evolution of CNO isotopes: the impact of massive stellar rotators. *Monthly Notices of the Royal Astronomical Society*, 490(2):2838.

Romano, D., Matteucci, F., Zhang, Z.Y., et al., 2020. Erratum: The evolution of CNO isotopes: a new window on cosmic star formation history and the stellar IMF in the age of ALMA. *Monthly Notices of the Royal Astronomical Society*, 499(1):523.

Rosenberg, M.J.F., Kazandjian, M.V., van der Werf, P.P., et al., 2014. Radiative and mechanical feedback into the molecular gas of NGC 253. *Astronomy & Astrophysics*, 564:A126.

Rosenberg, M.J.F., Werf, P.P.v.d., Aalto, S., et al., 2015. THEHERSCHELCOMPREHENSIVE (U)LIRG EMISSION SURVEY (HERCULES): CO LADDERS, FINE STRUCTURE LINES, AND NEUTRAL GAS COOLING. *The Astrophysical Journal*, 801(2):72.

Rujopakarn, W., Rieke, G.H., Eisenstein, D.J., et al., 2011. MORPHOLOGY AND SIZE DIFFERENCES BETWEEN LOCAL AND HIGH-REDSHIFT LUMINOUS INFRARED GALAXIES. *The Astrophysical Journal*, 726(2):93.

Rybak, M., Hodge, J.A., Greve, T.R., et al., 2022. PRUSSIC - I. A JVLA survey of HCN, HCO+, and HNC (1–0) emission in z 3 dusty galaxies: Low dense-gas fractions in high-redshift star-forming galaxies. *Astronomy & Astrophysics*, 667:A70. Publisher: EDP Sciences.

Rybak, M., Hodge, J.A., Vegetti, S., et al., 2020. Full of Orions: a 200-pc mapping of the interstellar medium in the redshift-3 lensed dusty star-forming galaxy SDP.81. *Monthly Notices of the Royal Astronomical Society*, 494(4):5542. Publisher: Oxford Academic.

Rybak, M., Vegetti, S., McKean, J.P., et al., 2015. ALMA imaging of SDP.81 – II. A pixelated reconstruction of the CO emission lines. *Monthly Notices of the Royal Astronomical Society: Letters*, 453(1):L26.

Saha, K. and Cortesi, A., 2018. Forming Lenticular Galaxies via Violent Disk Instability. *The Astrophysical Journal Letters*, 862(1):L12. Publisher: The American Astronomical Society.

Saitoh, T.R., Daisaka, H., Kokubo, E., et al., 2009. Toward First-Principle Simulations of Galaxy Formation: II. Shock-Induced Starburst at a Collision Interface during the First Encounter of Interacting Galaxies. *Publications of the Astronomical Society of Japan*, 61:481. ADS Bibcode: 2009PASJ...61..481S.

Salpeter, E.E., 1955. The Luminosity Function and Stellar Evolution. *The Astrophysical Journal*, 121:161.

Sanders, D.B., Soifer, B.T., Elias, J.H., et al., 1988. Ultraluminous Infrared Galaxies and the Origin of Quasars. *The Astrophysical Journal*, 325:74. ADS Bibcode: 1988ApJ...325...74S.

Sarangi, A. and Cherchneff, I., 2013. The Chemically Controlled Synthesis of Dust in Type II-P Supernovae. *The Astrophysical Journal*, 776:107. ADS Bibcode: 2013ApJ...776..107S.

Scalo, J.M., 1986. The stellar initial mass function. *Fundamentals of Cosmic Physics*, 11:1.

Schaye, J., Crain, R.A., Bower, R.G., et al., 2015. The EAGLE project: simulating the evolution and assembly of galaxies and their environments. *Monthly Notices of the Royal Astronomical Society*, 446(1):521.

Schmidt, M., 1959. The Rate of Star Formation. *The Astrophysical Journal*, 129:243. ADS Bibcode: 1959ApJ...129..243S.

Schmidt, M.R., He, J.H., Szczerba, R., et al., 2016. *Herschel* /HIFI observations of the circumstellar ammonia lines in IRC+10216. *Astronomy & Astrophysics*, 592:A131.

Schneider, F.R.N., Sana, H., Evans, C.J., et al., 2018. An excess of massive stars in the local 30 Doradus starburst. *Science*, 359:69. ADS Bibcode: 2018Sci...359...69S.

Schneider, P. and Sluse, D., 2013. Mass-sheet degeneracy, power-law models and external convergence: Impact on the determination of the Hubble constant from gravitational lensing. *Astronomy & Astrophysics*, 559:A37. Publisher: EDP Sciences.

Schwarzschild, K., 1916. On the Gravitational Field of a Mass Point According to Einstein's Theory. *Abh. Konigl. Preuss. Akad. Wissenschaften Jahre 1906,92, Berlin,1907*, 1916:189. ADS Bibcode: 1916AbhKP1916..189S.

Shimakawa, R., Kodama, T., Steidel, C.C., et al., 2015. Correlation between star formation activity and electron density of ionized gas at z = 2.5. *Monthly Notices of the Royal Astronomical Society*, 451:1284.

Shirazi, M., Brinchmann, J., and Rahmati, A., 2014. STARS WERE BORN IN SIGNIFICANTLY DENSER REGIONS IN THE EARLY UNIVERSE. *The Astrophysical Journal*, 787(2):120.

Shirley, Y.L., 2015. The Critical Density and the Effective Excitation Density of Commonly Observed Molecular Dense Gas Tracers. *Publications of the Astronomical Society of the Pacific*, 127(949):299. Publisher: IOP Publishing.

Simpson, J.M., Swinbank, A.M., Smail, I., et al., 2014. AN ALMA SURVEY OF SUBMILLIMETER GALAXIES IN THE EXTENDED CHANDRA DEEP FIELD SOUTH: THE REDSHIFT DISTRIBUTION AND EVOLUTION OF SUBMILLIMETER GALAXIES. *The Astrophysical Journal*, 788(2):125.

Slipher, V.M., 1917. Nebulae. *Proceedings of the American Philosophical Society*, 56:403. ADS Bibcode: 1917PAPhS..56..403S.

Sliwa, K., Wilson, C.D., Aalto, S., et al., 2017. Extreme CO Isotopic Abundances in the ULIRG IRAS 13120-5453: An Extremely Young Starburst or Top-heavy Initial Mass Function. *The Astrophysical Journal Letters*, 840(2):L11. Publisher: IOP Publishing.

Smail, I., Ivison, R.J., and Blain, A.W., 1997. A Deep Sub-millimeter Survey of Lensing Clusters: A New Window on Galaxy Formation and Evolution. *The Astrophysical Journal Letters*, 490:L5.

Smith, R.J., 2020. Evidence for Initial Mass Function Variation in Massive Early-Type Galaxies. *Annual Review of Astronomy and Astrophysics*, 58:577.

Smith, R.J., Lucey, J.R., and Edge, A.C., 2017. A counterimage to the gravitational arc in Abell 1201: Evidence for IMF variations, or a 1010 M black hole?†. *Monthly Notices of the Royal Astronomical Society*, 467:836.

Solomon, P. and Vanden Bout, P., 2005. Molecular Gas at High Redshift. *Annual Review of Astronomy and Astrophysics*, 43(1):677. _eprint: https://doi.org/10.1146/annurev.astro.43.051804.102221.

Solomon, P.M., Downes, D., Radford, S.J.E., et al., 1997. The Molecular Interstellar Medium in Ultraluminous Infrared Galaxies. *The Astrophysical Journal*, 478(1):144.

Spergel, D.N., Verde, L., Peiris, H.V., et al., 2003. First-Year Wilkinson Microwave Anisotropy Probe (WMAP) Observations: Determination of Cosmological Parameters. *The Astrophysical Journal Supplement Series*, 148:175. ADS Bibcode: 2003ApJS..148..175S.

Spilker, J.S., Marrone, D.P., Aguirre, J.E., et al., 2014. The Rest-frame Submillimeter Spectrum of High-redshift, Dusty, Star-forming Galaxies. *The Astrophysical Journal*, 785:149.

Spilker, J.S., Phadke, K.A., Aravena, M., et al., 2023. Spatial variations in aromatic hydrocarbon emission in a dust-rich galaxy. *Nature*, 618(7966):708. Number: 7966 Publisher: Nature Publishing Group.

Su, T., Marriage, T.A., Asboth, V., et al., 2017. On the redshift distribution and physical properties of ACT-selected DSFGs. *Monthly Notices of the Royal Astronomical Society*, 464:968.

Swinbank, A.M., Dye, S., Nightingale, J.W., et al., 2015. ALMA RESOLVES THE PROPERTIES OF STAR-FORMING REGIONS IN A DENSE GAS DISK AT z $\sim$ 3. *The Astrophysical Journal*, 806(1):L17. Publisher: IOP Publishing.

Swinbank, A.M., Lacey, C.G., Smail, I., et al., 2008. The properties of submm galaxies in hierarchical models. *Monthly Notices of the Royal Astronomical Society*, 391:420.

Swinbank, A.M., Papadopoulos, P.P., Cox, P., et al., 2011. THE INTERSTELLAR MEDIUM IN DISTANT STAR-FORMING GALAXIES: TURBULENT PRESSURE, FRAGMENTATION, AND CLOUD SCALING RELATIONS IN A DENSE GAS DISK AT z = 2.3. *The Astrophysical Journal*, 742(1):11.

Swinbank, A.M., Smail, I., Longmore, S., et al., 2010. Intense star formation within resolved compact regions in a galaxy at z = 2.3. *Nature*, 464(7289):733. Number: 7289 Publisher: Nature Publishing Group.

Tacconi, L.J., Genzel, R., Neri, R., et al., 2010. High molecular gas fractions in normal massive star-forming galaxies in the young Universe. *Nature*, 463(7282):781. Number: 7282 Publisher: Nature Publishing Group.

Tak, F.F.S.v.d., Black, J.H., Schöier, F.L., et al., 2007. A computer program for fast non-LTE analysis of interstellar line spectra - With diagnostic plots to interpret observed line intensity ratios. *Astronomy & Astrophysics*, 468(2):627. Number: 2 Publisher: EDP Sciences.

Talbot, Jr., R.J. and Arnett, W.D., 1973. The Evolution of Galaxies. III. Metal-Enhanced Star Formation. *The Astrophysical Journal*, 186:69. ADS Bibcode: 1973ApJ...186...69T.

Tayal, S.S., 2011. ELECTRON EXCITATION COLLISION STRENGTHS FOR SINGLY IONIZED NITROGEN. *The Astrophysical Journal Supplement Series*, 195(2):12.

Thomson, A.P., Ivison, R.J., Smail, I., et al., 2012. VLA imaging of 12CO J = 1-0 and free-free emission in lensed submillimetre galaxies. *Monthly Notices of the Royal Astronomical Society*, 425(3):2203.

Todini, P. and Ferrara, A., 2001. Dust formation in primordial Type II supernovae. *Monthly Notices of the Royal Astronomical Society*, 325:726. ADS Bibcode: 2001MNRAS.325..726T.

Toft, S., Smolčić, V., Magnelli, B., et al., 2014. SUBMILLIMETER GALAXIES AS PROGENITORS OF COMPACT QUIESCENT GALAXIES. *The Astrophysical Journal*, 782(2):68.

Toomre, A., 1964. On the gravitational stability of a disk of stars. *The Astrophysical Journal*, 139:1217.

Veilleux, S., Kim, D.C., and Sanders, D.B., 2002. Optical and Near-Infrared Imaging of the IRAS 1 Jy Sample of Ultraluminous Infrared Galaxies. II. The Analysis. *The Astrophysical Journal Supplement Series*, 143:315. ADS Bibcode: 2002ApJS..143..315V.

Viero, M.P., Asboth, V., Roseboom, I.G., et al., 2014. The Herschel Stripe 82 Survey (HerS): Maps and Early Catalog. *The Astrophysical Journal Supplement Series*, 210:22.

Visser, R., van Dishoeck, E.F., and Black, J.H., 2009. The photodissociation and chemistry of CO isotopologues: applications to interstellar clouds and circumstellar disks. *Astronomy and Astrophysics*, 503:323.

Walker, H.J., 2000. A brief history of infrared astronomy. *Astronomy & Geophysics*, 41(5):5.10.

Wardlow, J.L., Cooray, A., De Bernardis, F., et al., 2013. HerMES: Candidate Gravitationally Lensed Galaxies and Lensing Statistics at Submillimeter Wavelengths. *The Astrophysical Journal*, 762(1):59.

Warren, S.J. and Dye, S., 2003. Semilinear Gravitational Lens Inversion. *The Astrophysical Journal*, 590(2):673.

Watson, W.D., 1978. Gas Phase Reactions in Astrophysics. *Annual Review of Astronomy and Astrophysics*, 16(1):585. _eprint: https://doi.org/10.1146/annurev.aa.16.090178.003101.

Weisberg, J.M., Stanimirović, S., Xilouris, K., et al., 2008. Arecibo H i Absorption Measurements of Pulsars and the Electron Density at Intermediate Longitudes in the First Galactic Quadrant. *The Astrophysical Journal*, 674(1):286.

Wiklind, T., Ferguson, H.C., Guo, Y., et al., 2019. Evolution of the Gas Mass Fraction of Progenitors to Today's Massive Galaxies: ALMA Observations in the CANDELS GOODS-S Field. *The Astrophysical Journal*, 878(2):83. Publisher: American Astronomical Society.

Wright, E.L., Fazio, G.G., and Low, F.J., 1977. A high-resolution far-infrared survey of the W31 region. *The Astrophysical Journal*, 217:724. ADS Bibcode: 1977ApJ...217..724W.

Wright, E.L., Mather, J.C., Bennett, C.L., et al., 1991. Preliminary spectral observations of the Galaxy with a 7 deg beam by the Cosmic Background Explorer (COBE). *The Astrophysical Journal*, 381:200.

Yamada, R., Oyabu, S., Kaneda, H., et al., 2013. A Relation of the PAH 3.3 m Feature with Star-forming Activity for Galaxies with a Wide Range of Infrared Luminosity. *Publications of the Astronomical Society of Japan*, 65:103. ADS Bibcode: 2013PASJ...65..103Y.

Zapata, L.A., Schmid-Burgk, J., and Menten, K.M., 2011. Orion KL: the hot core that is not a "hot core". *Astronomy & Astrophysics*, 529:A24. Publisher: EDP Sciences.

Zhang, X., Lee, Y., Bolatto, A., et al., 2001. CO (J\hspace0.167em=\hspace0.167em4$\rightarrow$3) and [Ci] Observations of the Carina Molecular Cloud Complex. *The Astrophysical Journal*, 553(1):274. Publisher: IOP Publishing.

Zhang, Z.Y., Ivison, R.J., George, R.D., et al., 2018a. Far-infrared Herschel SPIRE spectroscopy of lensed starbursts reveals physical conditions of ionized gas. *Monthly Notices of the Royal Astronomical Society*, 481(1):59.

Zhang, Z.Y., Romano, D., Ivison, R.J., et al., 2018b. Stellar populations dominated by massive stars in dusty starburst galaxies across cosmic time. *Nature*, 558(7709):260.

Zhao, G., Mashonkina, L., Yan, H.L., et al., 2016a. Systematic Non-LTE Study of the -.6 [Fe/H] 0.2 F and G Dwarfs in the Solar Neighborhood. II. Abundance Patterns from Li to Eu. *The Astrophysical Journal*, 833:225. ADS Bibcode: 2016ApJ...833..225Z.

Zhao, Y., Lu, N., Xu, C.K., et al., 2016b. The [NII] 205 micron Emission in Local Luminous Infrared Galaxies. *The Astrophysical Journal*, 819(1):69. ArXiv: 1601.01404.